

-----

**ASTRONOMICAL INFRARED IMAGING**

A Thesis Presented for the Degree of  
Doctor of Philosophy.

by  
C.HOLLAND.

Department of Astronomy,  
University of Leicester.

1984

-----

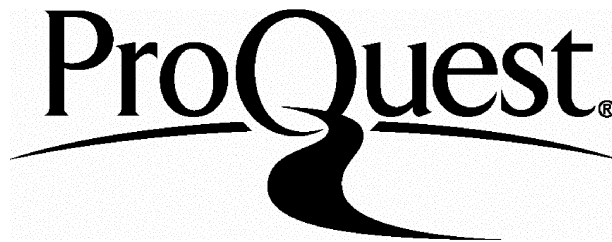
ProQuest Number: U346444

All rights reserved

INFORMATION TO ALL USERS

The quality of this reproduction is dependent upon the quality of the copy submitted.

In the unlikely event that the author did not send a complete manuscript and there are missing pages, these will be noted. Also, if material had to be removed, a note will indicate the deletion.



ProQuest U346444

Published by ProQuest LLC(2015). Copyright of the Dissertation is held by the Author.

All rights reserved.

This work is protected against unauthorized copying under Title 17, United States Code.  
Microform Edition © ProQuest LLC.

ProQuest LLC  
789 East Eisenhower Parkway  
P.O. Box 1346  
Ann Arbor, MI 48106-1346



## CONTENTS

	PAGE NUMBER
<u>INTRODUCTION</u>	I.1
<u>CHAPTER 1 : CCD/CID THEORY</u>	
1.1 INTRODUCTION	1.2
1.2 A SIMPLE THEORY OF A CCD/CID	1.2
i) THE MIS STRUCTURE	1.2
ii) ANALYSIS OF A MIS CAPACITOR	1.3
iii) THE VOLTAGE RESPONSE OF A CCD/CID	1.10
1.3 CCD/CID STRUCTURES	1.12
REFERENCES	1.20
<u>CHAPTER 2 : DESCRIPTION OF THE APPARATUS</u>	
2.1 INTRODUCTION	2.2
2.2 THE PHOTOMETER	2.3
2.3 THE CRYOSTAT AND LENS	2.9
2.4 THE MICROPROCESSOR	2.15
i) FIRST TRIP TO TENERIFE	2.17
ii) SECOND TRIP TO TENERIFE	2.20
2.5 THE DATA STORAGE MEDIA	2.22
2.6 THE RECOVERY OF THE DATA	2.23
REFERENCES	2.24
<u>CHAPTER 3 : OBSERVATIONAL RESULTS FROM THE CID</u>	
3.1 INTRODUCTION	3.2
3.2 THE FIRST TRIP TO TENERIFE	3.2
i) PATTERN NOISE	3.3

ii) CHARGE RETENTION	3.5
iii) NORMALISING THE SENSITIVITIES OF THE ELEMENTS	3.5
iv) THE OBSERVATIONS	3.7
3.3 THE SECOND TRIP TO TENERIFE	3.12
i) PATTERN NOISE AND BAD ELEMENTS	3.12
ii) CHARGE RETENTION	3.18
iii) NORMALISING THE SENSITIVITIES OF THE ELEMENTS	3.18
iv) SKY AND MIRROR DRIFTS	3.18
v) IMAGE QUALITY	3.21
vi) THE OBSERVATIONS	3.22
REFERENCES	3.26

#### CHAPTER 4 : SCANS FOR A HALO AROUND NGC 2683

4.1 INTRODUCTION	4.2
4.2 THE DATA	4.3
4.3 THE INVERSE MATRIX DECONVOLUTION METHOD	4.4
4.4 THE "BEST FIT" DECONVOLUTION	4.7
4.5 COLOUR INDICES OF NGC 2683	4.16
REFERENCES	4.25

#### CHAPTER 5 : MORPHOLOGICALLY PECULIAR GALACTIC NUCLEI

5.1 INTRODUCTION	5.2
5.2 THE OBSERVATIONS	5.4
5.3 DATA PROCESSING TECHNIQUES	5.6
i) BACKGROUND REMOVAL	5.6
ii) PICTURE CONSTRUCTION ROUTINE	5.8
iii) RADIAL POWER LAW ROUTINE	5.14
iv) COLOUR MAP CONSTRUCTION ROUTINE	5.16

5.4 ANALYSIS OF THE DATA	5.18
i) NGC 613	5.20
ii) NGC 1097	5.32
iii) NGC 1365	5.43
iv) NGC 1808	5.54
5.5 DISCUSSION AND CONCLUSIONS	5.63
REFERENCES	5.66

CONCLUDING REMARKS

APPENDIX A

CIRCUIT DIAGRAMS	A.1
------------------	-----

APPENDIX B

PASCAL PROGRAMME LISTING	B.1
--------------------------	-----

APPENDIX C

DERIVATION OF AN EXPRESSION FOR THE SEMI-MAJOR AXIS OF AN ELLIPSE IN CARTESIAN SPACE	C.1
---	-----

APPENDIX D

MAXIMUM ANGULAR TILT OF A NUCLEAR BULGE	D.1
---	-----

ACKNOWLEDGEMENTS

## ***INTRODUCTION***

## INTRODUCTION

The primary aim of this thesis, which did not quite go as initially planned, was to develop an infrared imaging system using a Charge Injection Device ( CID ). It was our intention to use this detector for building maps of the nuclear regions of galaxies. A retroreflecting focal plane scanning system, built for Dr.P.Lawson's thesis, was used for scanning images across the CID array. The electronics, controlling and reading the CID, were developed by two members of the X-Ray Astronomy group at Leicester University, namely Dr.R.S.Warwick and Dr.A.Humrich. This was commissioned by the Royal Observatory, Edinburgh, to Leicester. To handle the substantial quantities of data produced by the CID, a microprocessor was a vital component for monitoring the array and executing other jobs such as controlling the mirrors of the scanner. Consequently, a large amount of time was used writing machine code routines for the forthcoming trips and a comprehensive understanding of the hardware was a necessary preparation for possible repairs required to the microprocessor.

The first trip was to assess the characteristics of the CID and the software packages written for the

microprocessor. The scans of Saturn and Jupiter, which are discussed in chapter 3, returned some interesting results.

The lens, used for focusing the focal plane of the telescope onto the array, should have been good enough to concentrate most of the light from a point source onto a single element. However, the image was far worse than anticipated with the result that a point source, such as a star, was being smeared over several elements.

The second trip also showed a poor point source response and the culprit was thought to be the Getter releasing oil when the cryostat was baked out. This oil settled on all the cold surfaces when the cryostat was cooled.

The CID proved to have a low sensitivity and also showed an aging effect which was substantially worse on the second trip. This was probably a result of impurities becoming trapped in the surface of the array, causing a large dark current in some of the elements.

The CID's low sensitivity indicated that the goal of the thesis was not going to be reached. As a result, supplementary data were required to enhance the quality of the thesis.

Chapter 4 is devoted to the analysis of scans of NGC 2683 conducted by Dr.A.Adamson and Dr.D.J.Adams. The scans were an attempt at detecting a halo which may exist around this galaxy and some interesting results were obtained.

Chapter 5 concentrates on data, supplied by Dr.M.J.Ward, Dr.D.J.Axon and Dr.R.F.Jameson, on certain morphologically peculiar galaxies. The aim of this chapter was to discover whether these galaxies have active nuclei. It would also be interesting to see if their annular radial summation

profiles conform to those of "normal" galaxies and to ascertain the possible causes of the hot-spots seen in the optical photographs of their nuclei.

## **CHAPTER 1**

## CHAPTER 1

### 1.1 INTRODUCTION

Metal-Insulator-Semiconductor ( MIS ) technology, of which the Metal-Oxide-Semiconductor ( MOS ) transistors are a special case, is now in an advanced stage of development with MIS structures having very good interface properties.

Most of the development has been on Charge Coupled Devices ( CCDs ), which work at the visible and X-ray wavelengths. Infrared MIS detectors were not fabricated until the mid-seventies when an array of Charge Injection Devices ( CIDs ) was constructed by Kim (1975). It was made from a substrate of Indium Antimonide ( InSb ), which possesses a narrow-bandgap (  $E_g = 0.26\text{eV}$  at 77 K ), and an insulating layer of Silicon Oxynitride ( SiON ).

### 1.2 A SIMPLE THEORY OF A CCD/CID.

#### i) The MIS structure

The MIS structure, which is the basic unit from which CID and CCD arrays are constructed, consists of a gate

electrode separated from the surface of a semiconductor substrate by a thin layer of insulating material ( Figure 1.1 ). The gate electrode is made from either a metal or polysilicon<sup>1</sup>.

This structure is fundamental to all MIS devices, resulting in their behaviour being dependent on the conditions present at the insulator-semiconductor boundary.

## ii) Analysis of a MIS capacitor

On applying a voltage to the gate of a MIS device, a potential difference is established across the insulator and the semiconductor. The gate voltage is, therefore, given by :-

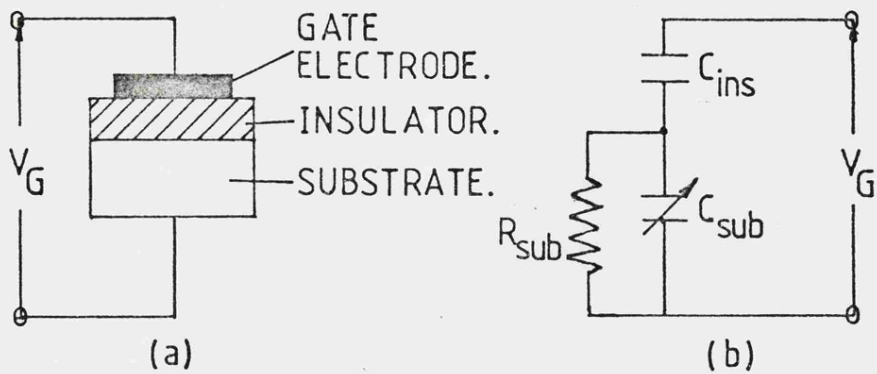
$$V_G = V_{ins} + \psi_s + V_{FB} \quad \dots [1.1]$$

where  $V_{FB}$  is the flatband voltage,  $\psi_s$  is the potential difference across the substrate and  $V_{ins}$  is the potential difference across the insulator. The bulk potential of the substrate is zero and so  $\psi_s$  is generally referred to as the SURFACE POTENTIAL.

The simple model in Figure 1.1 can be used to explain many of the characteristics of a CID ( or CCD ) ( see Grove et al (1964) ). In the following section, equations will be derived for the gate voltage and the surface potential to show how they are dependent on the time varying minority surface charge density,  $\sigma_{ins}$ , when the device is in the

---

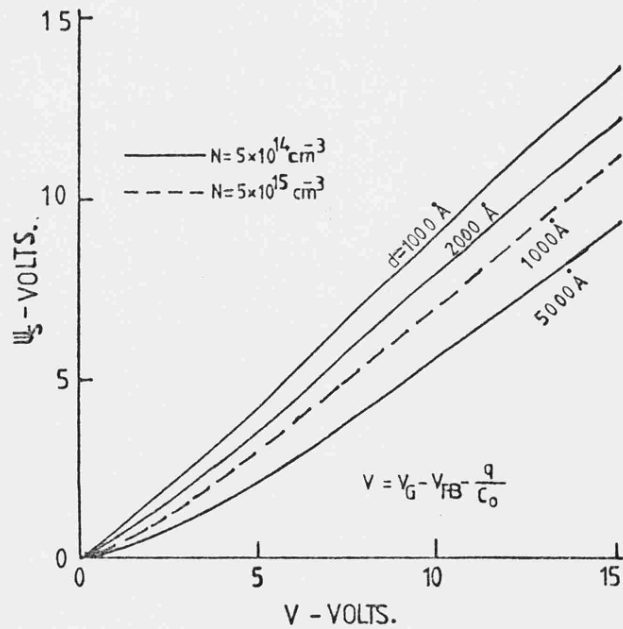
<sup>1</sup> The doping of a silicon wafer is sufficiently high that it becomes degenerate and exhibits metallic properties.



(a) SCHEMATIC DIAGRAM OF A MIS DEVICE.

(b) EQUIVALENT CIRCUIT DIAGRAM.

Figure 1.1



SURFACE POTENTIAL ( $\psi_s$ ) vs GATE VOLTAGE ( $V_G$ )  
FOR A SILICON DEVICE.

Figure 1.2

reverse biased mode.

The capacitance per unit area is defined as :-

$$C = J dt/dV \quad \dots [1.2]$$

where the current density,  $J$ , is the rate of change of the surface charge density,  $\sigma$  ( This charge density should not be confused with the charge accumulated at the insulator-substrate interface ). The current density is, therefore, given by :-

$$J = d\sigma/dt \quad \dots [1.3]$$

One must now eliminate  $J$  from equation [1.2 and [1.3 and integrate with the boundary condition  $V = 0$  at  $\sigma = 0$ . Now, using the boundary condition  $V = V_{ins}$  at  $\sigma = qN_{TOT}W$ , an expression for the insulator potential difference is obtained :-

$$V_{ins} = qN_{TOT}W/C_{ins} \quad \dots [1.4]$$

where  $q$  is the charge of the exposed impurity sites,  $N_{TOT}$  is the total exposed charge density,  $N_D - N_A + p - n$ ,  $W$  is the space charge layer width, created on applying a gate voltage, and  $C_{ins}$  is the capacitance per unit area of the insulator. However, equation [1.4 is true for the instant after a gate voltage is applied and is neglecting any minority charge build up on the insulator-substrate interface. To take this minority charge built up into account, an additional term must be added to equation [1.4

resulting in the following :-

$$V_{ins} = qN_{TOT}W/C_{ins} + \sigma_{inv}/C_{ins} \quad \dots [1.5]$$

where  $\sigma_{inv}$ , which is a function of time, is the minority surface charge density which has accumulated at the interface.

Combining the equations for the insulator voltage ( [1.5 ] ) and the gate voltage ( [1.1 ] ), one arrives at an expression for the gate voltage :-

$$V_G - V_{FB} = qN_{TOT}W/C_{ins} + \sigma_{inv}/C_{ins} + \psi_s \quad \dots [1.6]$$

where, from Gauss's law, the capacitance/unit area of a parallel plate capacitor is given by :-

$$C_{ins} = \epsilon_{ins}/x_{ins} \quad \dots [1.7]$$

where  $\epsilon_{ins}$  is the permittivity of the insulating layer and  $x_{ins}$  is its thickness.

Equation [1.6] expresses the gate voltage in terms of  $W$ ,  $\sigma_{ins}$  and  $\psi_s$ . To derive an expression for the surface potential, one must consider the instantaneous application of a gate voltage. The surface potential,  $\psi_s$ , is then obtained from Poisson's equation :-

$$d^2V/dx^2 = -\rho/\epsilon_{sub} \quad \dots [1.8]$$

where  $\epsilon_{sub}$  is the permittivity of the substrate material

and  $\rho$  is the charge density given by :-

$$\rho = qN_{TOT} \dots [1.9]$$

Integrating equation [1.8] twice, with the boundary conditions  $dV/dx = 0$  at  $x = W$  and  $V = \psi_s$  at  $x = 0$ , one obtains an expression for the voltage at any point within the substrate. The voltage profile across the depletion region, as a function of distance into the substrate, is, therefore, given by :-

$$V = qN_{TOT} (2W-x)x/2\epsilon_{sub} + \psi_s \dots [1.10]$$

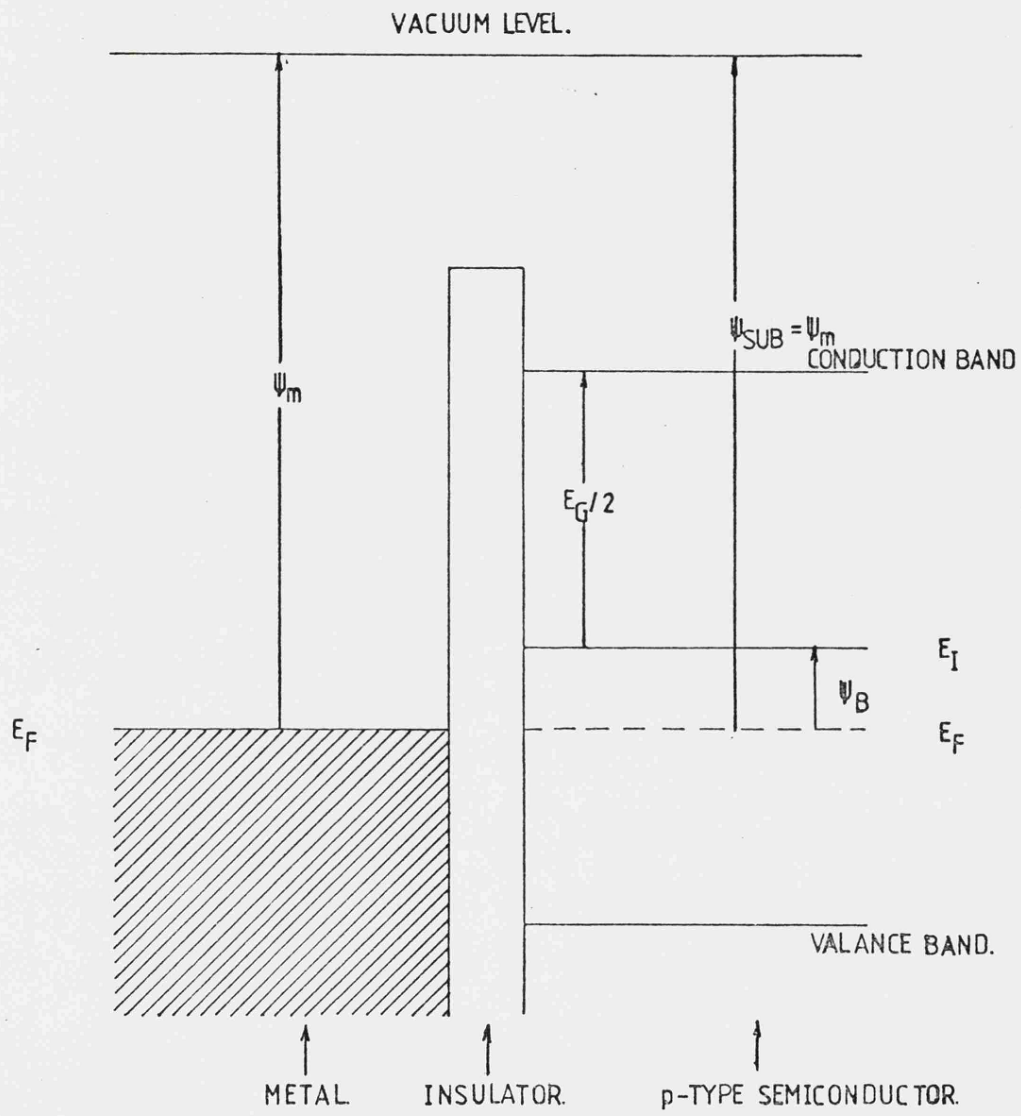
and, using the boundary condition  $V = 0$  at  $x = W$ , an expression for the surface potential is obtained :-

$$\psi_s = -qN_{TOT} W^2 / 2\epsilon_{sub} \dots [1.11]$$

This expression holds true for all values of  $t$ .

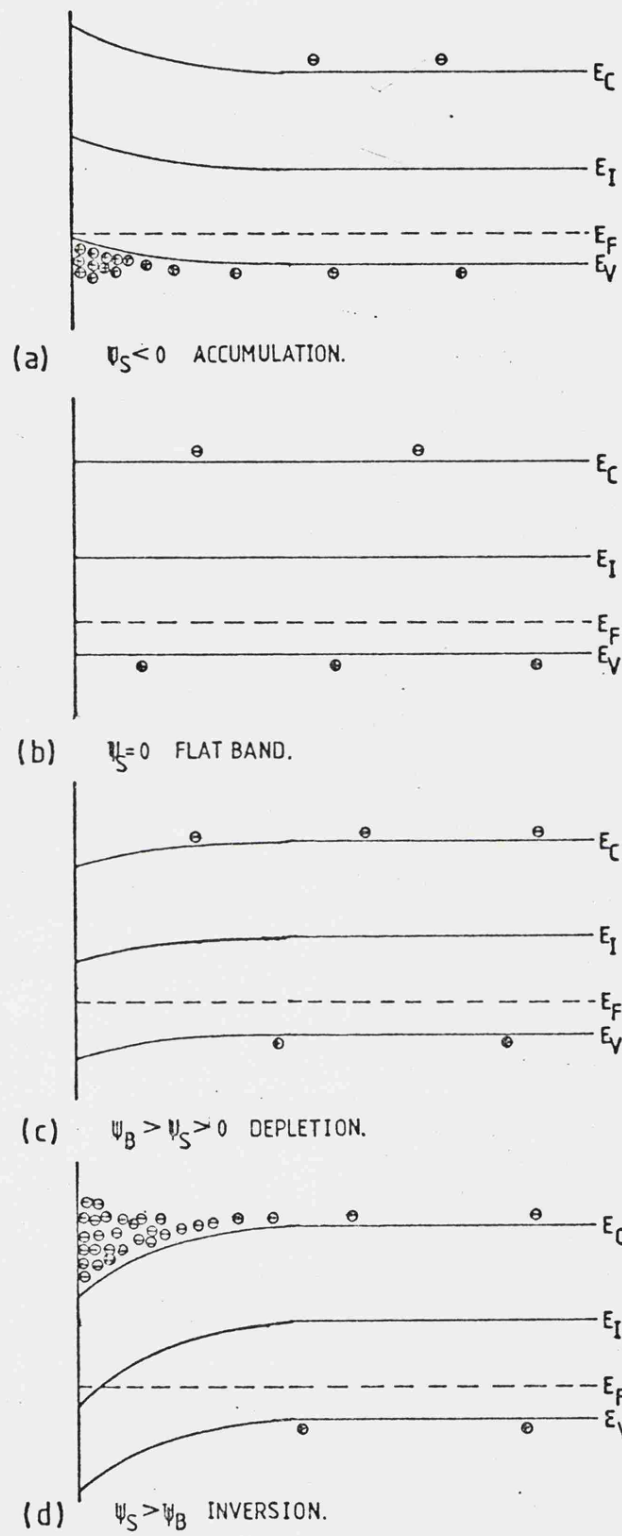
The variation of  $\psi_s$  with gate voltage for silicon ( with oxide thickness and semiconductor doping level as parameters ) is shown in Figure 1.2 ( reproduced from Amelio et al (1971) ). The effect of the surface potential on the energy bands of a p-type semiconductor, under thermodynamic equilibrium ( i.e. the Fermi level,  $E_F$ , is constant throughout the semiconductor ), is shown in Figure 1.3 and 1.4.

The relation between the space charge layer width,  $W$ , and the inversion layer surface charge density,  $\sigma_{ins}$ , is obtained by considering the total surface charge density on



FLAT BAND CONDITION IN THE IDEAL CASE (i.e.  $V_{FB} = 0$ ).

Figure 1.3



EFFECT OF AN APPLIED GATE VOLTAGE ON THE SIMPLIFIED ENERGY BANDS OF A p-TYPE SEMICONDUCTOR.

Figure 1.4

the CID ( or CCD ). This total charge must remain constant :-

$$\sigma_T = \sigma_{inv} + qN_{TOT}W = \text{constant} \quad \dots [1.12]$$

where  $\sigma_T$  is the surface charge density on the metal gate electrode. Because of the long relaxation time for the minority carriers, which is much larger than the majority carriers' relaxation time,  $\sigma_{inv}$  only increases slowly with time and as a result  $W$  must decrease. After a period of time, large in comparison to the minority relaxation time, all the gate voltage would be across the oxide layer and the space charge layer width would be zero. At this point the oxide layer is effectively sandwiched between two "metallic" field plates and the MOS device has reached saturation.

All CID and CCD devices rely on this accumulation of the minority charges in the depletion zone. These minority charges are generated mainly by photon absorption and thermal excitation, the latter of which can be suppressed by cooling the device, which results in the relaxation time of the minority charges becoming very large.

### iii) The voltage response of a CCD/CID

If one limits the following analysis to the ideal case, where the work function of the electrode material,  $\psi_m$ , and the substrate material,  $\psi_{sub}$ , are identical ( i.e.  $V_{FB} = 0$  ), then, from equation [1.6, the surface potential,  $\psi_s$ , is zero when the gate voltage,  $V_G$ , is zero. When the

surface potential is zero there is no distortion of the energy bands. This is known as the FLATBAND state ( Figure 1.4 (b) ).

If  $V_G$  becomes negative, the energy bands are bent upwards and the majority carriers are attracted to the insulator-substrate interface ( Figure 1.4 (a) ). The total capacitance of the device is then, as above, almost entirely due to the insulator being sandwiched between two "metallic" field plates.

For small positive values of  $V_G$  a depletion zone forms at the insulator-substrate interface ( Figure 1.4 (c) ). This acts as a dielectric in series with the insulator and so, from series capacitance theory, the total capacitance decreases. When  $\psi_s \approx \psi_B$  ( where  $\psi_B = E_F - E_I$ , and  $E_I$  is the intrinsic Fermi level, defined by the equation :-

$$E_I = E_V + E_G/2 \quad \dots [1.12]$$

where  $E_V$  is the valance band energy level and  $E_G$  is the valance to conduction band energy gap ) there is a population inversion ( i.e. minority carriers accumulate at the insulator-substrate interface which contribute to the substrate capacitance ) ( Figure 1.4 (d) ). This is the normal operating voltage at which all CID and CCD photon detectors are used.

At large positive values of  $V_G$  strong inversion occurs when  $\psi_s \approx 2\psi_B$  and this gate voltage is referred to as the THRESHOLD VOLTAGE,  $V_T$ , of the device. The inversion layer now dominates, unlike the p-n junction where accumulation of minority carriers cannot occur. This effectively

prevents any further penetration of the electric field into the substrate and the depletion width,  $W$ , can no longer increase because of the shielding effect of the inversion charge.

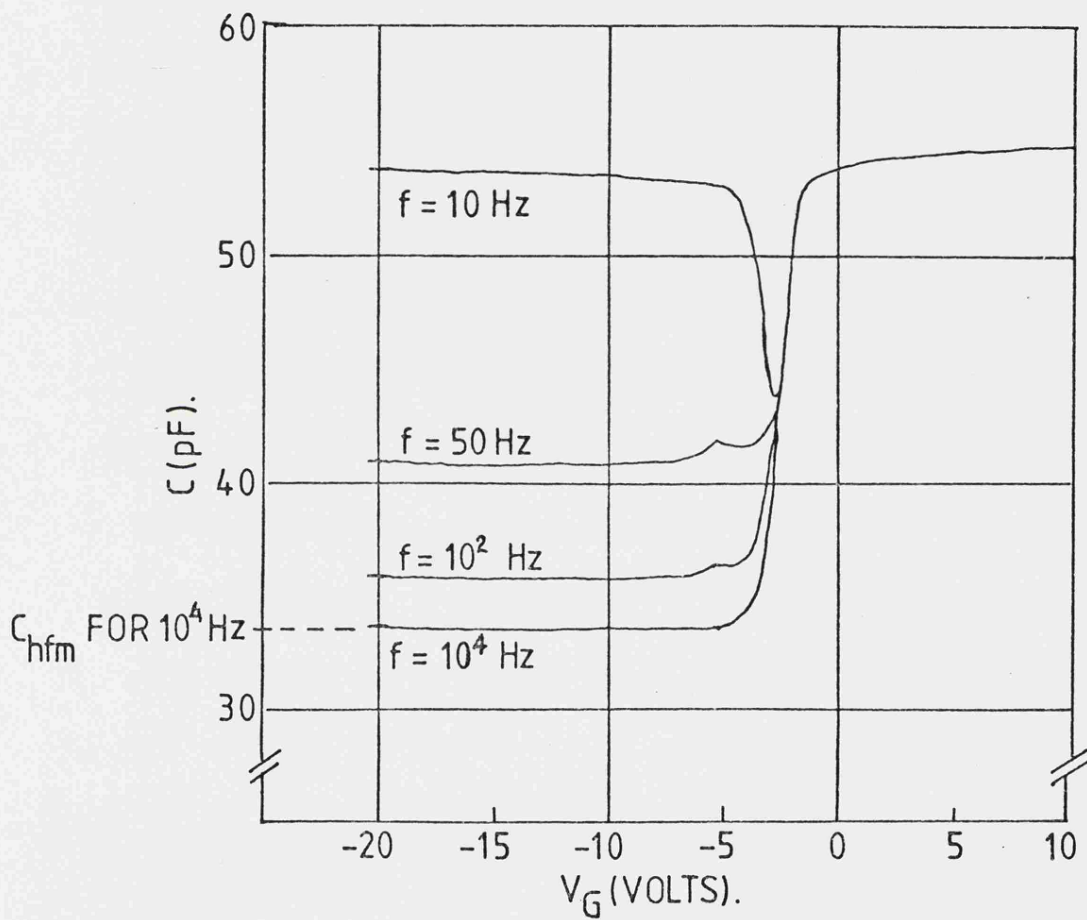
If small amplitude, high frequencies are applied to the device, the inversion capacitance remains below the low frequency capacitance because the minority carriers cannot respond to the rapid changes in the gate voltage. For these high frequencies where  $\sigma_{inv}$  is approximately zero, equation [1.4] becomes valid. In the weak inversion region the capacitance decreases with increasing gate voltage until  $\psi_s$  is approximately  $2\psi_B$ , where a minimum ( $C_{hf_m}$ ) is reached ( see Figure 1.5 ).

For the high frequency, large signal variation thermal equilibrium is not established and the inversion layer does not form. The depletion layer continues to penetrate deeper resulting in DEEP DEPLETION, and eventually  $\psi_s$  becomes large enough to cause breakdown of the semiconductor substrate.

The C-V curves for an InSb MIS device ( reproduced from Kim (1975) ) are shown in Figure 1.5. Note that the characteristics of an n-type substrate CID/CCD is the same as the p-type. However, the polarity of the gate voltage and the charges are reversed.

### 1.3 CCD/CID STRUCTURES

As the name implies, the CCD consists of an array of MIS capacitors, either one or two dimensional, arranged so that they are coupled to the adjacent capacitors. This allows



N-TYPE InSb (  $N_D \sim 3 \times 10^{15} \text{ cm}^{-3}$  ).

AREA OF DEVICE,  $A_d = 2 \times 10^{-3} \text{ cm}^2$ .

C-V CHARACTERISTICS OF AN InSb MIS STRUCTURE.

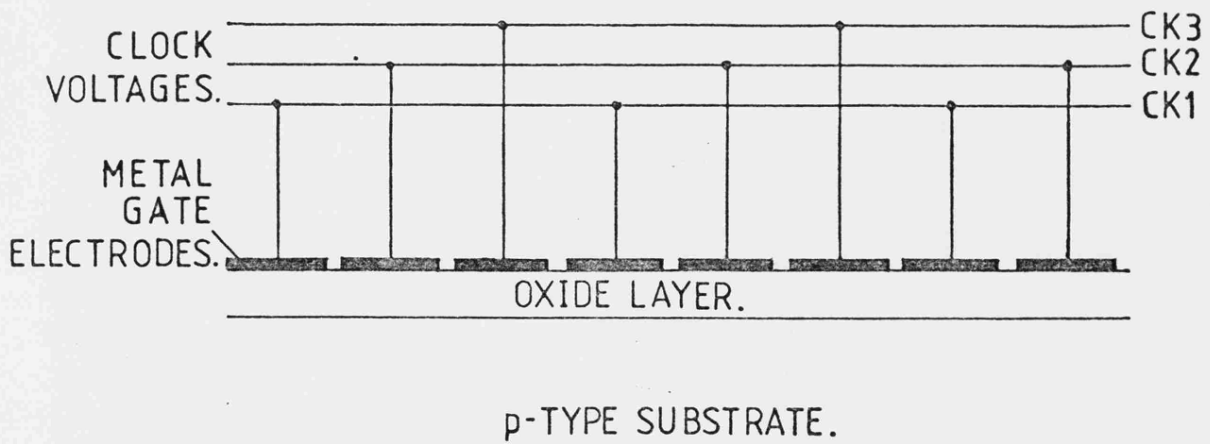
Figure 1.5

charges to be transferred between them in a controlled manner. The device is essentially an analog shift register and can be used for signal processing. Other uses are analog and digital serial memories, and optical, infrared or X-ray imaging ( eg see Steckl et al (1975) ).

In the absence of any signal charges  $\psi_s$  is a function of the applied gate voltage, the doping level in the substrate and the oxide thickness. The minority carriers from the electron-hole pairs, generated by incident photons, accumulate at the insulator-substrate interface ( region of maximum surface potential ). If two capacitors have different values of  $\psi_s$ , the charges accumulate at the maximum  $\psi_s$  provided the potential profiles overlap. Once the potential well is established, thermally generated minority carriers begin to collect in it. However, provided you cool the device and/or use a transfer rate that is very much greater than the relaxation time of the capacitor, the effect of these carriers is negligible.

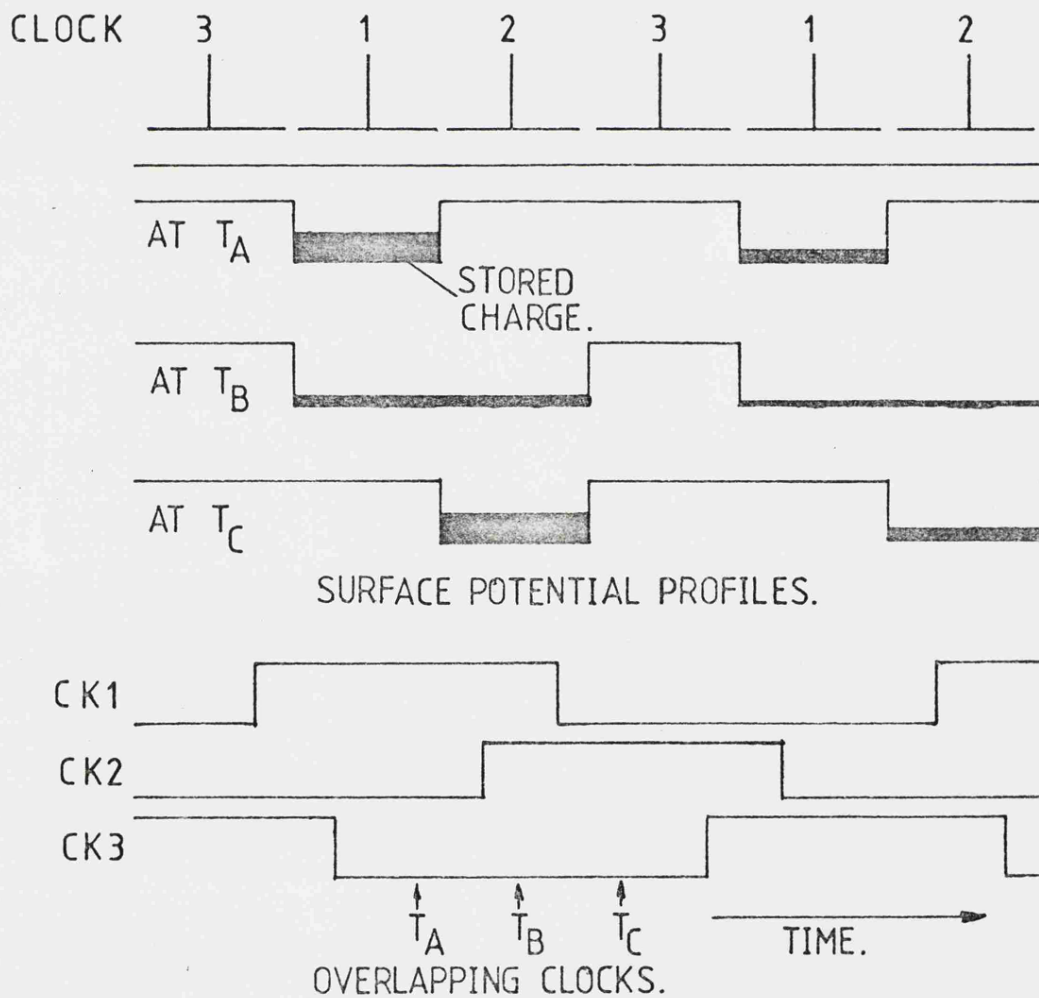
The original CCD ( Boyle and Smith (1970) ) consisted of a simple array of closely spaced metal gate electrodes ( Figure 1.6 ). Charges were transferred between electrodes by adjusting the gate voltages. Three phase clocking is required for this type of CCD and is illustrated in Figure 1.7. This simple device has the advantage of very few processing steps in its manufacture, yet the spacing of the gates must be very small, requiring extremely precise photolithography and extra circuits for the three-phase clocking.

A two phase CCD uses an asymmetric potential profile under the electrodes, which ensures that the transfer of



SCHEMATIC CROSS SECTION OF A SIMPLE n-CHANNEL CCD.

Figure 1.6



3-PHASE CHARGE TRANSFER CLOCKING FOR A CCD.

Figure 1.7

charge only occurs in one particular direction. This is accomplished by either varying the oxide thickness under the electrodes, or by varying the doping level at the substrate surface by "ion implantation"<sup>2</sup> of impurities ( Figure 1.8 ).

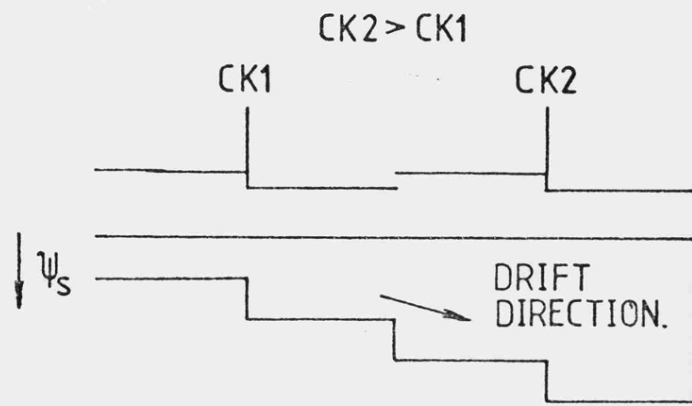
Transfer losses between storage regions in CCD's are caused by diffusion due to mutual repulsion between charge carriers and the existence of surface trapping states. The effect of diffusion diminishes relatively quickly as the amount of signal charge is decreased. The effect of surface trapping states can be reduced by growing ( or ion implanting ) a layer with an opposite dopant type onto the substrate. The effect of this is to shift the position of the maximum surface potential into the bulk material. Trapping states in the bulk material can also cause loss of charge, yet this effect is less than that due to the surface states. Thus, this type of CCD is known as a BULK-CHANNEL CCD ( BCCD ).

The output signal of a CCD is obtained either by current or voltage sensing. Current sensing of the output employs a drain diffusion that is held at a steady potential ( Figure 1.9 ). The CCD array acts effectively as a multiple gate MIS transistor in which the drain current is proportional to the charges transferred to the final gate electrode.

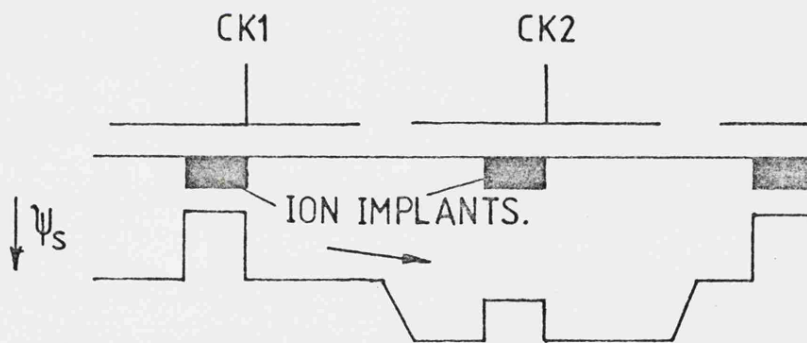
Voltage sensing is achieved by using a floating-diffusion amplifier ( Figure 1.10 ). The floating diffusion is connected to the gate of a MOS transistor and the potential

---

<sup>2</sup> This is a technique for introducing a precise level of dopant into the lattice of a semiconductor crystal by bombarding the surface with ions of that dopant.



VARYING OXIDE THICKNESS.



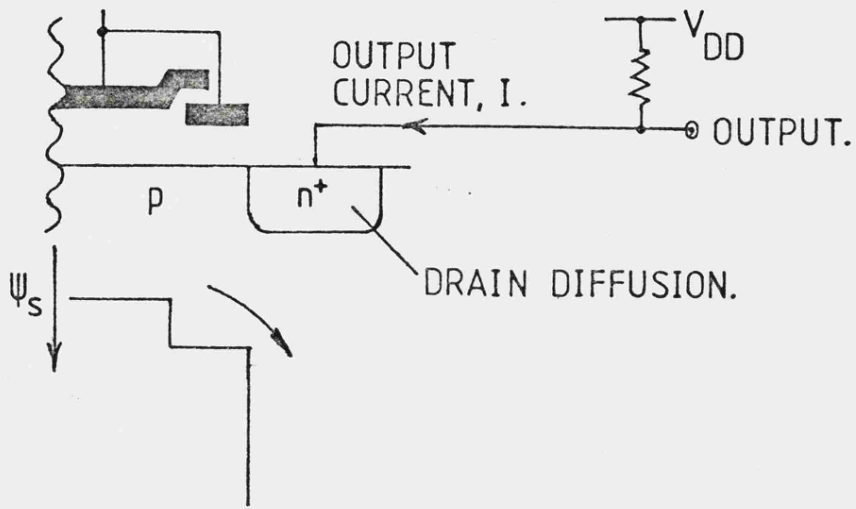
ION IMPLANTATION.

2-PHASE ASYMMETRIC POTENTIAL WELLS FOR A CCD.

Figure 1.8

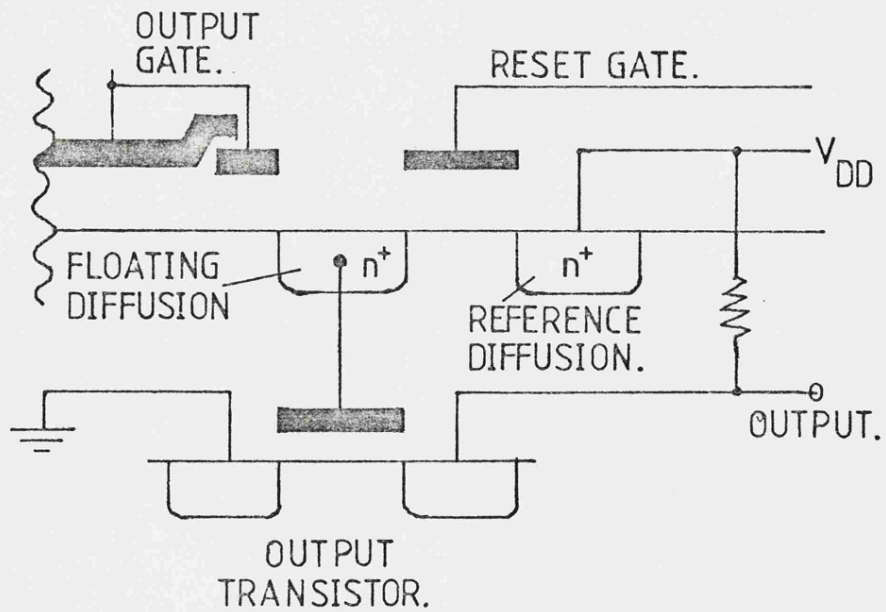
variations produce an output signal proportional to the reference signal variations. The floating diffusion is reset to the reference level using a reset gate between each signal pulse.

The CID array used for this thesis consists of 33 detectors ( 0.1 mm x 0.1 mm square ), having a separation of 0.03 m.m. between elements. To use the CID as a photon detector a bias voltage was initially applied to all of the elements in the CID. In this state the minority charges generated by incident photons are attracted to the insulator-substrate interface and the majority charges drift into the bulk substrate. To read the elements, the bias voltage was removed and a positive going injection voltage was applied. This drives the minority charges out into the substrate where they recombine with the majority charges. Sampling of the voltage on the output electrodes of the elements before and after injection gives a measure of the accumulated charge which is a function of the incident photon flux. The circuit diagrams of the electronics developed for reading the CID, are shown in APPENDIX A.



CURRENT-SENSING CCD OUTPUT.

Figure 1.9



VOLTAGE-SENSING CCD OUTPUT.

Figure 1.10

## REFERENCES

AMELIO, G.F., BERTRAM, W.J., and TOMSETT, M.F., IEEE Transactions on Electron Devices, Vol. ED-18, pp 986-992, Nov. 1971.

BOYLE, W.S., and SMITH, G.E., Bell Syst. Tech. J., Vol. 49, pp 587-593, Apr. 1970.

GOETZBERGER, A., and NICOLLIAN, E.H., Appl. Phys. Letters, Vol. 9, pp 444-446, Dec. 1966.

GROVE, A.S., SNOW, E.H., DEAL, B.E., and SAH, C.T., J. Appl. Phys., Vol. 35, pp 2458-2460, Aug. 1964.

KIM, J.C., Proceedings of the 1975 International Conference on the Application of Charge Coupled Devices, Sep. 1975.

STECKL, A.J., NELSON, R.D., FRENCH, B.T., GUDMUNDSEN, R.A., and SCHENCHTER, D., Proceedings of The IEEE, Vol. 63, pp 67-74, Jan. 1975.

## **CHAPTER 2**

## CHAPTER 2

### 2.1 INTRODUCTION

This chapter will discuss the apparatus used in detail. Most of the photometer had already been constructed for Dr.P.Lawson towards his thesis on 10 $\mu$ m imaging ( Lawson (1980) ), so very little work was required on the photometer initially. However, later discoveries about the system necessitated amendments to it.

A new cryostat was bought for the CID, and the changes required in the interior were carried out by Mr.V.Brooksbank<sup>1</sup>.

While this was in progress, flexible software programmes for the microprocessor system were being developed. The control of the mirrors, reading the data stream from the CID, as well as processing and storing the data had to be accomplished.

The subjects discussed in this chapter are shown below:-

2.1] INTRODUCTION

2.2] THE PHOTOMETER

---

<sup>1</sup> Technician at Leicester University.

- 2.3] THE CRYOSTAT AND LENS
- 2.4] THE MICROPROCESSOR
- 2.5] THE DATA STORAGE MEDIA
- 2.6] THE RECOVERY OF THE DATA

## 2.2 THE PHOTOMETER

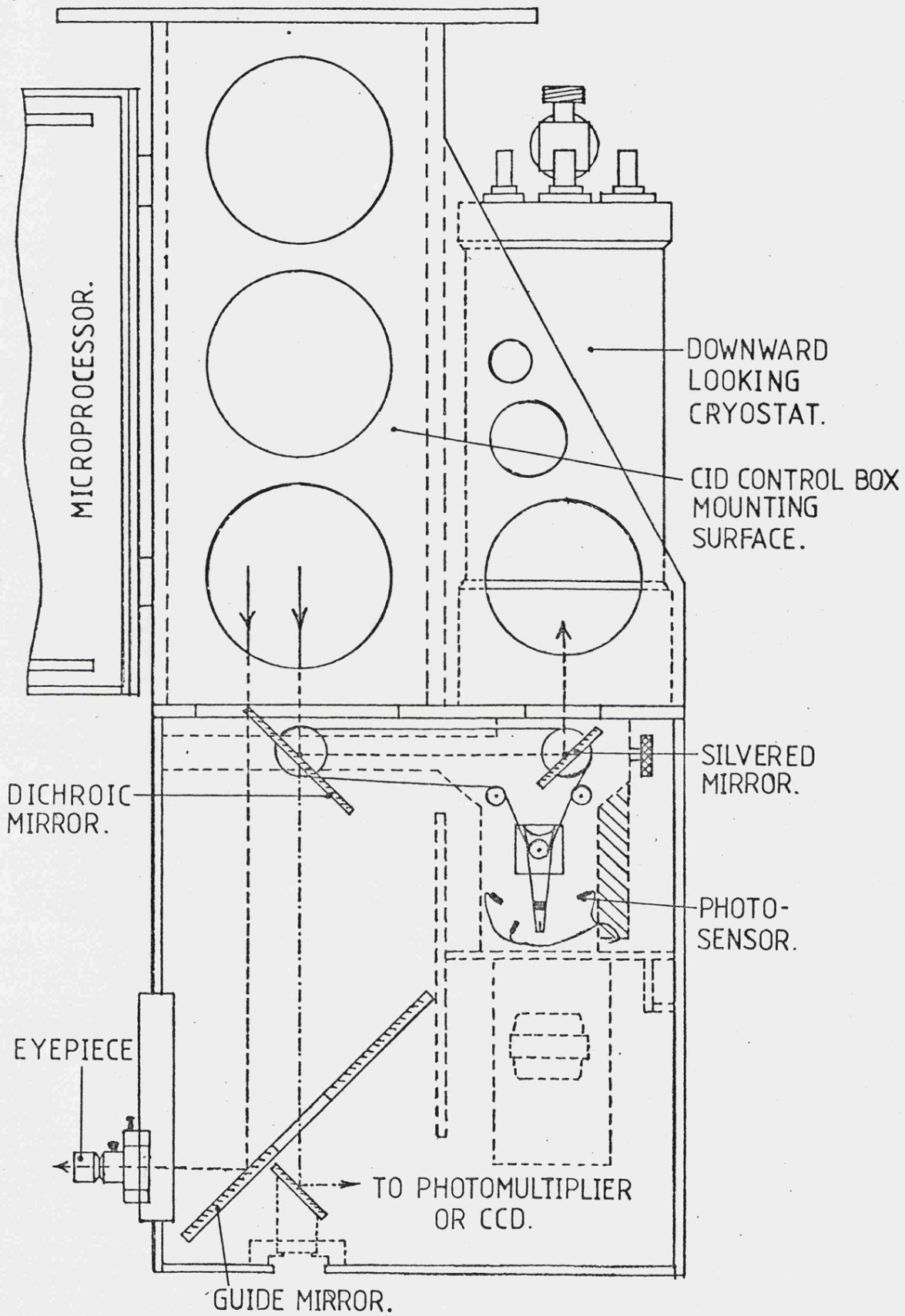
The photometer was designed and built by Mr.C.D.Maddock<sup>2</sup>, for Dr.P.Lawson's work towards his thesis. The two main problems foreseen were the coupling of the two mirrors, and their backlash. The coupling was accomplished by using pre-stretched steel wire, wrapped around the drive wheels twice to stop any slippage. The backlash was almost entirely eliminated by reducing the weight of the mirror cradles, the mirrors, the axles, and the drive wheels to a minimum. Moreover the air moved by the mirrors when advanced, added to the dampening of any oscillations in the system ( Lawson (1981) ).

The reason for keeping the two mirrors perpendicular ( Lawson (1981) and Baddiley (1977) ), enabled a section of sky to be scanned at right angles to the array axis, while the image of the sky remained in focus on the detector. Figure 2.1 is a cross-sectional drawing of the photometer before any changes were administered, and Figure 2.2 is the focal plane scanning system removed from the photometer box.

The first mirror, which the converging beam from the

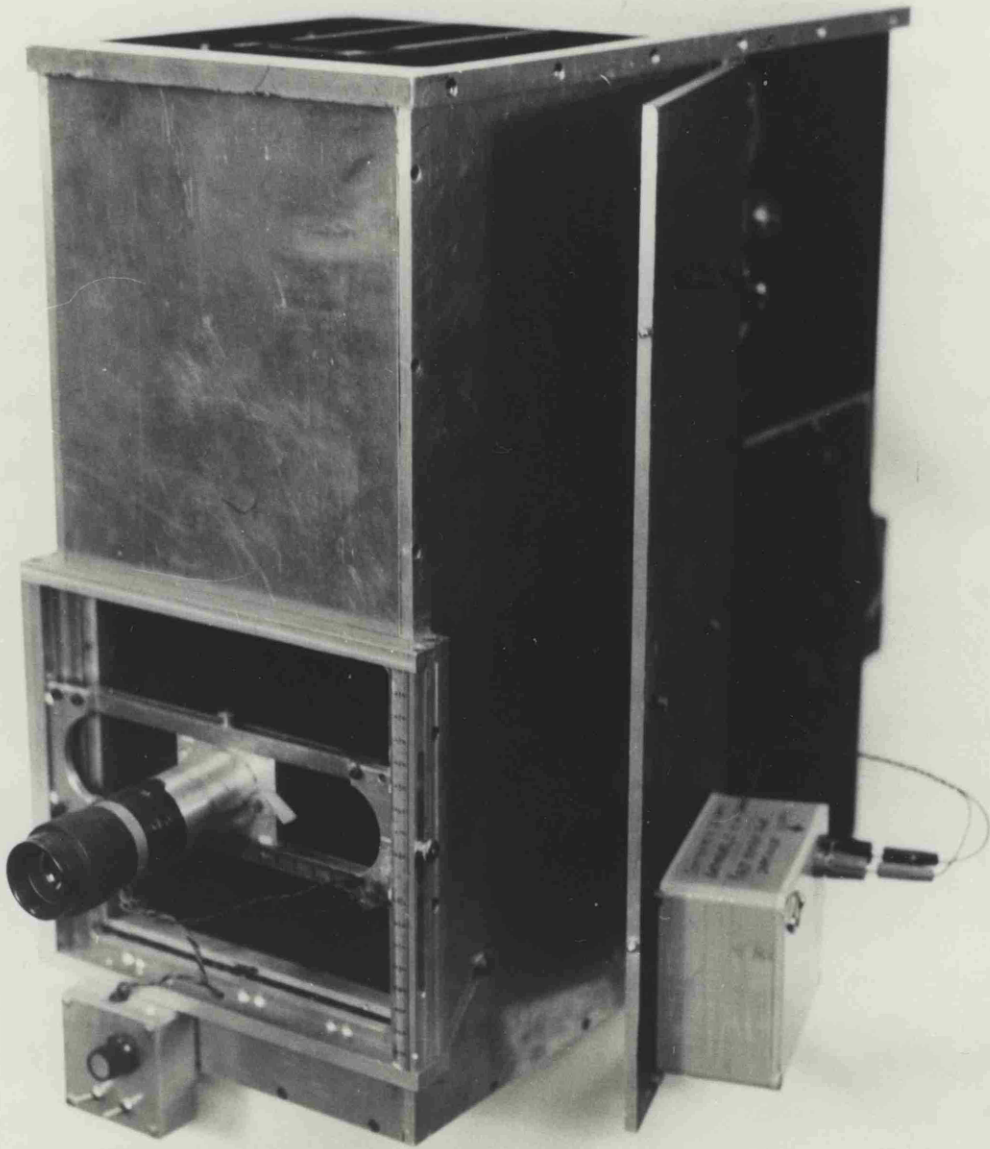
---

<sup>2</sup> Formerly a Technician at Leicester university, now retired.



THE PHOTOMETER.

Figure 2.1



A PHOTOGRAPH OF THE FOCAL PLANE SCANNER.

Figure 2.2

telescope encounters, is a thin dichroic, with a large cross-sectional area. Dichroic mirrors possess the property of reflecting 98%<sup>3</sup> of the radiation with wavelengths longer than 1.5 $\mu$ m, yet achieve 50% transmission at 0.5 $\mu$ m. The transmission of the optical light permits the observer to view the object while, at the same time, the retro-reflecting mirror pair scan the infrared radiation from the object across the CID array. If required, the optical light from the object, instead of being directed into the observer's eye, could be focused onto a photomultiplier, or possibly an optical CCD.

On reflection from the dichroic mirror, the infrared beam is directed towards the second of the retroreflecting mirror pair. This diverts the beam upwards into the base of a downward looking cryostat, and is focused onto the detectors.

The retroreflecting mirrors are controlled by a single stepper motor, mounted directly below the second mirror. The stepper motor, which can accomplish 800 steps per revolution, is activated only by the microprocessor. The angular step size of the motor had to be reduced from 0.45° to 0.09° ( see equation [2.2] ). This meant that the circumference of the mirror drive wheel to the circumference of the motor drive wheel had to be in a ratio of 5:1 respectively.

For positional information on the mirrors, an arm attached to the shaft of the motor can break photosensors, which are positioned at the two extreme ranges of the arm's

---

<sup>3</sup> These percentage values are dependent on the deposition thickness.

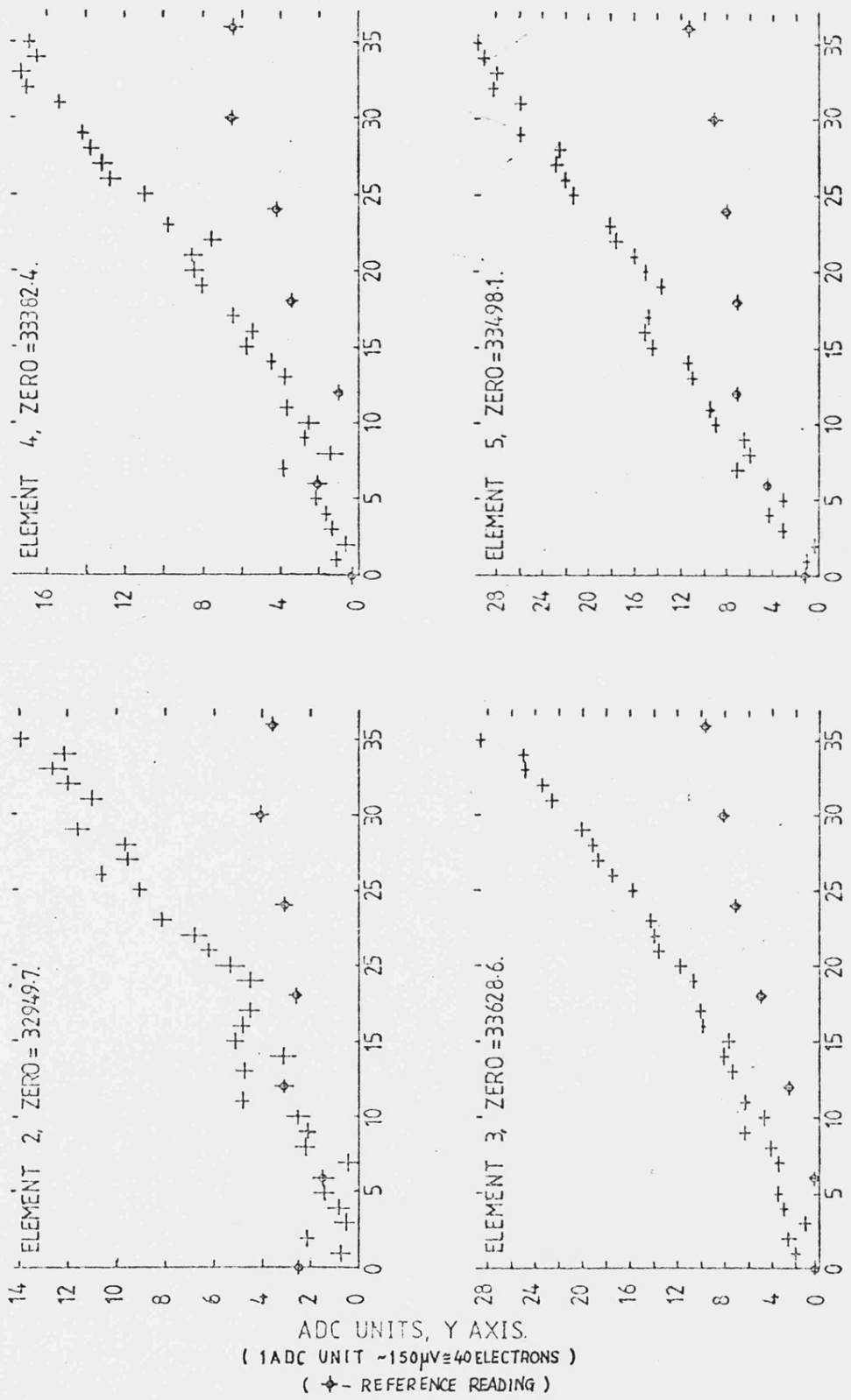
swing. There is also a photosensor at the zero point, which, when the two mirrors are at  $45^\circ$  to the horizontal, is activated. This position was always used as the start of the scans.

The Tenerife 60" telescope, used for all our observations, is not renowned for its tracking capability, so a guide mirror was mounted in the photometer and an eyepiece was positioned on an X-Y guide frame ( see Figure 2.1 ). The image of an object was focused on illuminated cross-hairs in the eyepiece. This eliminated any parallax between the two. The observer could then position the cross-hairs on a guide star at the beginning of a scan, and then supervise and correct, if needed, the tracking of the telescope.

If the optical channel was not in use, the hole in the guide mirror could be moved so that the light would be redirected to the eyepiece, allowing the observer to guide on the object under scrutiny.

On the first trip, the mirror step size was discovered to be twice the detector width, which could not be corrected until the photometer was returned to Leicester. Moreover, because our observations were confined to bright sources, an effect was overlooked which increases as a function of time from when the apparatus was turned on. This effect also superimposed the data points on a general upward drift beginning at the start of the scan and became worse along the scan direction ( see Figure 2.3 ). A probable cause was the large amounts of heat generated by the electronics, the transformer, and the stepper motor.

To overcome this, the electronics and the transformer



NUMBER OF MIRROR MOVEMENTS, X AXIS.

THE DRIFTS AS A FUNCTION OF MIRROR POSITION.

Figure 2.3

were mounted outside the photometer box on insulating legs to reduce the heat generated within it. However, the repositioning of the stepper motor was considered by Mr.C.D.Maddock to be impractical.

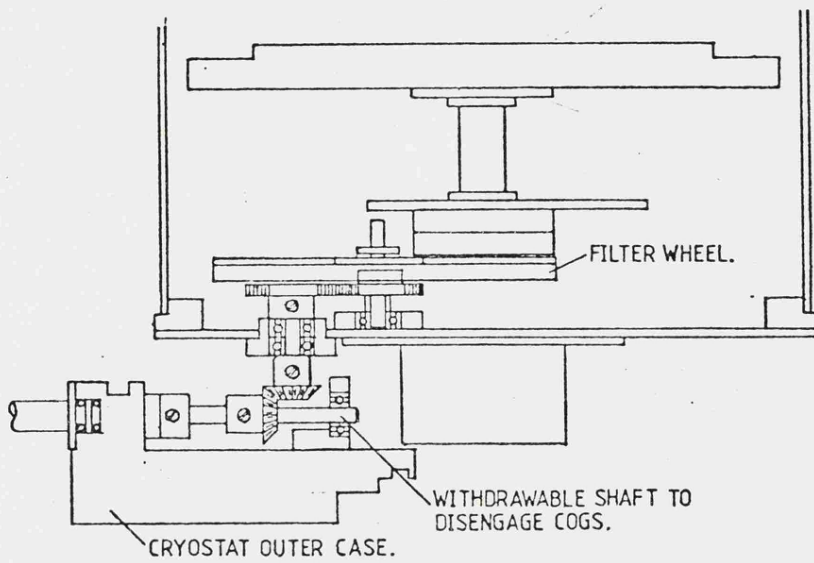
An opportunity to test the revised photometer was not forthcoming because an application for time on the South African 40" telescope was refused.

### 2.3 THE CRYOSTAT AND LENS

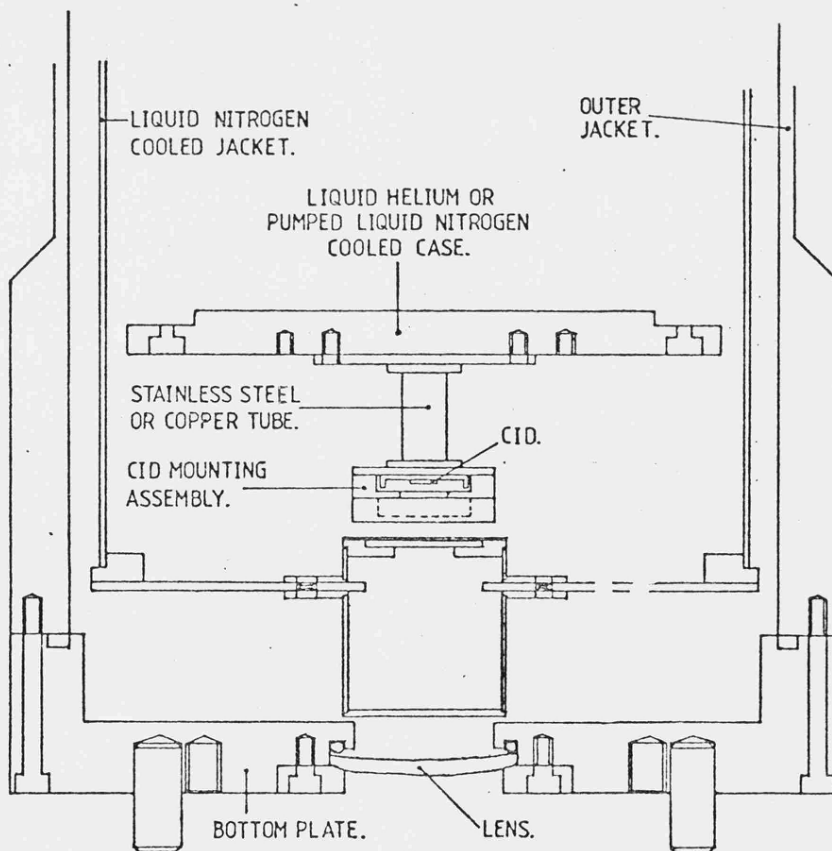
The cryostat, which was an Oxford Instruments modified MD800 liquid helium cryostat, was purchased specifically for the array. The CID mounting assembly was connected to the base of the liquid helium dewar ( 4K ) via a stainless steel tube ( see Figure 2.4 (a) and (b) ). The tube's thermal resistance along with the heat input through the connecting leads from the nitrogen dewar, and the preamplifier, maintained the CID at a working temperature of approximately 30K, which maximised its efficiency.

On observing trips, liquid helium was not employed as a coolant, and the stainless steel tube was replaced with a copper tube, which has a low thermal resistance. However, the liquid helium was substituted with pumped liquid nitrogen ( ~50K ), and the outer dewar was filled with liquid nitrogen.

Figure 2.4 (a) shows the internal arrangement of the cryostat on the first trip. The converging F13 beam entered the bottom of the cryostat through a Zinc Selenide ( ZnSe ) lens, which focused the image onto the array. After the beam had passed through the lens into the outer vacuum



(a) INITIAL CONFIGURATION OF CRYOSTAT.



(b) CONFIGURATION ON SECOND TRIP.

Figure 2.4

chamber, it then entered the inner vacuum chamber by passing through two K filters. Because the first K filter was taking the brunt of the radiation from and through the entrance lens, the second filter, mounted just above the array, was required to filter out any superfluous radiation which may be emitted from the "hot" inner surface of the first filter. The second filter also helped in reducing any stray radiation that may have been creeping into the inner volume in which the detector was mounted.

A top hat arrangement was mounted on the outer face of the base plate of the liquid nitrogen tank to define the beam as well as possible and also reduce any stray light from entering the system.

Because of these two filters, it was only possible to conduct our observations at the Johnson K band for the first trip.

For the second trip, a filter wheel arrangement was built into the cryostat, as shown in Figure 2.4 (b). However, the construction of this was not completed before the second trip, and consequently the observations on this trip were also restricted to the Johnson K.

With the system unaltered, the plate scale would be 9.59 arcseconds / mm. Therefore, each detector would have seen  $9.59 / \text{mm} \times 0.13\text{mm} \approx 1.25$  arcseconds. However, because of the expected seeing conditions a detector size of 3.7 arcseconds / element was more realistic. A condensing lens was therefore required with a magnification of :-

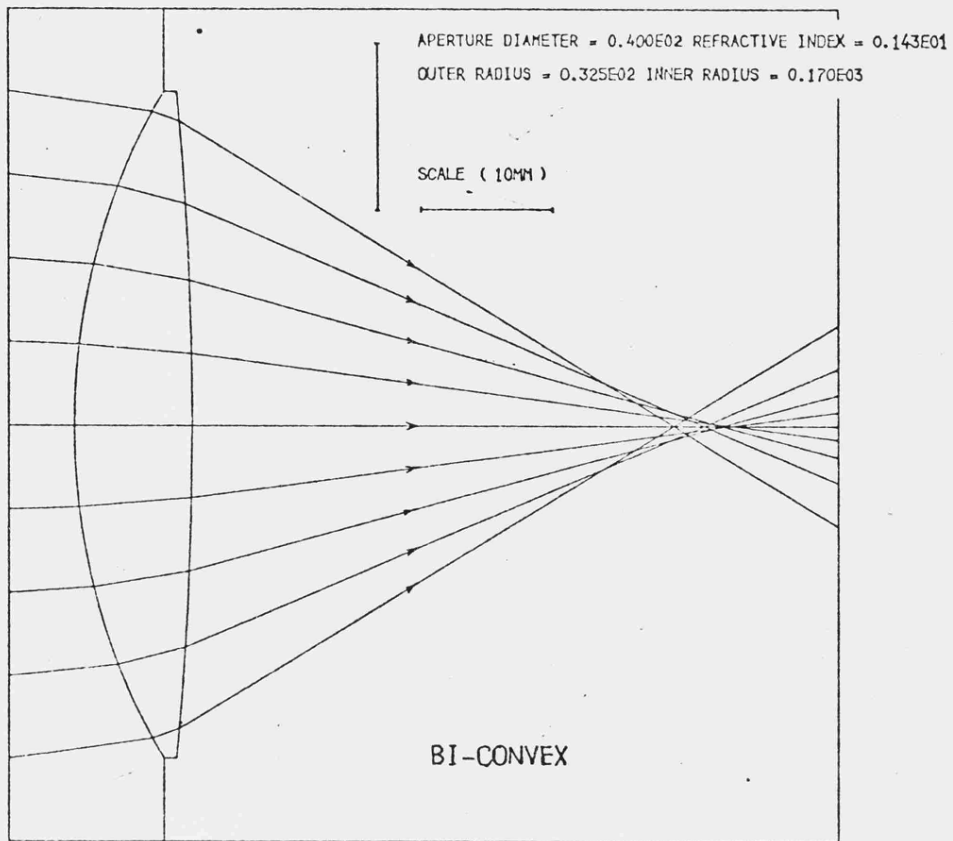
$$\frac{\text{HEIGHT OF IMAGE}}{\text{HEIGHT OF OBJECT}} = \frac{3.70}{1.25} \approx 3 \quad \dots [2.1$$

With the lens mounted in the cryostat, the new detector distance would be  $175\text{mm} \times 1/3 = 58.33\text{mm}$  above the base plate. Moreover, the array would have an apparent size of  $3 \times 4.26\text{mm} = 12.8\text{mm}$  and with our plate scale of  $9.59$  arc-seconds / mm, this is equivalent to 2 arcminutes on the sky.

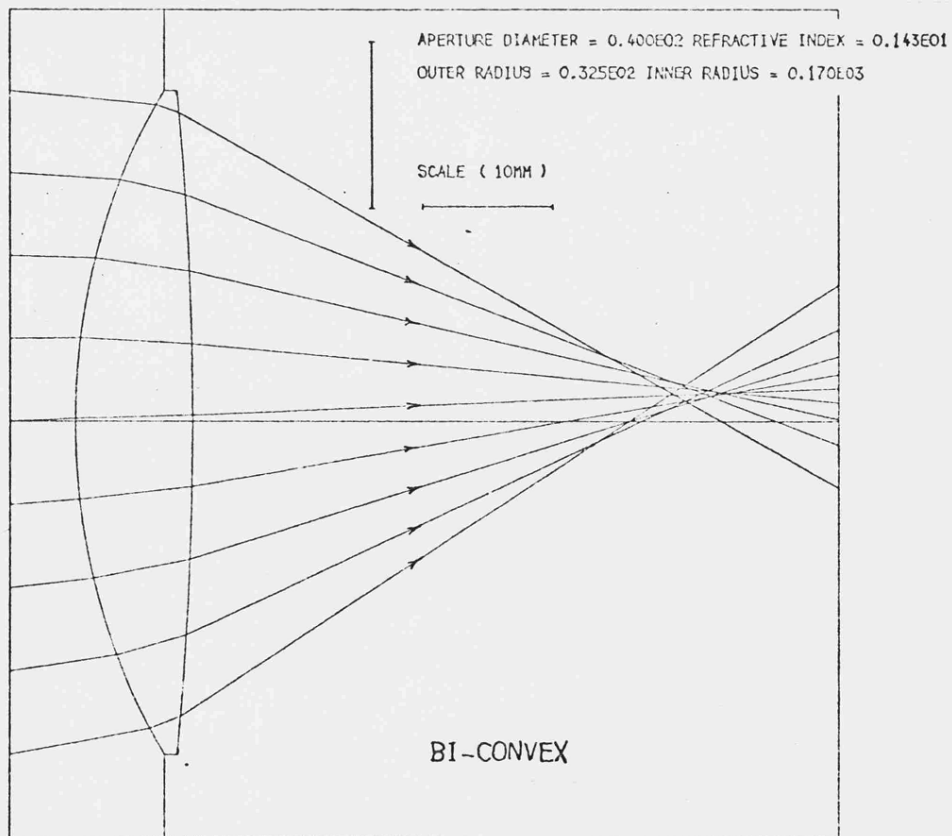
This lens was ordered from Spectroscopic Accessories, who proposed that the most suitable material to make the lens from was Calcium Fluoride ( $\text{CaF}_2$ ), with the inner and outer face having radii of curvature of 170 and 32.5mm respectively (ie a convex lens).

To check this, a programme was written on the CYBER to trace the rays through the lens in question, and give an idea of the spherical and comatic aberrations. The rays traced through this lens indicated that it was not suitable and on contacting Spec. Acc., they confirmed that they had made an error. The second lens, with inner and outer faces having radii of curvature of 80 and -212mm respectively (ie a convex-meniscus), was constructed from ZnSe which is a stable and non-hygroscopic material. This was much improved over the initially proposed lens.

Figure 2.5 and 2.6 show the plots produced by the ray tracing routine for both lenses. The  $\text{CaF}_2$  lens focused the F13 beam approximately 50mm behind the front face, and also exhibited strong spherical and comatic aberrations. If the outer two rays are ignored, the ZnSe lens has a sharp focus and its focal point is 58.7mm behind the front face. This compares favourably with the detector distance from the bottom of the base plate. Moreover, if the CID was centred on the optical axis of the lens, the off axis plot shows

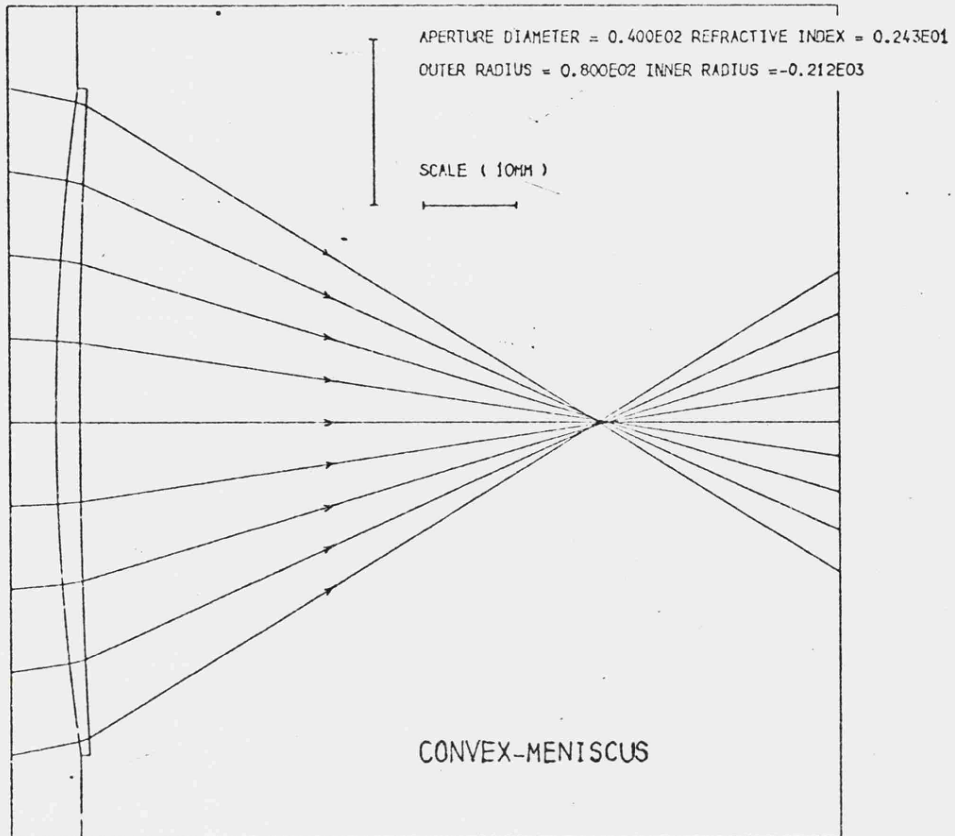


(a) ON AXIS PLOT FOR  $\text{CaF}_2$  LENS.

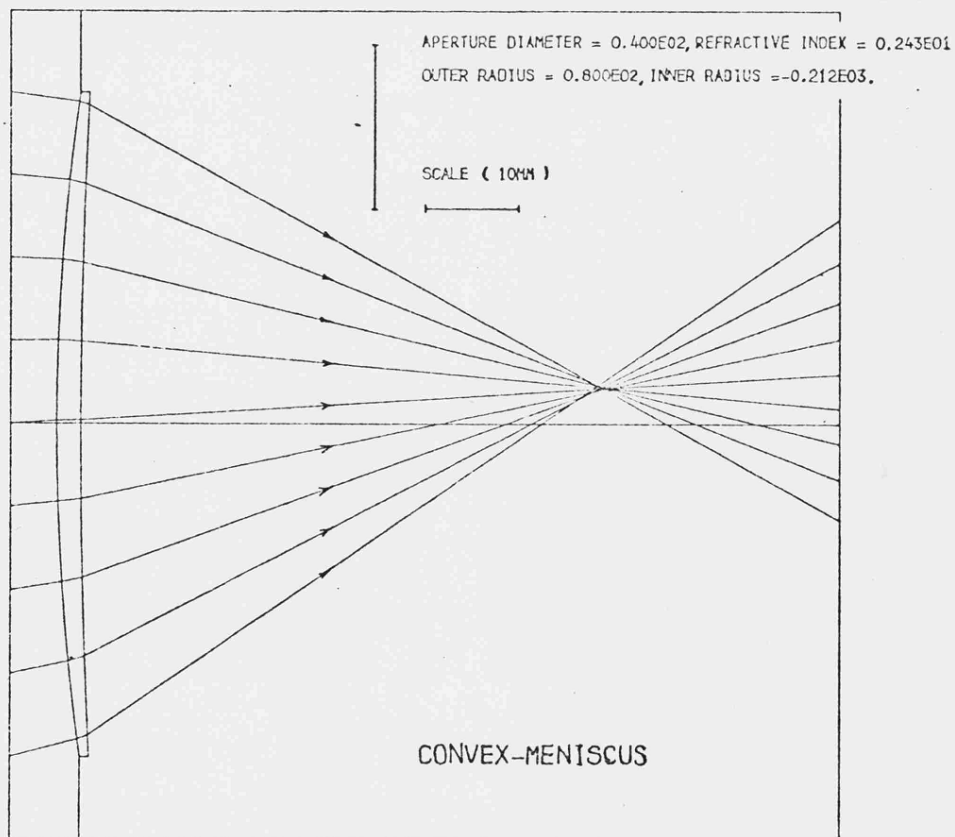


(b) OFF AXIS PLOT FOR  $\text{CaF}_2$  LENS.

Figure 2.5



(a) ON AXIS PLOT FOR ZnSe LENS.



(b) OFF AXIS PLOT FOR ZnSe LENS.

Figure 2.6

the effect of the aberrations on the detectors at its extreme edge. This plot indicates that nearly all the light would fall in a circle of diameter 0.05mm, which is half the diameter of each detector. So, any smearing of the image must be influenced primarily by the seeing conditions and the image quality of the telescope.

This lens accounts for the step size error discussed in the earlier section. The equation for the horizontal displacement of an image is given by :-

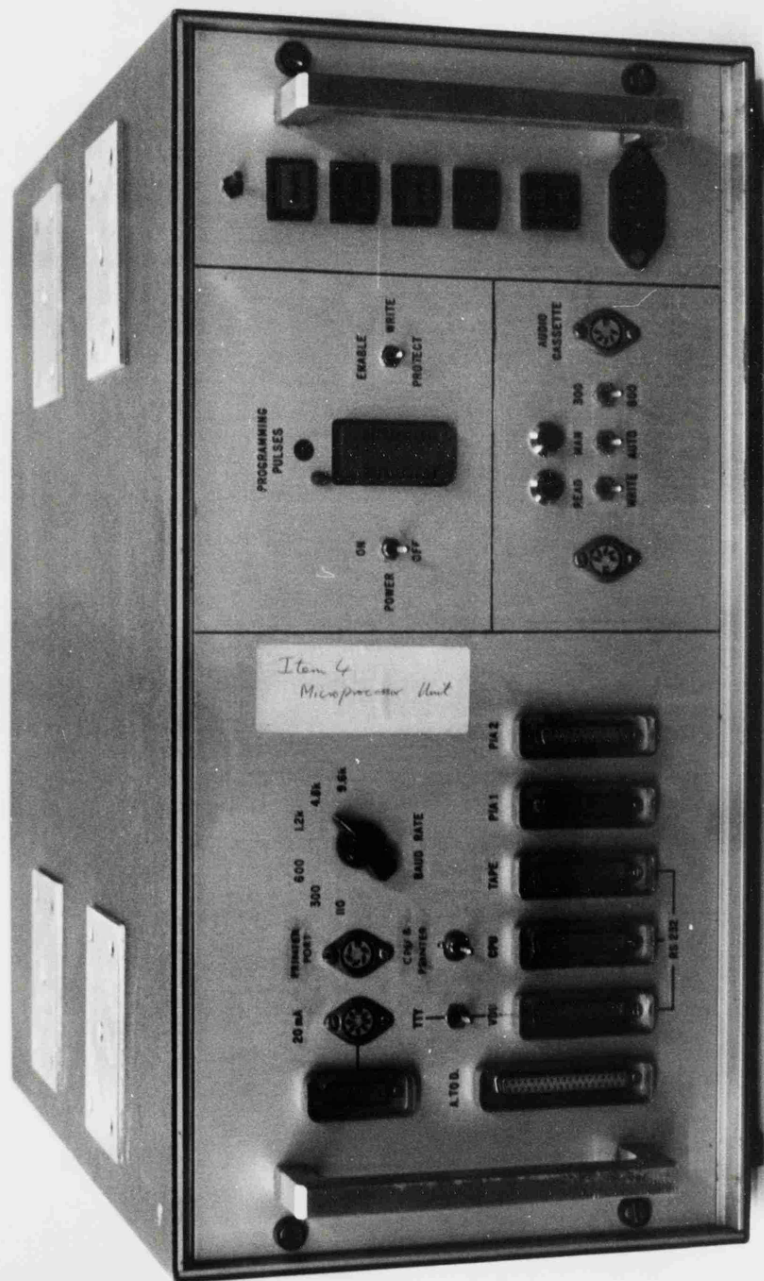
$$x = d \sin ( 2t ) \quad \dots[2.2]$$

where  $d$  = the mirror pivot separation ( 215mm ), and  $t$  = the angle of rotation of the mirrors (  $0.09^\circ$  ).

This yields a displacement of 0.67mm / step. However, each element has the apparent width of  $3 \times 0.1\text{mm} = 0.3\text{mm}$ . Therefore, the step angle of the mirrors had to be halved to accommodate for the reduction in the detector size.

#### 2.4 THE MICROPROCESSOR

The controlling microprocessor employed in both trips, Figure 2.7, was an M6800 microprocessor system, produced by Motorola. This was based upon the easily understood 6800 microprocessor chip. However, it was operated at machine code level, and had no high level languages available such as BASIC. The advantage of machine code is its speed. However, the disadvantages are the difficulty of reading the highly complex programmes, and debugging them.



PHOTOGRAPH OF MICROPROCESSOR.

Figure 2.7

i) First trip to Tenerife

It was decided that the microprocessor would start the integration of the CID by sending a pulse via a Peripheral Interface Adapter (PIA), while the rest of the time, the CID would continue integrating.

The microprocessor then executed the following for one complete scan :-

1] Asked the user for the number of positive and negative scan positions.

2] Moved the mirrors into the zero position, and a pre-reading of the CID was performed to flush out any accumulated charge.

3] The data were read from the CID through the PIA, and transferred into the picture storage area. The mirror position was checked to ascertain if the end of the scan<sup>4</sup> had been reached. If true, the routine would terminate ready for the user to display, store, or discard the generated picture. Providing the above was false, the microprocessor would check that the limits of the mirror movement, set by the user, had not been encountered, if not, the mirrors were advanced a step and routine 3] was executed again.

---

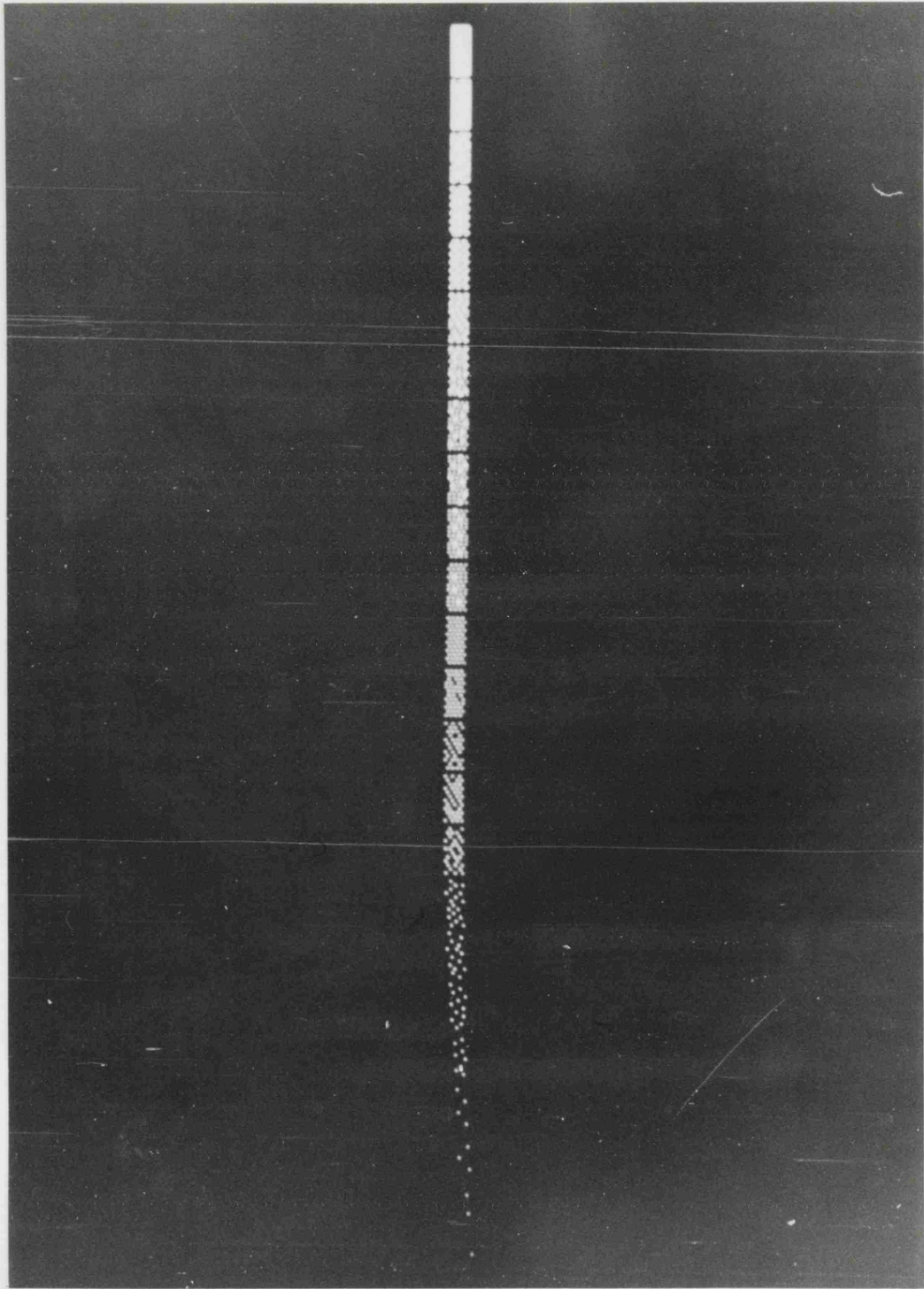
<sup>4</sup> A scan ends when the mirror has stepped from the zero position, to the positive step limit, back to the negative step limit and finally encounters the zero position again.

4] The direction of the mirror movement was reversed, and the microprocessor returned to routine 3].

On completion of the scanning routine, the next step was generally to display the data on a DACOL Visual Display Unit (VDU). To display the data as a grey scale picture, the character generator chip in the VDU was replaced with a 2716 Electrically Programmable Read Only Memory (EPROM) chip mounted on a pin conversion plug, since the two chips were not directly pin compatible. This chip was programmed so that it replaced each of the lower case letters, in the American Standard Code for Information Interchange (ASCII), with a matrix of dots which is reproduced in Figure 2.8.

It was anticipated that the array data would suffer from what is called "pattern" noise, as do CCDs. This "noise" is a consequence of each element sitting at its own DC level. Initially the pattern noise was thought to consist of alternate high and low DC offsets. The minimum of the data from the first element was then removed from the rest of the data from odd numbered elements. The process was then repeated for the second element with all even numbered elements. This did not remove the pattern noise, as was initially thought, and the grey scale pattern was degraded to such an extent that a  $k=3$  magnitude star could not easily be distinguished among the streaks ( see Figure 3.1 ).

The display routine was far too complex to attempt to change the software at the observatory, and since the rest of the software routines and apparatus seemed to be



GREY SCALE CHARACTERS USED ON THE VDU.

Figure 2.8

functioning satisfactorily, the observing programme was continued.

ii) Second trip to Tenerife

The software was completely rewritten for this trip, with the CID free running (ie integrating then sending the data to the microprocessor). This was to prevent any charge build up on the detectors, which occurred on the earlier trip.

The software routine executed for one complete scan was as follows :-

1] It asked the user for the number of positive and negative scan positions, the number of mirror movements, before returning to the initial mirror position to check the background counts, the number of times the CID was to be read after each mirror step (since the CID needed a finite length of time to reach equilibrium, see Chapter 3), and the number of times the CID was to be read while the mirrors were stationary.

2] The mirrors were then moved to the most negative position set by the user. This position would be returned to for a reference reading after a given number of mirror movements.

3] The microprocessor would ignore a pre-defined number of reads from the electronics to allow the CID to reach equilibrium. The next stream of useful data

would then be stored in a temporary buffer until the stream had finished. Then while the CID started another integration, the microprocessor would transfer the buffer contents into the data storage area. The microprocessor would then check to see if there were any further integrations required while the mirrors were in the present position. If so, routine 3] would be executed with the exception that the CID was already in equilibrium.

4] The mirror position was then compared against its positive scan limit, defined earlier by the user.

If the mirror position is the same as the positive scan limit, the microprocessor would exit from the data collection routine. Otherwise, the routine would test to see if a reference reading was to be executed. Providing a reference was to be performed, the mirrors would be temporarily returned to the start position for the reference readings, and afterwards restored to their former position.

The mirrors would then be advanced one step, and the microprocessor would return control to routine 3].

On completion of the prior routines, the microprocessor could then display the data as a grey scale pattern on the VDU, after a small amount of processing of the raw data.

Briefly, the raw data was condensed down to a one byte number, transferred into the picture storage area, and then the minimum reading for each element was removed from the rest of the data for that element. This method was very

successful in eliminating the pattern noise. However, the picture was still severely degraded because certain detectors had very large dark currents ( refer to Figures 3.8 and 3.9 ).

With this improved pattern noise removal routine, it was possible to distinguish objects brighter than approximately 6<sup>th</sup> magnitude, after 4 seconds integration, from among the streaks due to bad elements.

## 2.5 THE DATA STORAGE MEDIA

On the first trip, the primary data storage medium was a Facit 4203 cassette unit. This unit was rather susceptible to the cold, and often ceased to function correctly. An attempt to alleviate the problem was to wrap the unit in an insulating blanket. This helped to retain some of its internally generated heat and proved to be successful. However, this was not really a suitable solution, and on the second trip the Facit was replaced with a more reliable storage medium.

The microprocessor, on the second trip, off loaded the accumulated data at the end of a scan to an APPLE micro-computer which not only saved the data on a floppy disc, but could also process the data further, although the latter was rather time consuming.

Paper tapes and, if really desperate, hard copies of the data could be used as back up media, but fortunately these were not required on either of the trips.

## 2.6 THE RECOVERY OF THE DATA

The data from the first trip were stored on special digital cassettes. The mainframe computer had a Facit 4203 cassette unit attached directly to it. The reading of the cassettes was therefore quite simple. However, on viewing the files saved on the mainframe, it was discovered that the data had been written with no carriage returns inserted anywhere in the file. This awkward problem, since Fortran programmes on the Cyber will only read in lines of maximum length 150 characters, was resolved by using a PASCAL programme, listed in APPENDIX B. This programme read the data, character by character, and wrote the data out in a coherent form, with carriage returns inserted at the appropriate places.

For the data from the second trip, machine code and BASIC programmes were written which made the APPLE emulate a VDU, with the exception that an escape character ( ESC ) entered on the keyboard would make the microprocessor read the relevant data file on floppy disc and then send it via the serial line onto a file on the CYBER.

The APPLE routines proved to be very successful, with FORTRAN programmes, on the CYBER, having no difficulty in reading the transferred data files.

## REFERENCES

LAWSON,P., "THE DEVELOPMENT OF A 10 MICRON IMAGING SYSTEM",  
Ph.D. thesis, Leicester University, 1981.

BADDILEY,C.J., Infrared Physics, Vol. 17, pp 393-404, 1977.

## **CHAPTER 3**

## CHAPTER 3

### 3.1 INTRODUCTION.

The data from the first and second trips will be discussed in the following sections. The pattern noise will be illustrated and the technique for removing it will be discussed. The relative sensitivities of the elements will be compared between the laboratory derived values and those obtained from the first and second trips data.

Astronomically interesting results on Saturn and Jupiter from the first trips data are discussed, followed by an obscured cluster observed on the second trip.

The image quality will be examined for the second trip and possible explanations of this poor image are proposed.

The section headings in this chapter are :-

3.1] INTRODUCTION

3.2] THE FIRST TRIP TO TENERIFE

3.3] THE SECOND TRIP TO TENERIFE

### 3.2 THE FIRST TRIP TO TENERIFE.

This trip was primarily to familiarize ourselves with the

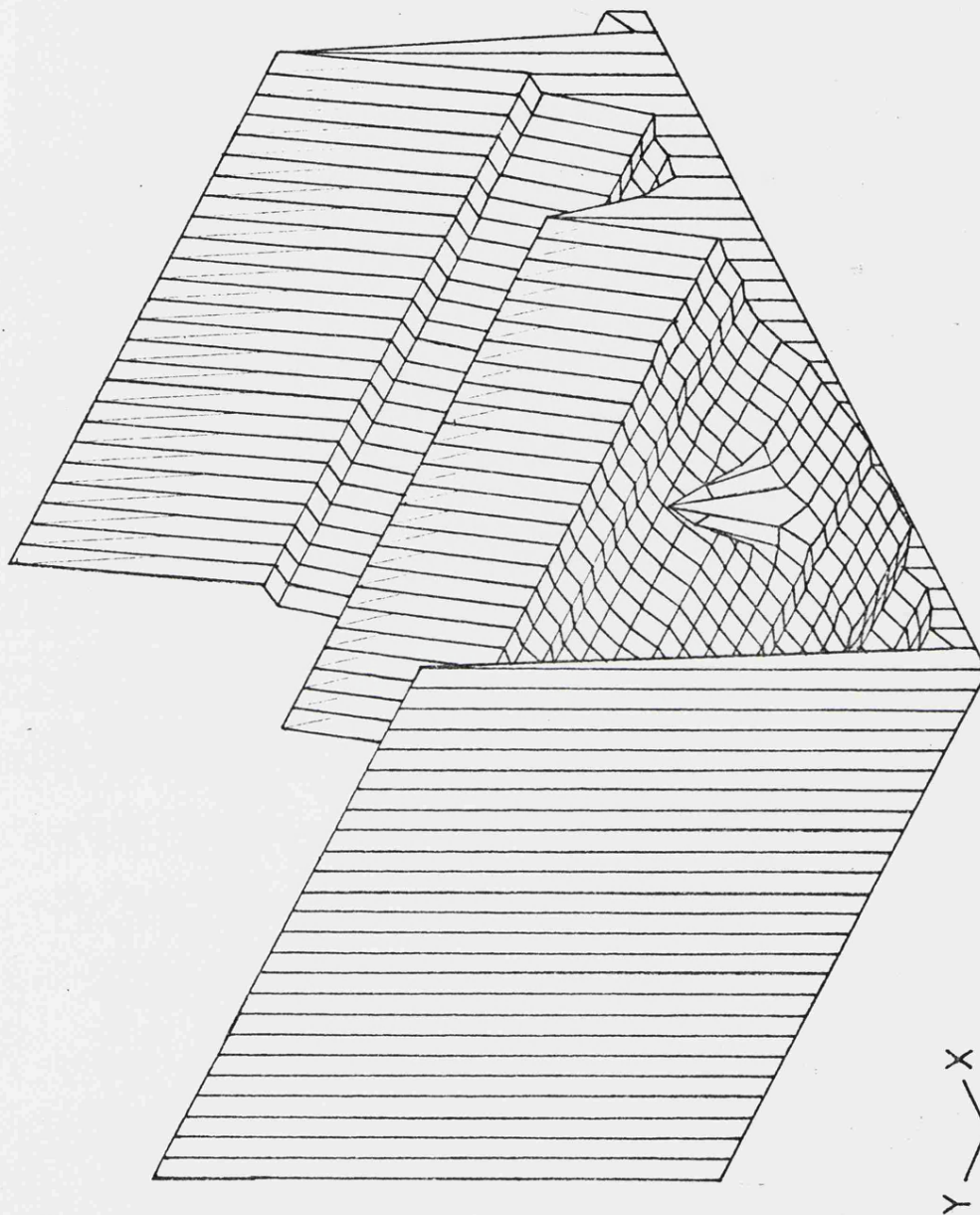
characteristics of the CID. Although the equipment worked well, there were improvements and alterations required on the software of the microprocessor, discussed in Chapter 2, which could only be done after the trip.

i) Pattern noise

As discussed in the preceding chapter, the pattern noise is a result of each element floating at a characteristic dark current level. Figure 3.1 shows the star Alcyone ( BS 1165, 2.96 magnitudes at K ) and is the sort of image obtained on the VDU at the telescope. The star is just visible among the pattern noise.

On the mainframe computer at Leicester the pattern noise was eliminated by removing the background level from each column of data ( ie the data associated with a particular element ). This background removal was accomplished by taking the data from each column of the scan and then calculating the mean and the corrected standard deviation of the data. However, if a source was present in the data column, the mean would be in error. Therefore, any data points more than three standard deviations above the mean were masked and the new mean and corrected standard deviation were recalculated. This was repeated until either no points were discarded or a minimum of ten points were remaining, ensuring that reasonable values for the mean and the corrected standard deviation were calculated. This mean was then removed from the data and the next column was then processed.

On completion of the above operation, the sensitivities



X = ARRAY AXIS.

Y = SCAN DIRECTION.

A THREE DIMENSIONAL PROJECTION OF BS 1165 DATA.

( WITH PATTERN NOISE )

Figure 3.1

were then normalized relative to element 16. The improved picture of BS 1165 is shown in Figure 3.2.

#### ii) Charge retention

The reader may have noticed that the image appears to be symmetric about the maximum for BS 1165, apparently indicating that the step size was correct. However, the CID retained charge<sup>1</sup> longer than anticipated resulting in the object being smeared in the scan direction. This charge retention only became apparent when the data was analysed at Leicester.

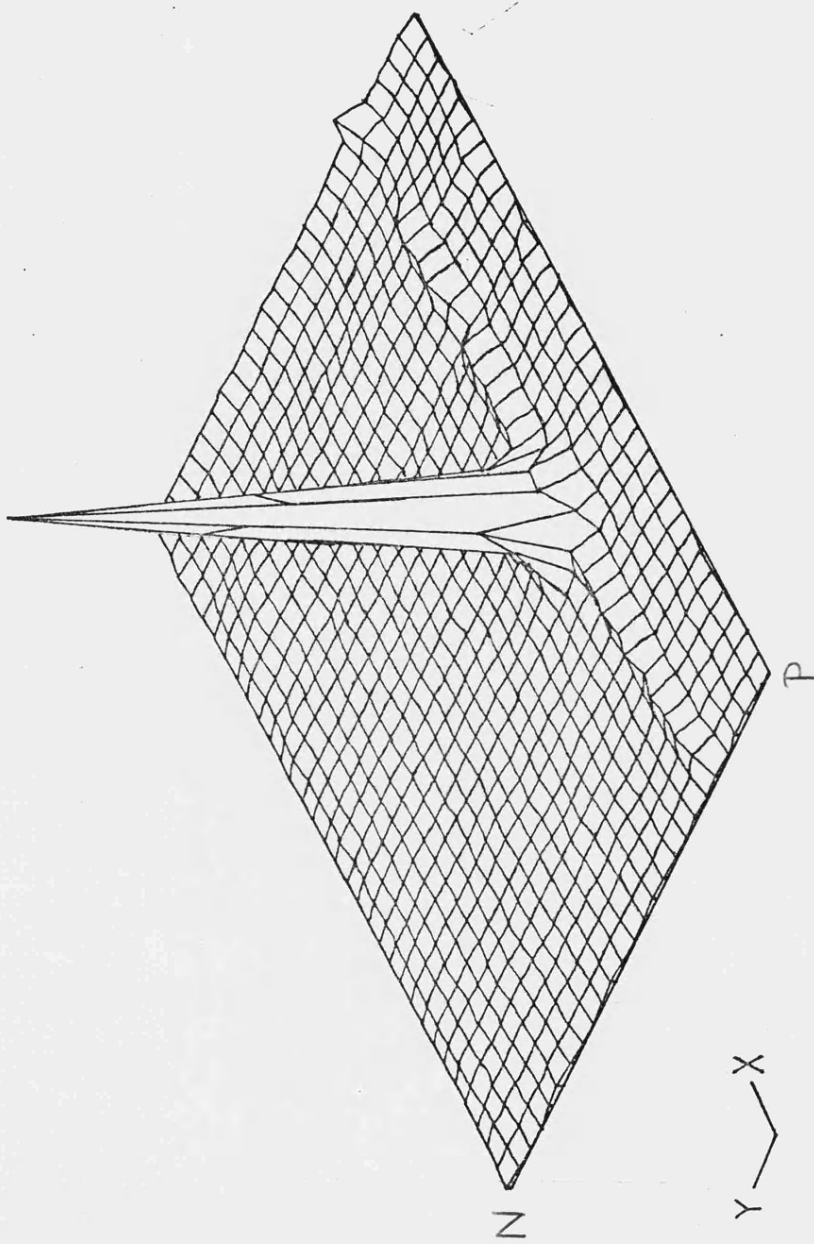
The ridge running across the columns in Figure 3.2 is a result of the CID integrating between scans ( refer to footnote on page 2.17 ). During this time the elements had reached saturation and the resulting ridge was very apparent on the displayed scans. A small amount of software reprogramming enabled the microprocessor to ignore a predefined number of reads of the CID. However, it was apparent from all the data scans that followed that this was not enough to clear the charge that had built up.

#### iii) Normalising the sensitivities of the elements

Each element in the array has a different sensitivity. To normalize these with respect to a particular element in the CID a source was needed which changed with time and also

---

<sup>1</sup> Warwick and Humrich (1984) found that the number of readout cycles taken to reach equilibrium increased as the input signal level diminished.



X = ARRAY AXIS.

Y = SCAN DIRECTION.

N = NEGATIVE STEP LIMIT.

P = POSITIVE STEP LIMIT.

IMPROVED PICTURE OF BS 1165.

( PATTERN NOISE REMOVED )

Figure 3.2

completely filled the field of view of the array.

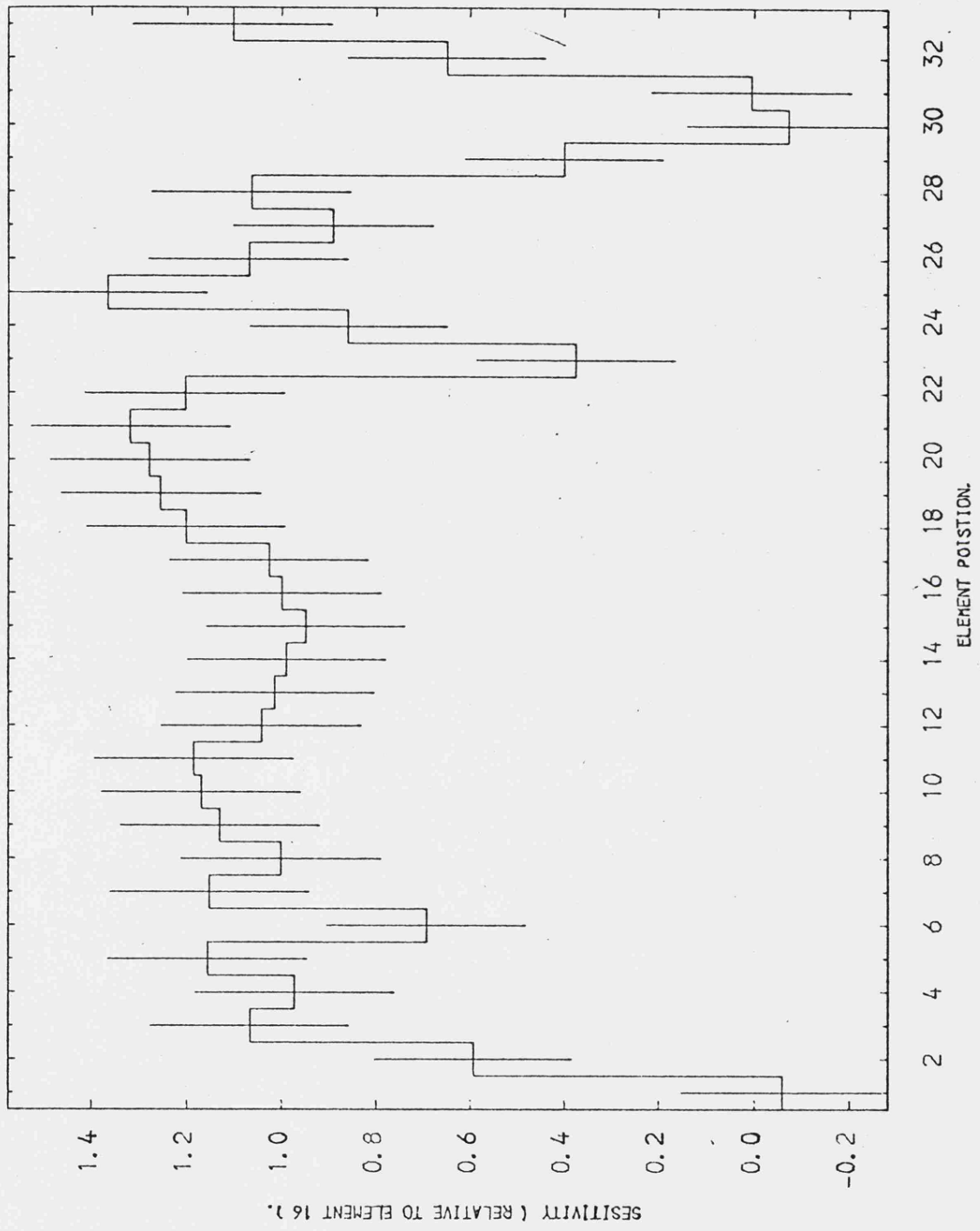
A source of this kind was not observed on this trip. However, the ridge running across all the scans served in establishing their sensitivities relative to element 16 ( Figure 3.3 ). These values compare well up to element 17 with those obtained in the laboratory by Warwick and Humrich (1984) ( Figure 3.4 ) and from the second trip ( Figure 3.5 ). Beyond element 17 there seems to be very little correspondence between the three.

Element 1, 30 and 31 appear, from Figure 3.3 and 3.4, to be almost totally insensitive. Moreover, 2, 23 and 29 have low sensitivities. All these poor elements occur at the ends of the array. Consequently we endeavoured to confine the sources observed to the central 16 elements.

#### iv) The Observations

Most of the observations were confined to bright objects. Few astronomically significant results could be drawn from the scans because the mirror step size was twice the detector size and the charge retention caused the image to smear in the scan direction.

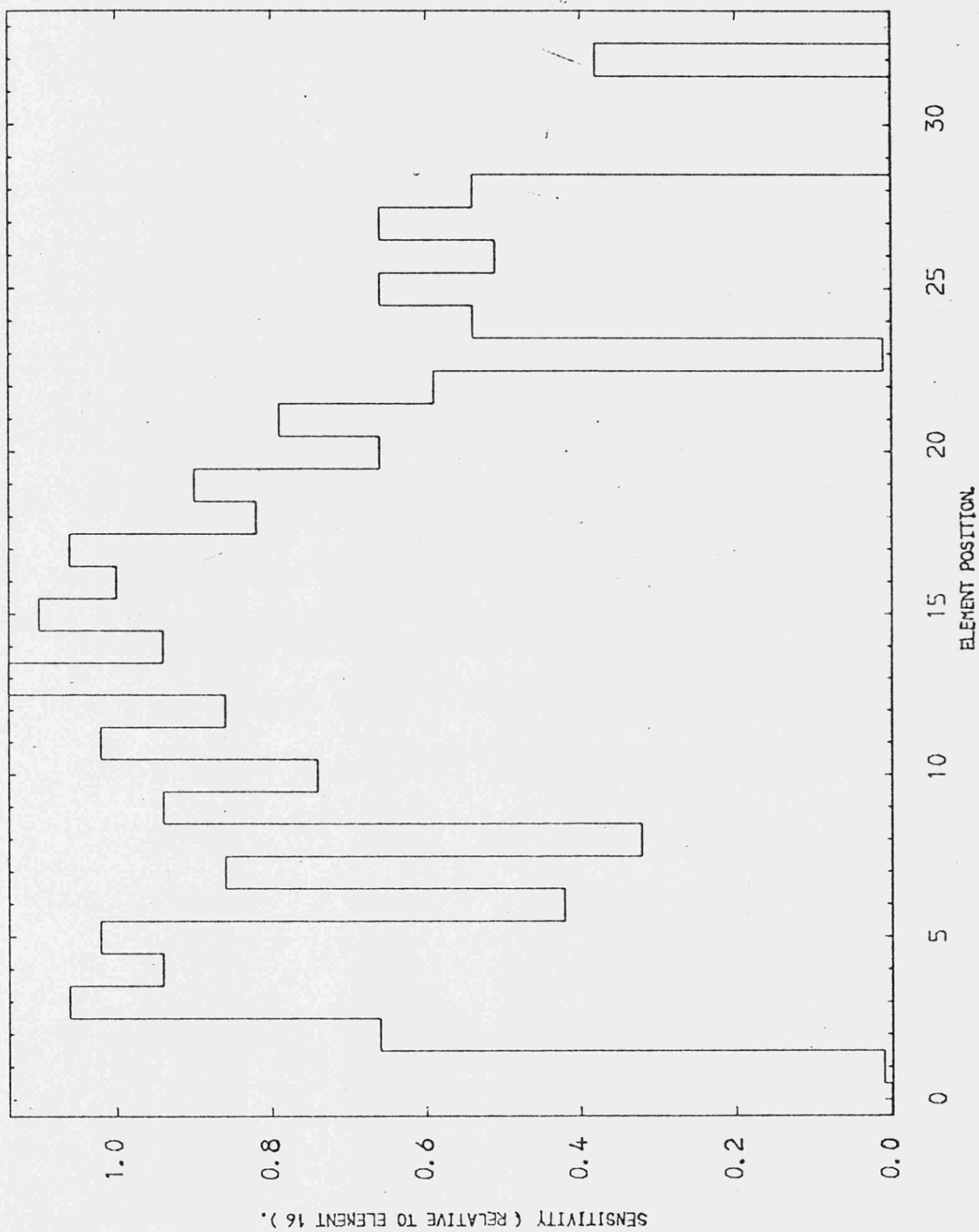
The scan of most interest was that of Saturn. This scan, reproduced in Figure 3.6, shows the rings of Saturn to be the most prominent feature at  $2.2\mu\text{m}$ . This can be explained by considering the major constituents of the rings and the planet. The rings consist mainly of water ice ( Clark and McCord (1980) ) whereas the upper atmosphere of the planet is a mixture of molecular Hydrogen (  $\text{H}_2$  ), Helium (  $\text{He}$  ), Methane (  $\text{CH}_4$  ) and Ammonia (  $\text{NH}_3$  ). Methane and Ammonia



RELATIVE SENSITIVITY FROM THE FIRST TRIP.

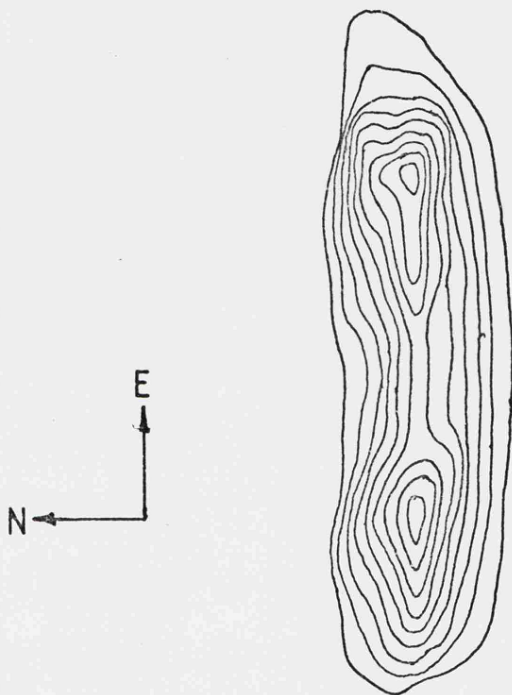
Figure 3.3





RELATIVE SENSITIVITY FROM THE SECOND TRIP.

Figure 3.5



EAST = SCAN DIRECTION ; NORTH = ARRAY AXIS.

VERTICAL SCALE = 2 x HORIZONTAL SCALE.

CONTOUR INTERVAL : 14,563 COUNTS.

CONTOUR PLOT OF SATURN SHOWING THE BRIGHT RINGS.

Figure 3.6

have absorption features at 2.3 and 2.2 $\mu$ m respectively ( Fink and Sill (1982) ). Consequently the light reflected from the planet's "surface" is much lower than that from the rings. A 2.2 $\mu$ m image of Saturn and its rings, made by D.Allen and J.Bailey, was later printed in the Report of the Anglo-Australian Telescope Board, 1<sup>st</sup> July 1981 to 30<sup>th</sup> June 1982.

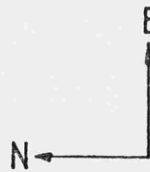
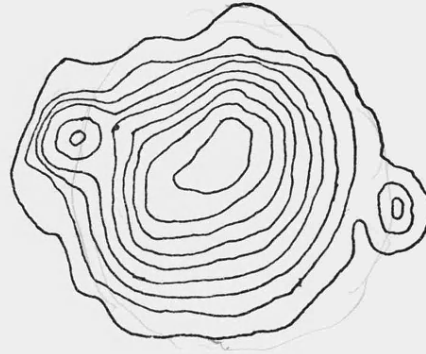
The scan of Jupiter ( see Figure 3.7 ) shows some strange features. The polar regions appear to be almost as bright as the central region. The ices of Ammonia ( NH<sub>3</sub> ), Ammonium Sulphide ( NH<sub>4</sub>HS ) and CH<sub>4</sub> have absorption features at 2.2, 2.2 and 2.3 $\mu$ m respectively ( Fink and Sill ). This would tend to rule out any reflection from the poles and would also indicate that the emission was occurring high in the atmosphere above them. Caldwell et al (1980) conducted observations at 8 $\mu$ m and concluded that the polar brightening was non-thermal in origin. These peculiar effects could be explained by aurorae which were proposed by Caldwell et al.

At the time of our observations, the Jovian spin axis was almost 90° to the direction of the Earth. This is why we were able to detect both poles at 2.2 $\mu$ m.

It should be noted that there is a certain amount of doubt about the relative brightnesses of the poles and the central region of the planet. This is because the planet was positioned on a poor response region of the array.

### 3.3 THE SECOND TRIP TO TENERIFE

i) Pattern noise and bad elements



EAST = SCAN DIRECTION ; NORTH = ARRAY AXIS.

VERTICAL SCALE = 1 x HORIZONTAL SCALE.

CONTOUR INTERVAL : 4,083 COUNTS.

CONTOUR PLOT OF JUPITER SHOWING THE BRIGHT POLES.

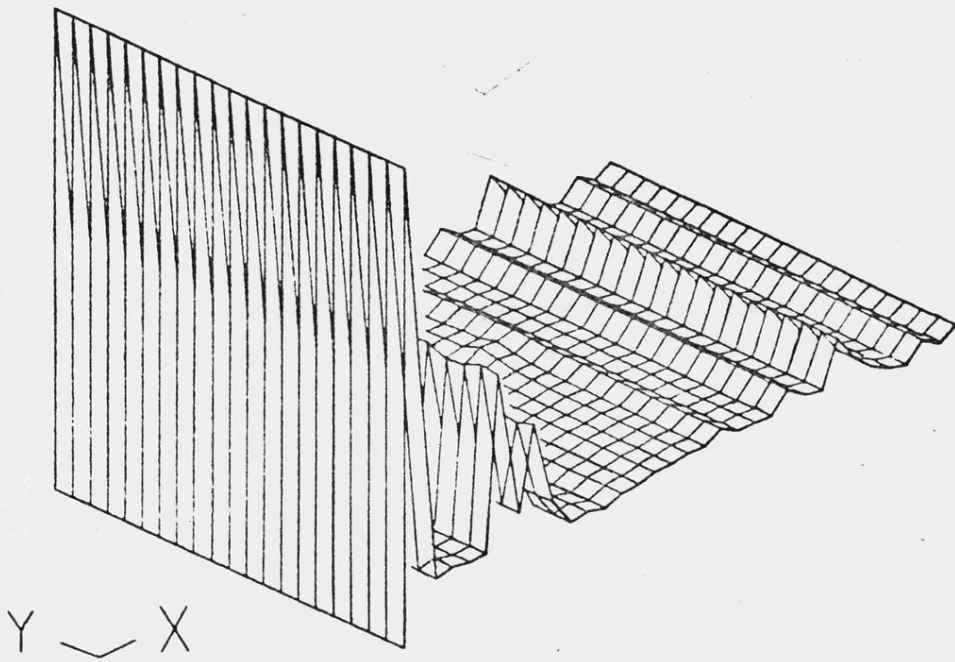
Figure 3.7

The processing of the pattern noise on the trip was discussed in Chapter 2 section 2.3 (ii). This method succeeded in removing the pattern noise. However, a new problem arose which was absent on the first trip. Certain elements had become extremely noisy ( compare Figures 3.2 and 3.8 (b) ). This was probably because the InSb array had no protective oxide layer and impurities may have diffused into the surface. These impurities can act as recombination sites, altering the characteristics of the element drastically. For example, increasing the dark current and/or decreasing the sensitivity. Removal of most of the impurities was achieved by boiling water in the inner helium tank for 12 to 24 hours, but, some of the impurities must have been rather more permanent resulting in a gradual degradation of the array.

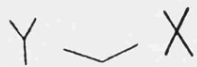
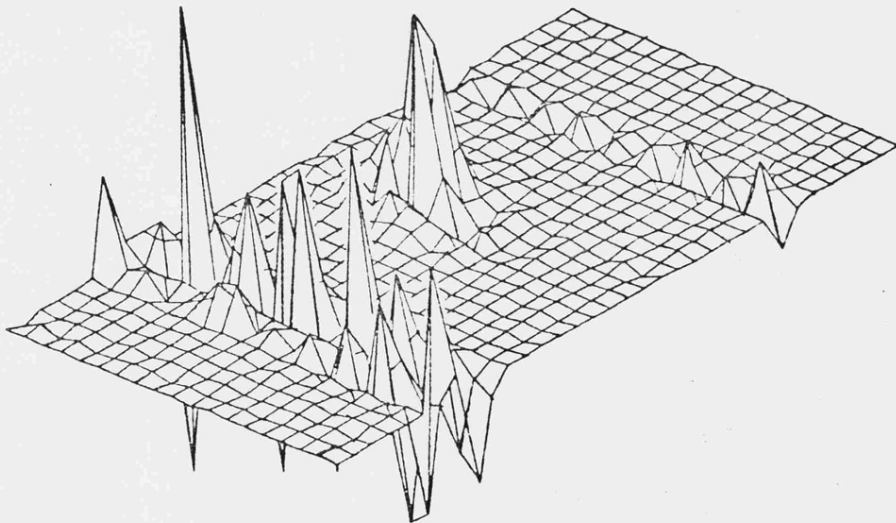
After pattern noise removal at Tenerife, these noisy elements debased the image, limiting the detectable sources on the screen to 6<sup>th</sup> magnitude after 4 seconds integration ( Figure 3.9 and 3.10 ).

Reduction of the data on the mainframe computer required the same operations as discussed in section 3.2 (i) with an additional routine for extrapolating the data from adjacent good elements. These good elements were also occasionally prone to intermittent spikes. These were removed by the same above method though the coordinates of the reading had to be supplied by the programme user.

Figure 3.10 is a contour plot of BS 8622 and shows clearly the effect of the bad elements. On masking the bad elements, a vastly improved image is generated ( see



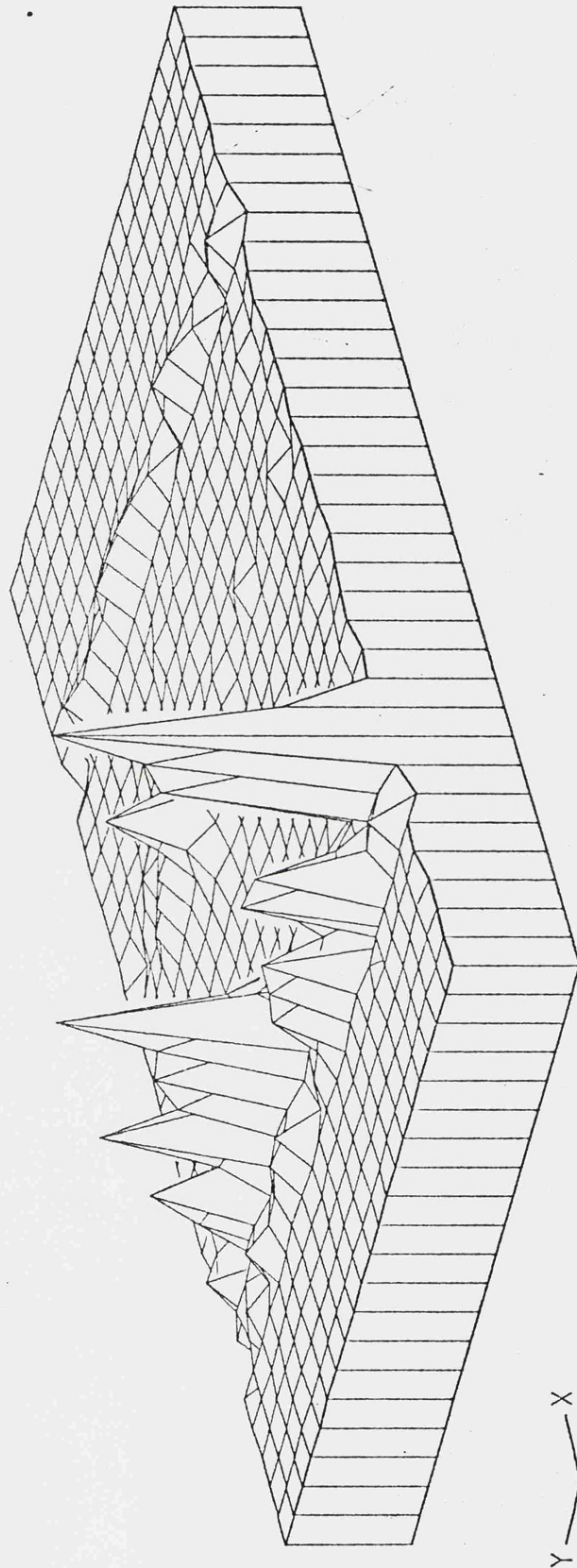
(a) WITH PATTERN NOISE.



(b) PATTERN NOISE REMOVED.

A THREE DIMENSIONAL PROJECTION OF BS 7236.

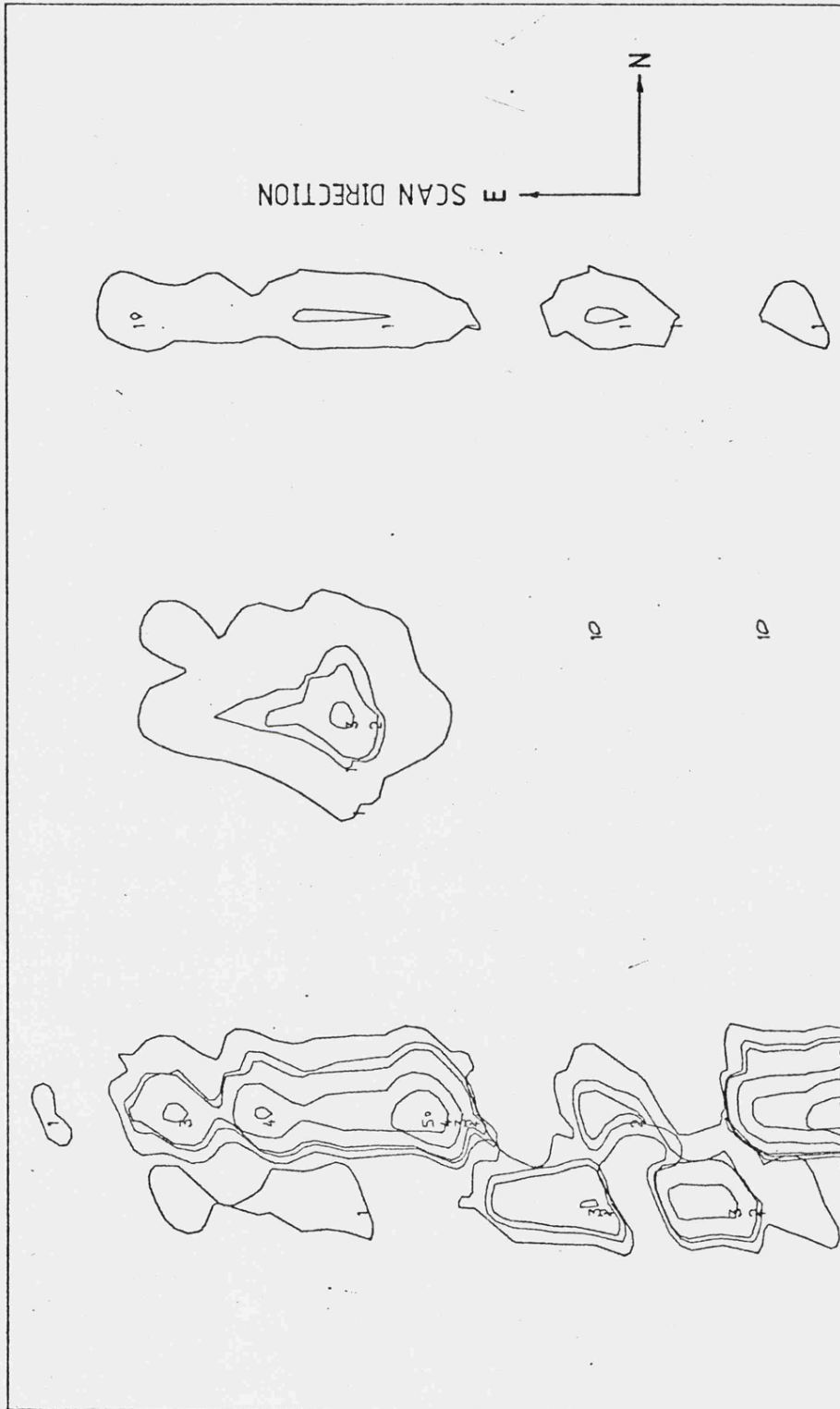
Figure 3.8



THREE DIMENSIONAL PROJECTION OF BS 8622.

( WITH NOISY ELEMENTS )

Figure 3.9



SIGMA= 11.06 EACH LEVEL= N<sup>2</sup>\*SIGMA

BS 8622.

CONTOUR PLOT OF BS 8622.

( WITH NOISY ELEMENTS )

Figure 3.10

Figures 3.11 and 3.12 ).

ii) Charge retention

Charge retention is still evident in Figures 3.11 and 3.12, even though a delay of approximately 3 seconds was inserted after each mirror movement. This confirms the findings of Warwick and Humrich ( see footnote in section 3.2 (ii) ).

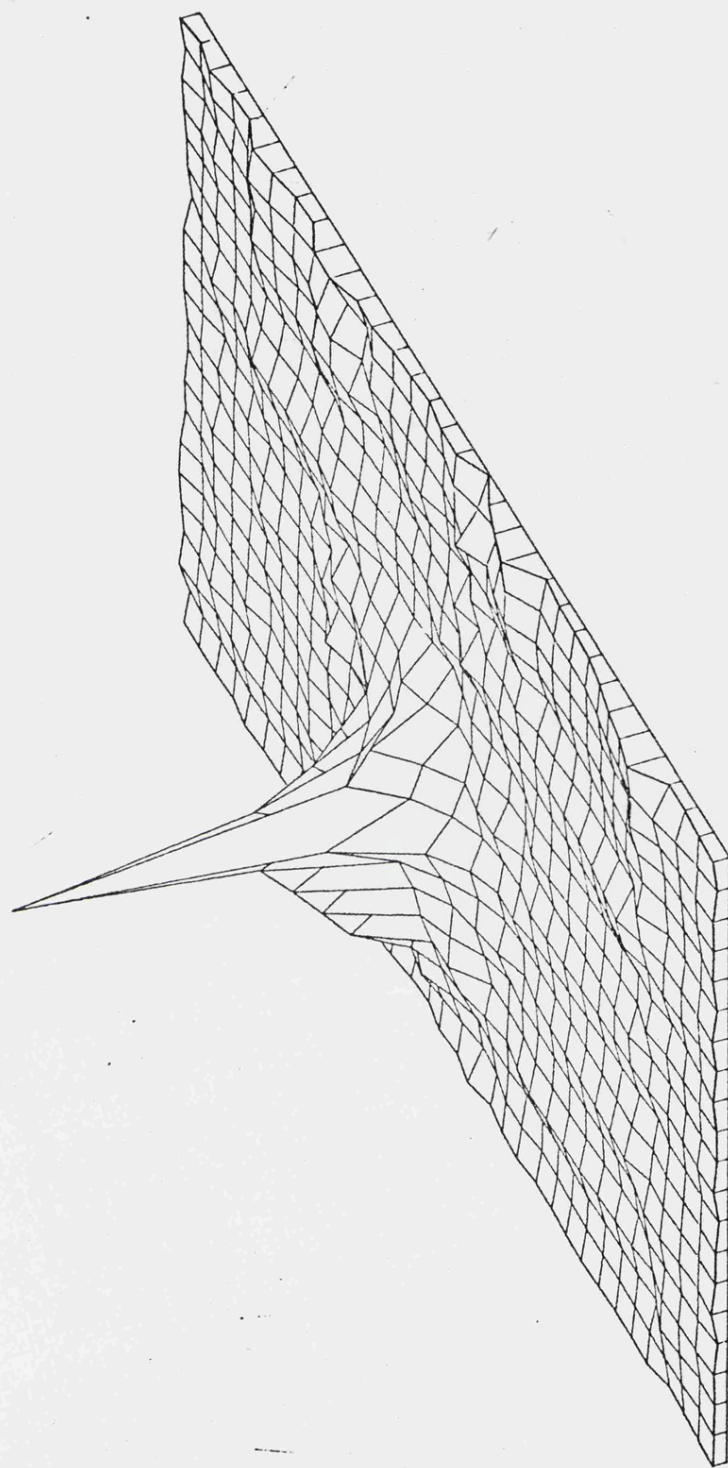
iii) Normalising the sensitivities of the elements

The method used to determine the relative sensitivities of the elements was to observe the dawn sky. This gave a source which completely filled the field of view of the array and was also changing with time.

The resulting estimates of the relative sensitivities are shown in Figure 3.5. They are in close accordance with the first trip and the laboratory determinations up to element 17. However, elements 18 to 33 seem to have no correlation between the three sensitivity plots, indicating that their characteristics change with each temperature cycle.

iv) Sky and Mirror drifts

Sky drifts were monitored throughout the scans by returning to the reference position after a set number of mirror movements, which was defined just before the scan



THREE DIMENSIONAL PROJECTION OF BS 8622.  
( NOISY ELEMENTS MASKED )  
Figure 3.11



SIGMA= 1.79 EACH LEVEL= N<sup>2</sup>\*SIGMA  
BS 8622

CONTOUR PLOT OF BS 8622.  
( NOISY ELEMENTS MASKED )

Figure 3.12

( see Figure 2.3 ).

On the mainframe computer at Leicester, a polynomial equation<sup>2</sup> was then fitted to these reference points. The DC offset of the curve ( ie the  $x^0$  term ) was ignored because some of the scans started on infrared sources. The curve was then subtracted from the data and, except for the first reference at the start of the scan, all the reference points were removed. This was repeated for all the elements in the scan.

This should have left the data free of any drift. The effect pointed out in Chapter 2, section 2.1, introduced an offset which was linear with the mirror displacement from the reference position. The best straight line and the corrected standard deviation for this effect were calculated. Any points above three standard deviations above the line were regarded as possible sources and were eliminated from the next calculation. The process was then repeated until either no further points were discarded, or a minimum of ten points remained. This line, along with the  $x^0$  term, was removed from the data. This removed the pattern noise on the data as well as the mirror displacement effect.

The above procedure was conducted on all of the elements in the array and, along with the masking of the noisy elements, a clean picture remained ( Figure 3.11 and 3.12 ).

#### v) Image Quality

---

<sup>2</sup> For N reference points in the scan a polynomial of order N-1 was applied.

From Chapter 2 the image produced by the lens should have concentrated nearly all the light onto one element of the array from a point source. On analysing the data from the standard star BS 8622, a maximum of 11% of the total light from the star was incident on one pixel and approximately 40% on the nine pixels centred on the maximum.

The cryostat, when opened in Tenerife, was discovered to have a layer of oil deposited on all the surfaces, including the lens and filters, in the outer vacuum chamber. This was cleaned off and the cryostat was evacuated and baked again. However, on returning to Leicester it was discovered that there was yet more oil on the surfaces in the outer vacuum chamber. This oil, which was thought to originate from the Getter when it was baked, condensed on all the optical surfaces and was the most probable cause of the poor image quality and the low sensitivity obtained.

#### vi) The Observations

Most of the observations were of an obscured cluster in the galactic plane. Figure 3.13 is a mosaic of scans pieced together to illustrate the relative positions, but the contours do not indicate the relative brightnesses of the stars.

This cluster was first discovered by Eaton et al (1984). Table 3.1 shows the K magnitudes determined from the scans and the V, J, H and K magnitudes from Eaton et al.

The brightest star in the cluster, star 2, is in good

STAR NO. DATA.	H	M	S	°	"	V	J-H	H-K	K SCAN	
						$\pm 0.05$	$\pm 0.02$	$\pm 0.03$	$\pm 0.03$	$\pm 0.04$
1	18 42	0.2	-3 20	6	15.96	1.32	0.61	5.61	5.29	
2	18 42	2.8	-3 18	41	>17.7	1.79	0.88	4.72	4.70	
3	18 42	2.9	-3 17	22	>17.7	1.95	0.88	5.50	5.03	
4	18 42	5.3	-3 18	25	>17.7	1.94	0.77	6.79	6.86	
5	18 42	6.8	-3 16	43	>17.7	2.53	1.14	5.42	4.91	
6	18 42	9.2	-3 18	40	>17.7	1.63	1.33	5.86	5.30	
7	18 42	11.0	-3 16	58	>17.7	1.88	0.82	6.69	6.70	
8	18 42	14.6	-3 18	42	>17.7	2.48	1.11	6.38	5.72	
9	18 42	9.5	-3 19	57	-	-	-	-	~7.16	

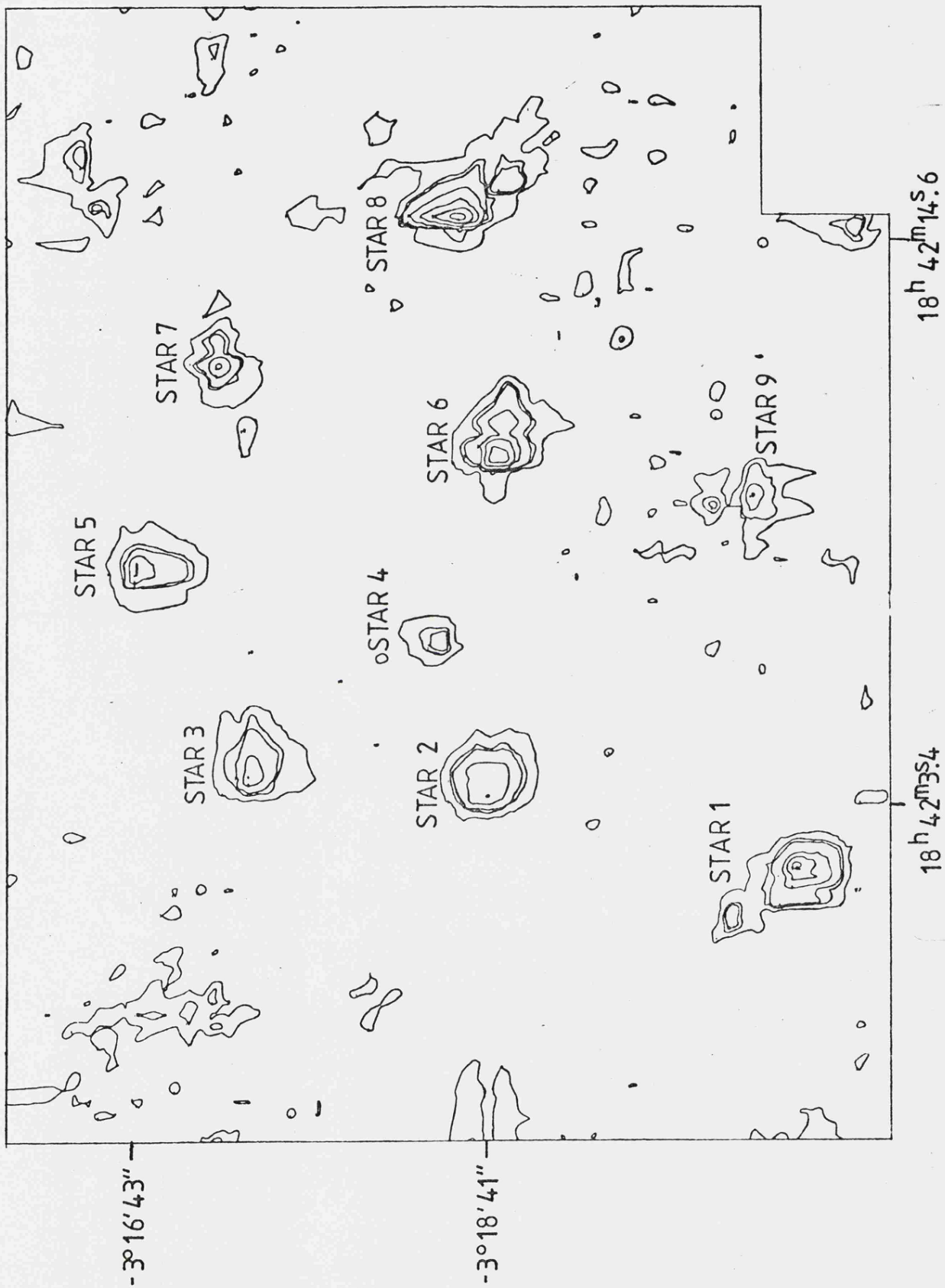
TABLE 3.1

agreement with Eaton et al estimates. However, the stars brighter than 6.5 magnitudes are above Eaton et al estimates because of the charge retention of the CID at low light levels. Sources fainter than 6.5 magnitudes drop below Eaton et al estimates because the counts ignored below the one sigma level become more significant in comparison to the star's total counts even with the image smearing. Star 9 is an extra source which Eaton et al did not discover. This star appears to be a double source with a separation of approximately 12" of arc. Stars 1 and 8 also appear to be doubles with separations of approximately 29" of arc and 19" of arc respectively. It should be noted that the word 'double' does not imply that these sources

are gravitationally bound.

The array's sensitivity was limited to 7.5 magnitudes for a 1 standard deviation detection in 1 second. However, if all the light from a point source, such as a star, fell on one element, then the limiting magnitude would have been 10.38 magnitudes for a 1 standard deviation detection in 1 second.

The other observations consisted of scans of the nuclei of galaxies. However, because of the array's limiting sensitivity of approximately  $10^{\text{th}}$  magnitude per square arcsecond for a 1 standard deviation detection in 1 second, most of the objects were undetectable.



MOSAIC OF SCANS OF OBSCURED GALACTIC PLANE CLUSTER.

Figure 3.13

## REFERENCES

EATON,N., ADAMS,D.J., and GILES,A.B., Mon. Not. R. astr. Soc., in press, 1984.

CALDWELL,J., TOKUNAGA,A.T., and GILLETT,F.C., Icarus, Vol. 44, pp 667-675, 1980.

CLARK,R.N., and McCORD,T.B., Icarus, Vol. 43, pp 161-168, 1980.

FINK,U., and SILL,G.T., in COMETS, ed. L.L.Wilkening ( TUCSON: University of Arizona Press ), p 164, 1982.

WARWICK,R.S., and HUMRICH,A., AN EVALUATION STUDY OF A CHARGE INJECTION DEVICE FOR APPLICATION IN FOCAL PLANE INSTRUMENTATION FOR UKIRT, Dec. 1983.

## **CHAPTER 4**

## CHAPTER 4

### 4.1 INTRODUCTION

There is a substantial amount of evidence which indicates that spiral galaxies have massive halos associated with them. This evidence comes mainly from the flat rotation curves, obtained from the 21cm hydrogen line, which extend as far out as 100kpc from the nuclei of many galaxies ( eg Haschick and Burke (1975) and Krumm and Salpeter (1977) ). These massive halos must possess very large mass-to-light ratios, otherwise they would be easily detected in the optical and infrared.

An optically luminous halo around NGC 4565 was discovered by Hegi and Gerber (1977) and later in the infrared by Hohlfield and Krumm (1981). Hohlfield and Krumm also tentatively suggested that they had detected halos around NGC 2768, 4203 and 4762.

NGC 2683 is an Sb galaxy which is almost edge on with a position angle ( PA ) of  $42^\circ$  ( Mayall and Lindblad (1970) ). Simkin (1975) scanned the minor axis of the galaxy in an effort to detect an optical halo. A suggestion of one was found. In an attempt to confirm this, scans were

conducted in Right Ascension ( RA ), by Dr.A.Adamson and Dr.D.J.Adams, through the nucleus at three wavelengths.

Two methods were used to analyse the data sets produced. The first was to deconvolve the data with the beam profile. The halo should then become apparent as wings extending out from the nuclear bulge and should become more prominent with increasing wavelength ( ie V to K ). However, the deconvolution method had a fundamental stumbling block, which is discussed in a later section, and had to be rejected. The second method was to compare the V-J and V-K colours with radial distance from the nucleus. This proved to be more successful than the deconvolution method.

This chapter is subdivided into the following sections :-

- 4.1] INTRODUCTION
- 4.2] THE DATA
- 4.3] THE INVERSE MATRIX DECONVOLUTION METHOD
- 4.4] THE "BEST FIT" DECONVOLUTION METHOD
- 4.5] COLOUR INDICES OF NGC 2683

## 4.2 THE DATA

The data, supplied by Dr.A.Adamson, was over sampled by a factor of 6.

$$\text{Over sampling} = \frac{\text{Beamsize}}{\text{Integration time} \times \text{scan rate}}$$

Beam size = 50 arcseconds.

Integration time = 5 seconds.

Scan rate = 1.806 arcseconds/second.

$$\text{Over sampling} = \frac{50}{5 \times 1.806}$$

Over sampling was necessary for deconvolution to be performed. This is because it effectively converts the beam size from six integrations wide ( 6 bins ) to one bin wide. The deconvolution should allow us to pick out fine detail in the scan data ( ie sources with a diameter greater than 8" of arc in the scan direction ).

#### 4.3 THE INVERSE MATRIX DECONVOLUTION METHOD

If we consider the two dimensional matrix of the beam profile,  $B(n \times n)^1$ , where  $n$  is the number of data points in the scan, the product of this matrix with the clean deconvolved data matrix,  $D(1 \times n)$ , will reproduce the observed data matrix,  $C(1 \times n)$ .

$$C(1 \times n) = D(1 \times n) \times B(n \times n) \quad \dots [4.1]$$

To convert the observed data matrix,  $C(1 \times n)$ , back to the deconvolved data,  $D(1 \times n)$ , we must multiply both sides of equation [4.1 by the inverse of the matrix  $B(n \times n)$ . Remembering that  $B(n \times n) \times B^{-1}(n \times n) = I(n \times n)$ , which is the

---

<sup>1</sup> If the beam profile is ( a b c d e ), where  $c$  is the maximum reading, the matrix  $B(n \times n)$  is :-

$$\begin{array}{l}
 n \text{ rows} \\
 \left[ \begin{array}{cccccccc}
 c & b & a & 0 & . & . & . & . & 0 \\
 d & c & b & a & . & . & . & . & 0 \\
 e & d & c & b & . & . & . & . & 0 \\
 0 & e & d & c & . & . & . & . & 0 \\
 . & . & . & . & & & & & . \\
 . & . & . & . & & & & & . \\
 0 & 0 & 0 & 0 & . & . & . & . & a \\
 0 & 0 & 0 & 0 & . & . & . & . & b \\
 0 & 0 & 0 & 0 & . & . & . & . & c
 \end{array} \right]
 \end{array}$$

n columns.

IDENTITY MATRIX, the resulting equation is :-

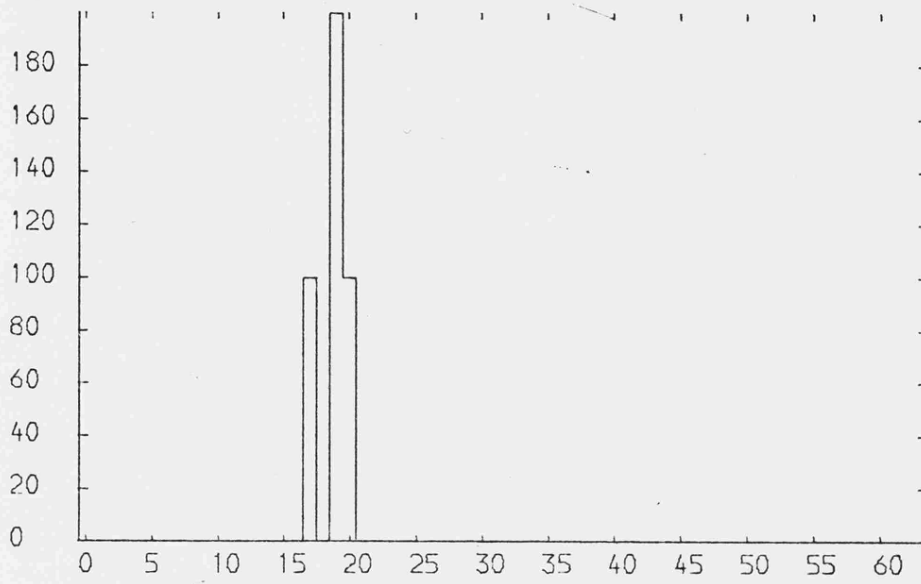
$$C(1 \times n) \times B^{-1}(n \times n) = D(1 \times n) \quad \dots [4.2]$$

So the deconvolved data can be returned if the inverse matrix of the beam is known. Fortunately a facility was available on the Cyber which would work out the inverse matrix of a two dimensional matrix.

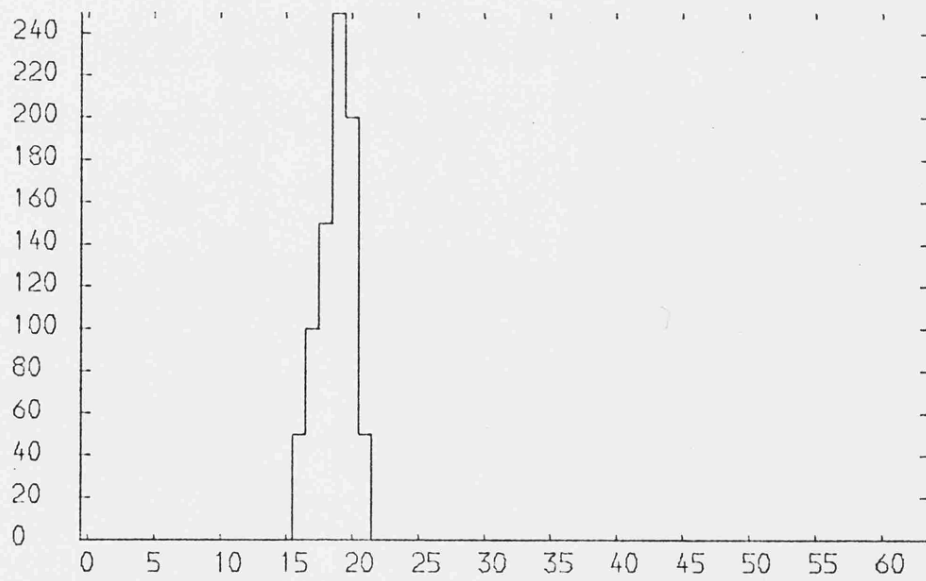
To test how the programme would perform, a file was created which had three artificial sources stored in it. Two sources were set to 100 counts and the third was 200 counts. These sources were then smeared with a beam profile of ( 0.5 1.0 0.5 ) and the smeared data and beam profile data were entered into the programme. Figure 4.1 shows the results, where (a) is the final deconvolved data and (b) is the initial smeared data.

The deconvolving routine has managed to recover the original source counts and their positions exactly.

This would be excellent if the data collected only suffered from beam smearing. However, all observational data carries noise. Therefore, a small amount of noise was added to the smeared data and the programme was executed once again, this time with rather catastrophic results ( see Figure 4.2 ). The routine had found the solutions but they were clearly wrong. This is not surprising, since the above matrix method is trying to solve the set of equations exactly and does not take the noise into account. Any noise on the data merely sends the solutions oscillating from large positive to large negative values, in an attempt to compensate for the noise. This was a major fault in the



(a) DECONVOLVED DATA.



(b) SMEARED SYNTHETIC DATA.

Figure 4.1

routine and so this method had to be rejected.

#### 4.4 THE "BEST FIT" DECONVOLUTION

If equation [4.1 is expanded into its long form, the following equations are obtained :-

$$C_1 = D_1 B_{11} + D_2 B_{21} + \dots + D_n B_{n1}$$

$$C_2 = D_1 B_{12} + D_2 B_{22} + \dots + D_n B_{n2}$$

$$C_n = D_1 B_{1n} + D_2 B_{2n} + \dots + D_n B_{nn}$$

These equations can be reduced to a simpler form :-

$$C_i = \sum_{j=1}^n B_{ji} D_j \quad \dots[4.3,$$

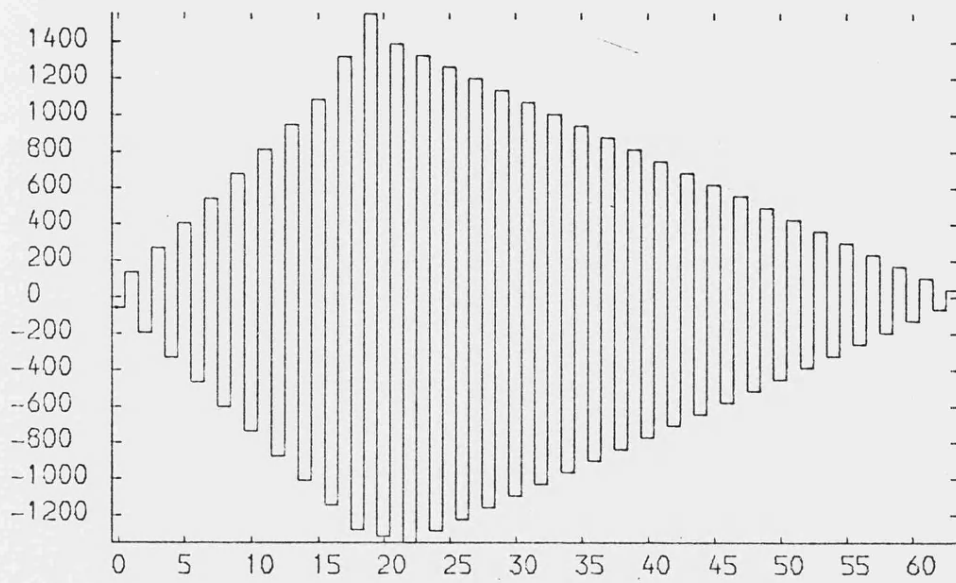
for  $i = 1$  to  $n$ . However, this would generate a set of equations which would suffer from the same problems as in section 4.3.

If an extra term is added to the left hand side of equation [4.3 it becomes :-

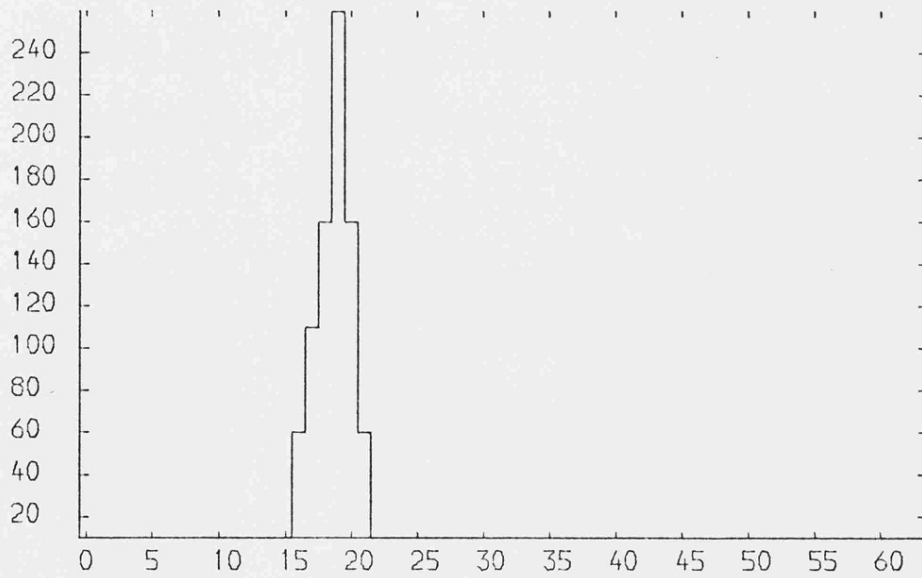
$$f_i = - C_i + \sum_{j=1}^n B_{ji} D_j \quad \dots[4.4,$$

for  $i = 1$  to  $n$  ( where  $f_i$  is known as the residual of the equation ). A routine was available on the Cyber which would minimise these residuals for the whole scan.

With this new routine installed in the programme the noisy synthetic data and the beam profile data were once



(a) DECONVOLVED DATA.



(b) NOISY SMEARED SYNTHETIC DATA.

Figure 4.2

again entered. Not surprisingly, the resultant deconvolved data still oscillated like the earlier method, but a significant reduction in the amplitude of the oscillations was obtained.

The reason that the oscillations persisted was that  $D_j$  could still take on large negative values which were caused solely by the noise. The only way to eliminate these negative values was to substitute  $D_j$  with  $D_j^2$  and so equation [4.4] became :-

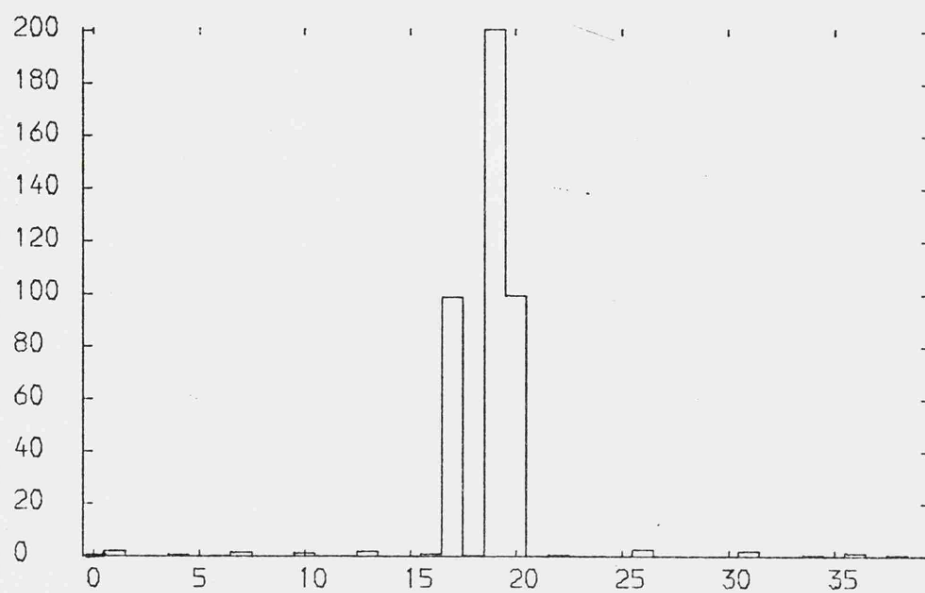
$$f_i = -C_i + \sum_{j=1}^n B_{ji} D_j^2 \quad \dots [4.5,$$

for  $i = 1$  to  $n$ .

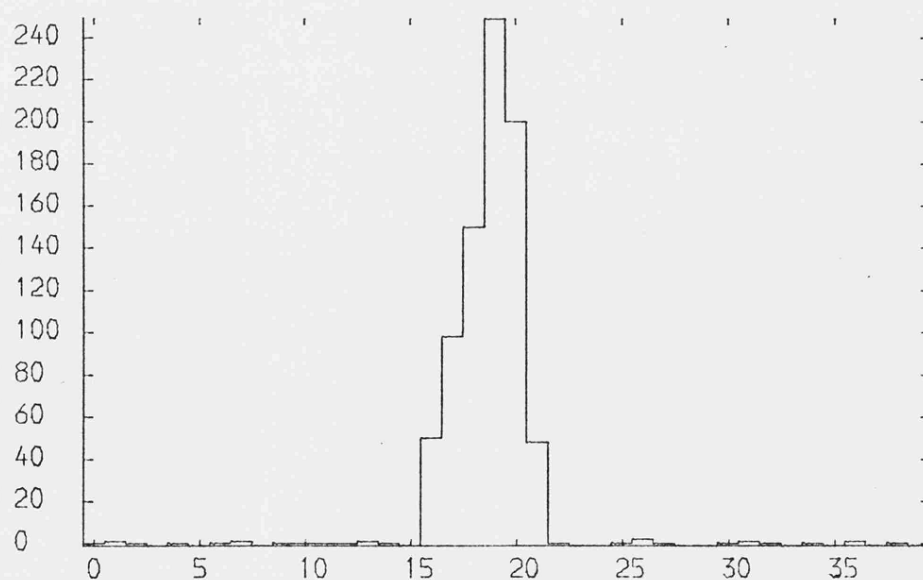
This improved method was almost completely immune to the noise on the data. The result of deconvolving the noisy synthetic data is shown in Figure 4.3 (a).

Now that the programme was deconvolving the noisy synthetic data it was time to process the scans of NGC 2683. However, a few extra steps were required before the data could be used.

Because the star, scanned for the beam profile, was at a different declination to the galaxy one must transform the RA beam profile scan of the star to the same declination and with the same integration time per bin as the RA scan of the galaxy. The background levels of the galaxy and the beam profile data were determined by taking the first and last ten points in the scans, checking beforehand that no source or bad points were in these regions. The galaxy data were then deconvolved producing the two sets of data in Figure 4.4 and 4.5 for the optical and infrared scans



(a) IMPROVED DECONVOLVED DATA.



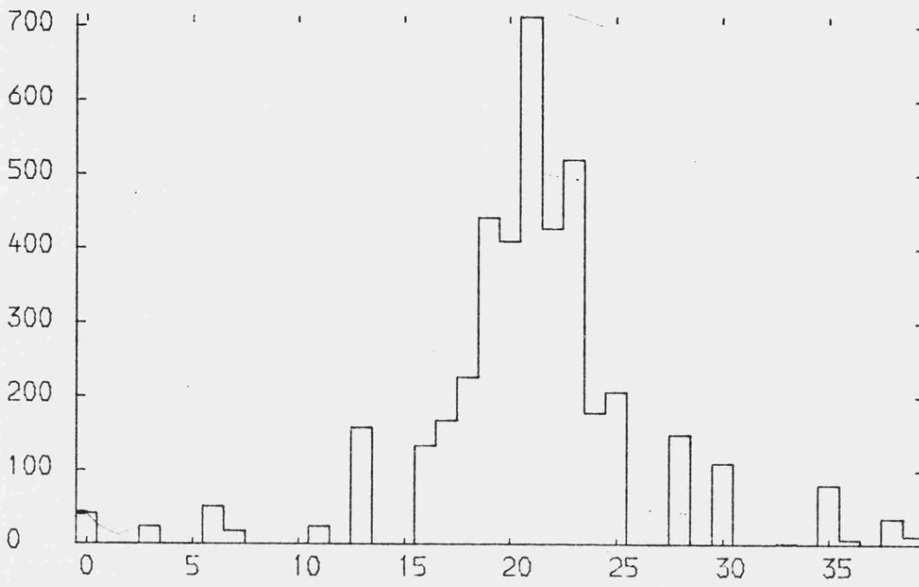
(b) NOISY SMEARED SYNTHETIC DATA.

Figure 4.3

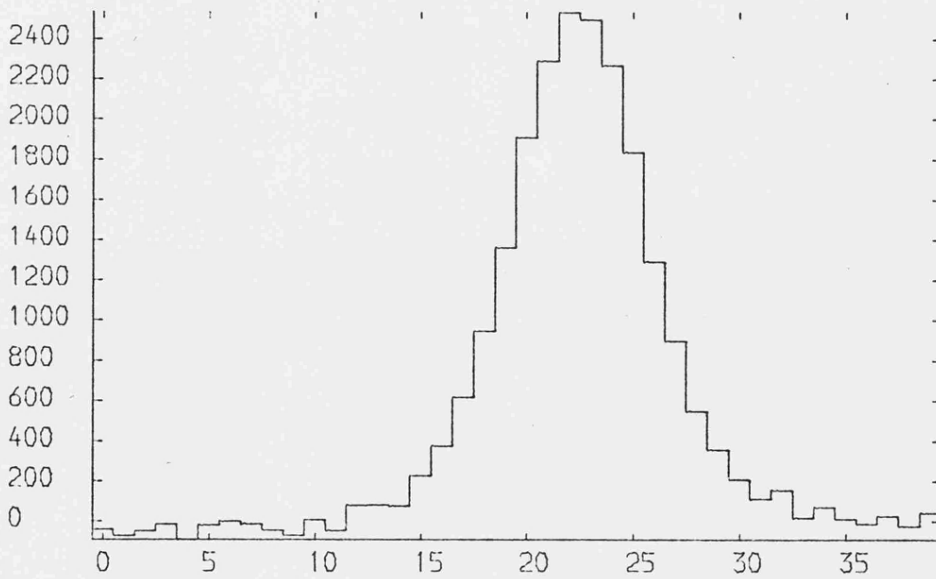
respectively. Plates 4.1 and 4.2 show the deconvolved optical and infrared scans superimposed on blue and red wavelength photographs. The routine has performed extremely well in picking out point sources as can be seen by the two faint stars and the spiral arm.

The errors on the deconvolved data were impossible to calculate. However, a method of testing the validity of a feature was found in a paper by Charles et al (1977) who were analysing the X-ray structure of supernova remnants. Their technique was to add on a Gaussian distribution of random numbers to the galaxy data set. This distribution had the same standard deviation as the background counts in the scans and a mean of zero. This was run several times through the deconvolution routine and any permanent features, such as the two stars and the spiral arm detections, were real features. The fine structures in the galaxy were found to change drastically with each run and, therefore, could not be regarded as real features.

These transient features were a result of diffuse objects not appearing to be true point sources in the beam. If one considers a string of sources, A, B, C, D and E, perpendicular to the scan direction and with C lying on the scan line which passes through the beam centre, then, on the first integration, source C enters the beam. However, on the second integration, sources B and D enter the beam causing excess counts to be added to those from source C. Similarly, on the next integration, sources A and E would enter the beam. This would continue until source C lay in the centre of the beam, after which the process would be reversed. This source illustrates how a true diffuse object



(a) DECONVOLVED DATA.



(b) RAW V DATA.

OPTICAL, V, SCAN DATA AND RESULTS.

Figure 4.4

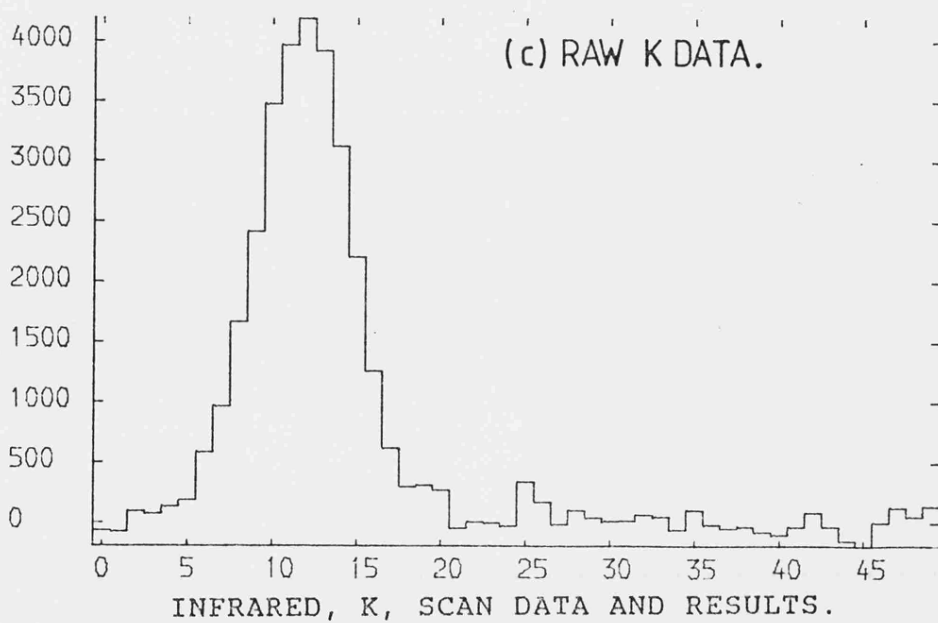
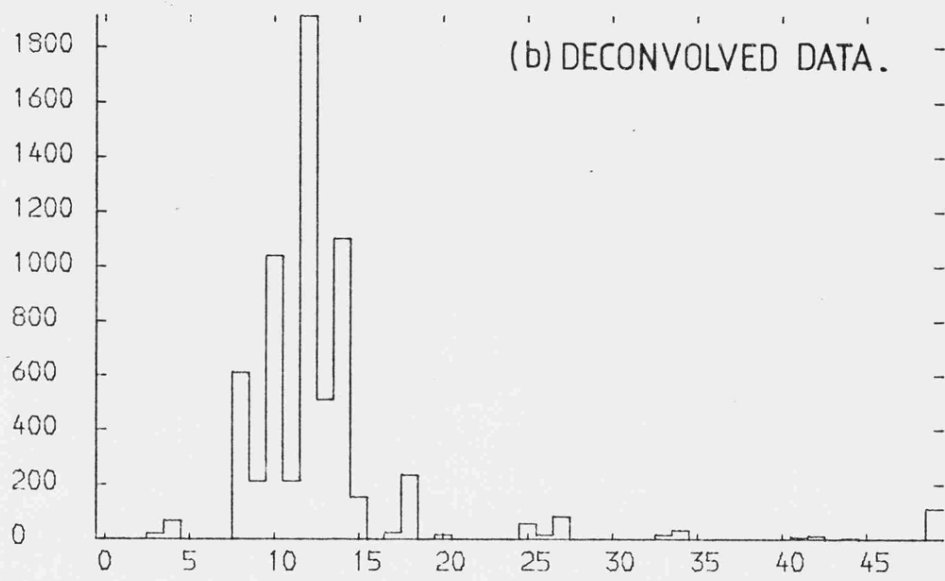
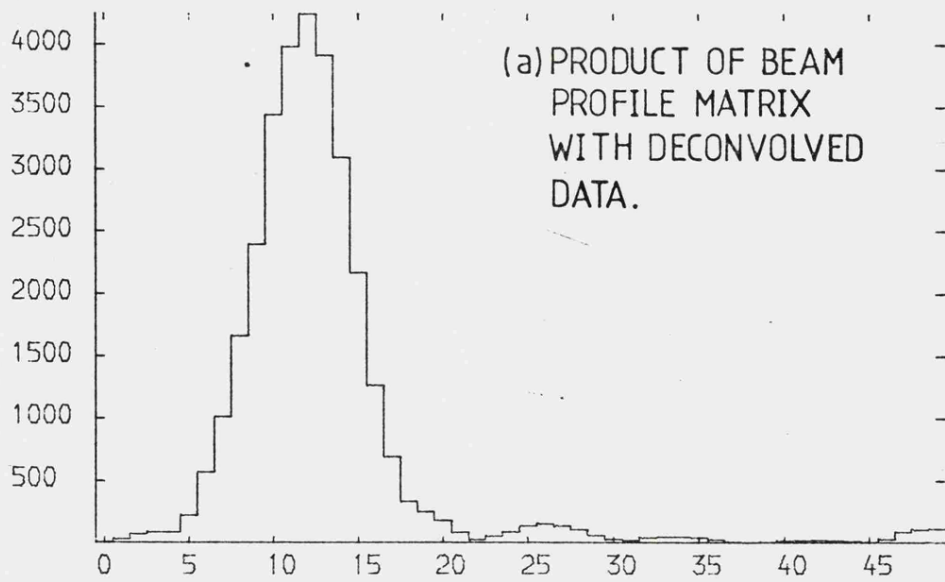
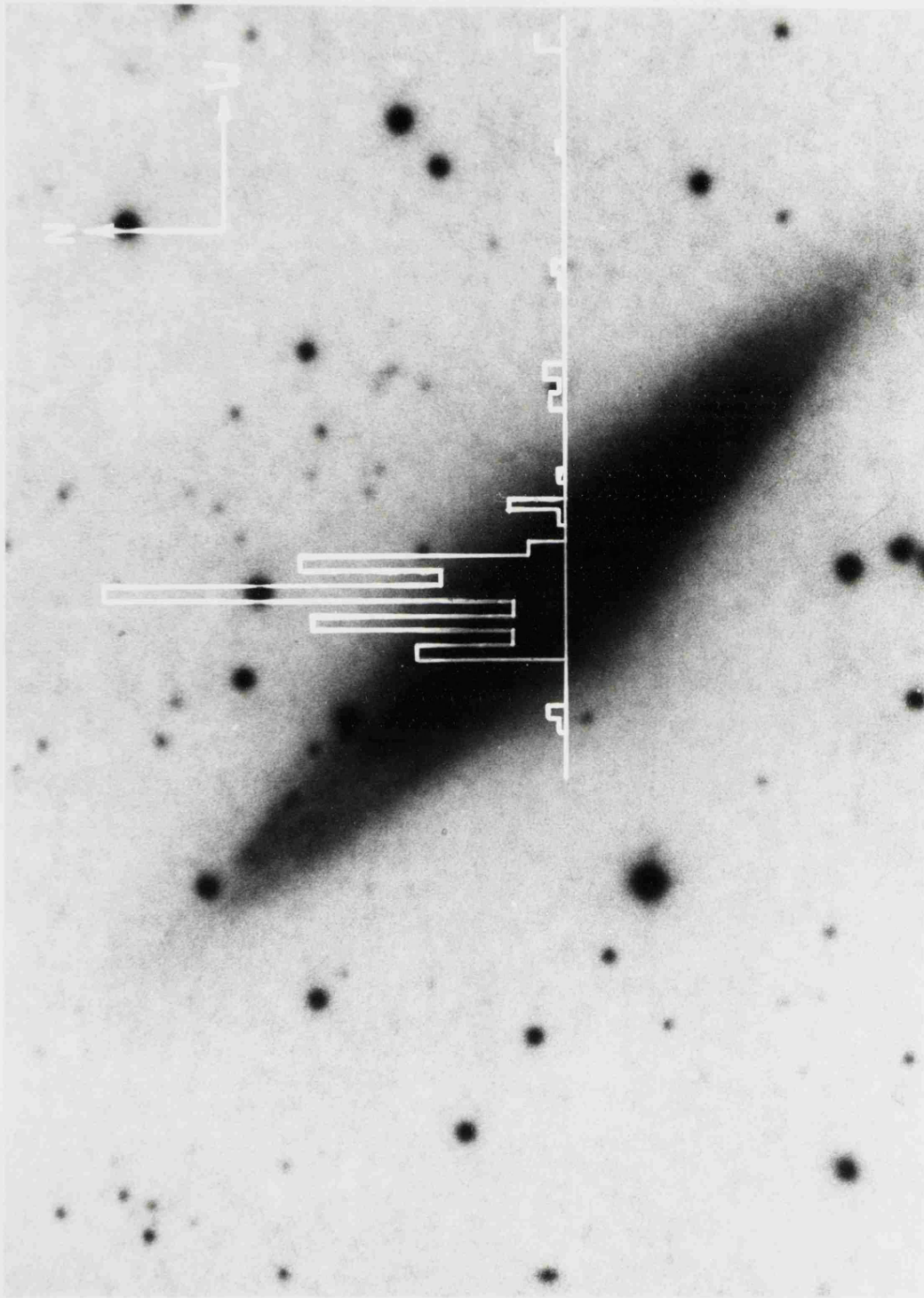
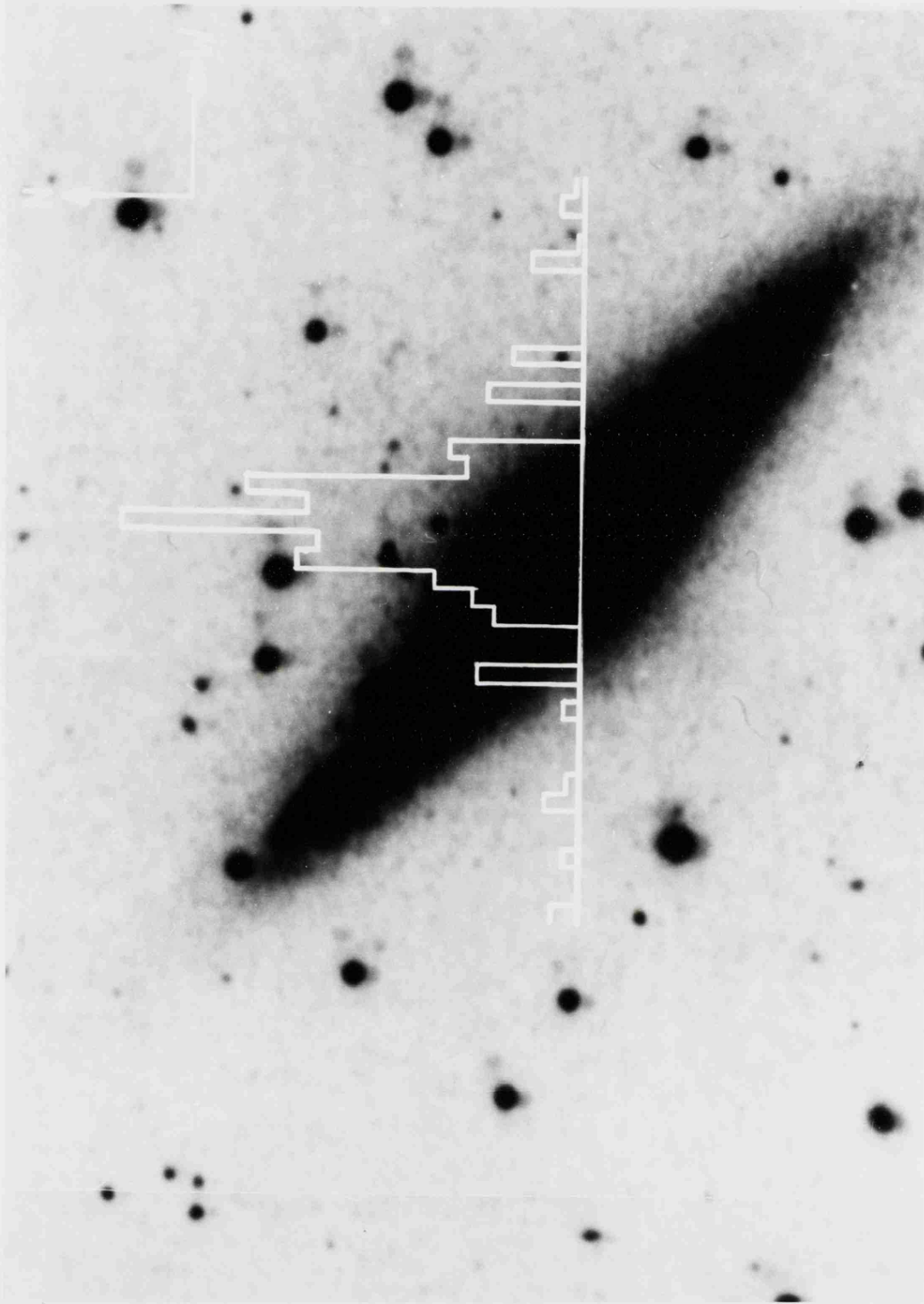


Figure 4.5



SCALE : 3.54 ARCSECONDS PER MILLIMETRE

PLATE 4.1



SCALE : 3.54 ARCSECONDS PER MILLIMETRE

PLATE 4.2

responds in the beam. The routine was, therefore, confused by these diffuse objects, resulting in it being unable to detect the faint wings of the halo. This routine would have worked if the circular beam had been replaced with a square ( or rectangular ) beam and the telescope scanned parallel to one of its sides.

As a result of this, the routine had to be rejected, even though it was capable of detecting a star of approximately 11.5 magnitudes at K for a one standard deviation detection in one second from the raw data.

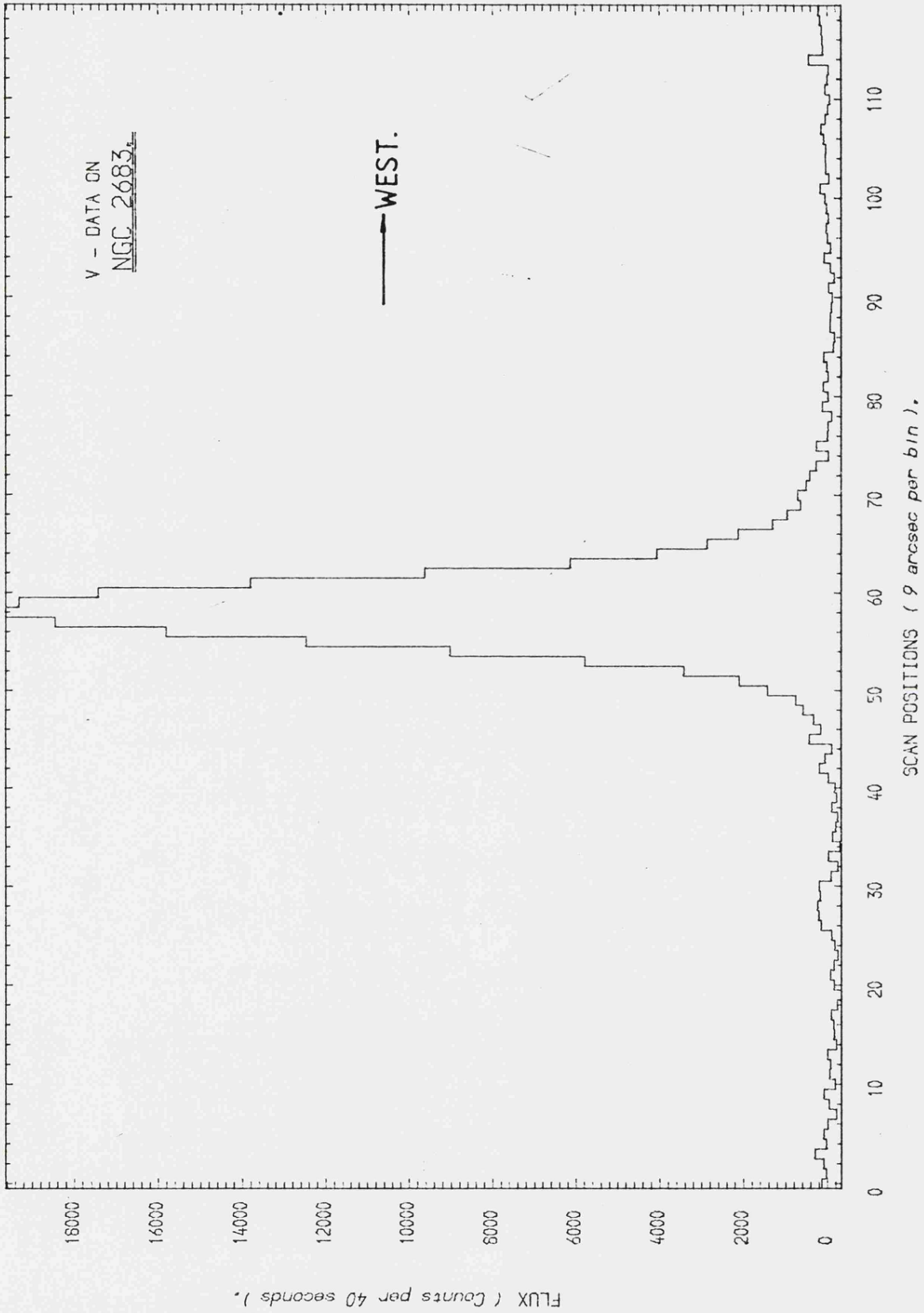
#### 4.5 COLOUR INDICES OF NGC 2683.

The number of scans of the galaxy for the K data was a factor of two less than the V and J scans ( Figures 4.6, 4.7 and 4.8 are all the relevant wavelength scans summed together ). As a result, the signal-to-noise for the K data was too poor and was, therefore, not used in the following method.

Background removal from the V and J scans was accomplished by setting windows in the data array over which the best straight line was determined. This was then removed from the data.

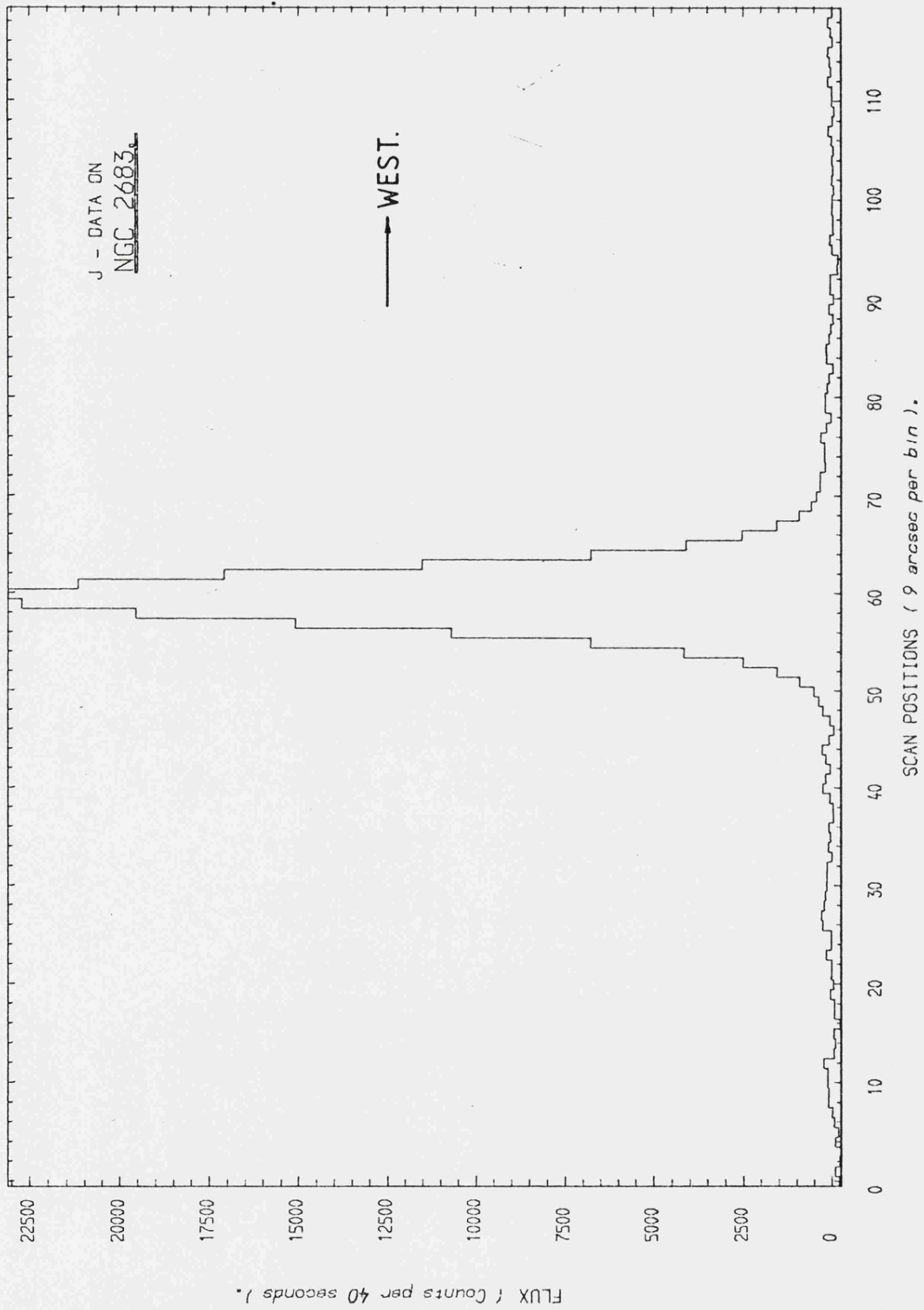
The surface brightness at J of the nucleus of the galaxy is in good agreement with that obtained by Adamson (1983) ( see Table 4.1 ). The K magnitude is a little brighter than the estimate of Adamson. However, the errors on his magnitudes are unknown.

The magnitude of the galaxy nucleus at V could not be determined because no neutral density filters were



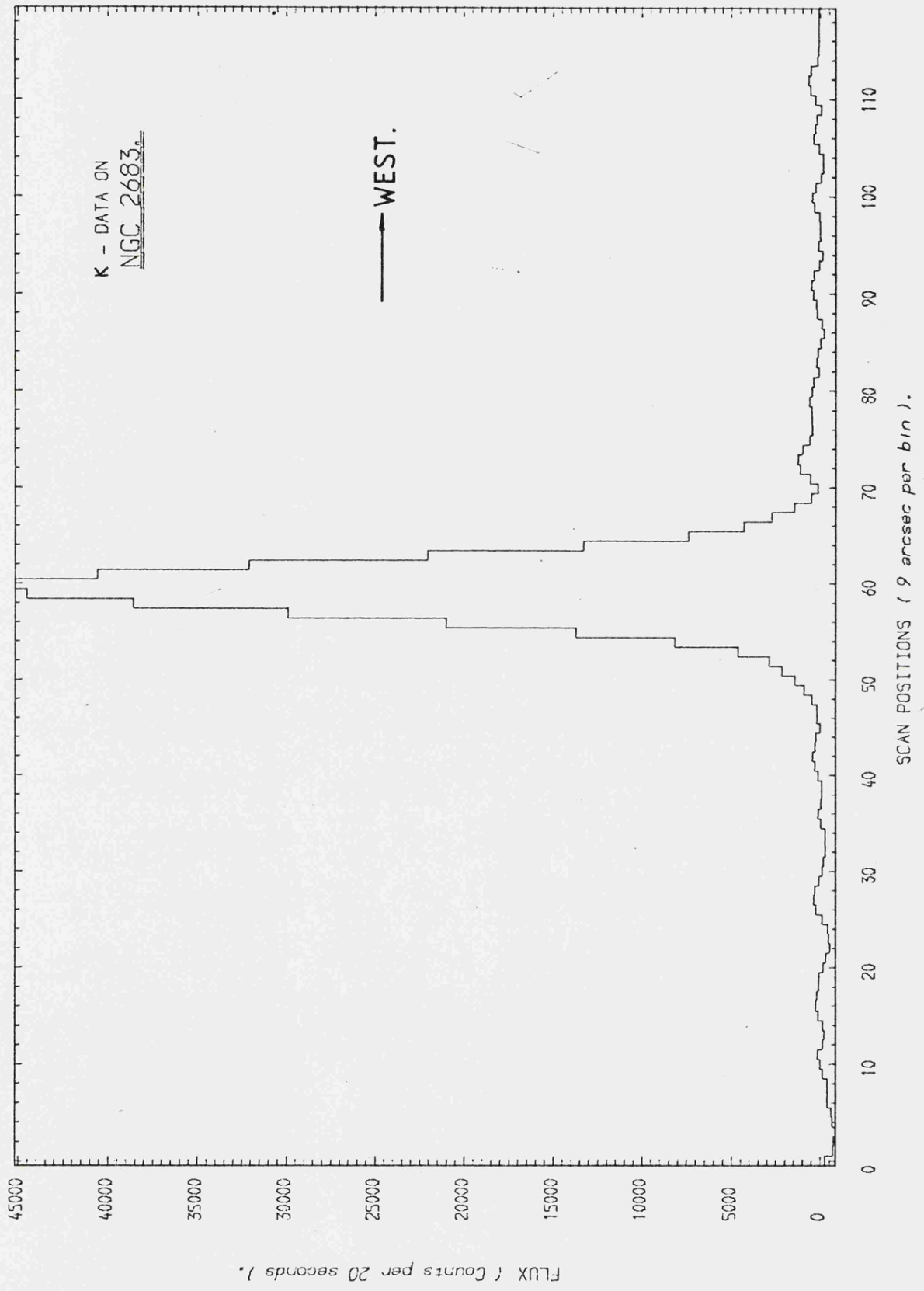
V DATA SCAN.

Figure 4.6



J DATA SCAN.

Figure 4.7



K DATA SCAN.

Figure 4.8

	SURFACE BRIGHTNESS ( Adamson )	SURFACE BRIGHTNESS ( mag.arcsec <sup>-2</sup> )
JOHNSON BAND	( mag.arcsec <sup>-2</sup> )	±0.01
V	17.90	-
J	16.45	16.48
K	15.36	15.12

TABLE 4.1

available on the trip. This meant that the pulse rate from the photomultiplier tube, produced by bright objects, exceeded the maximum pulse rate that the discriminator could handle and so the standard star counts at V were found to be useless. This also meant that the absolute colour of the galaxy nucleus could not be determined although the relative colours were unaffected.

As described earlier, the data was over sampled and so a running average was taken. This is where every bin had the preceding and proceeding elements added to it and the first and last two bins of the data set were then discarded.

The resulting colour plot<sup>2</sup> is shown in Figure 4.9 where the galaxy's nuclear colour has been set to zero since the standard star V count was unobtainable. This plot indicates that the galaxy is, infact, reddening out to a distance,

<sup>2</sup> Note that, because of this running average, only every third point plotted on the colour plot is statistically significant.

perpendicular to the line of sight, of approximately 2.5kpc from the galaxy's nucleus<sup>3</sup>. This reddening is more apparent on the West than the East side. Because the galaxy is at an inclination of approximately 80° to the line of sight ( Mayall and Lindblad (1970) and Simkin (1975) ) the reddening is probably due to internal galactic absorption.

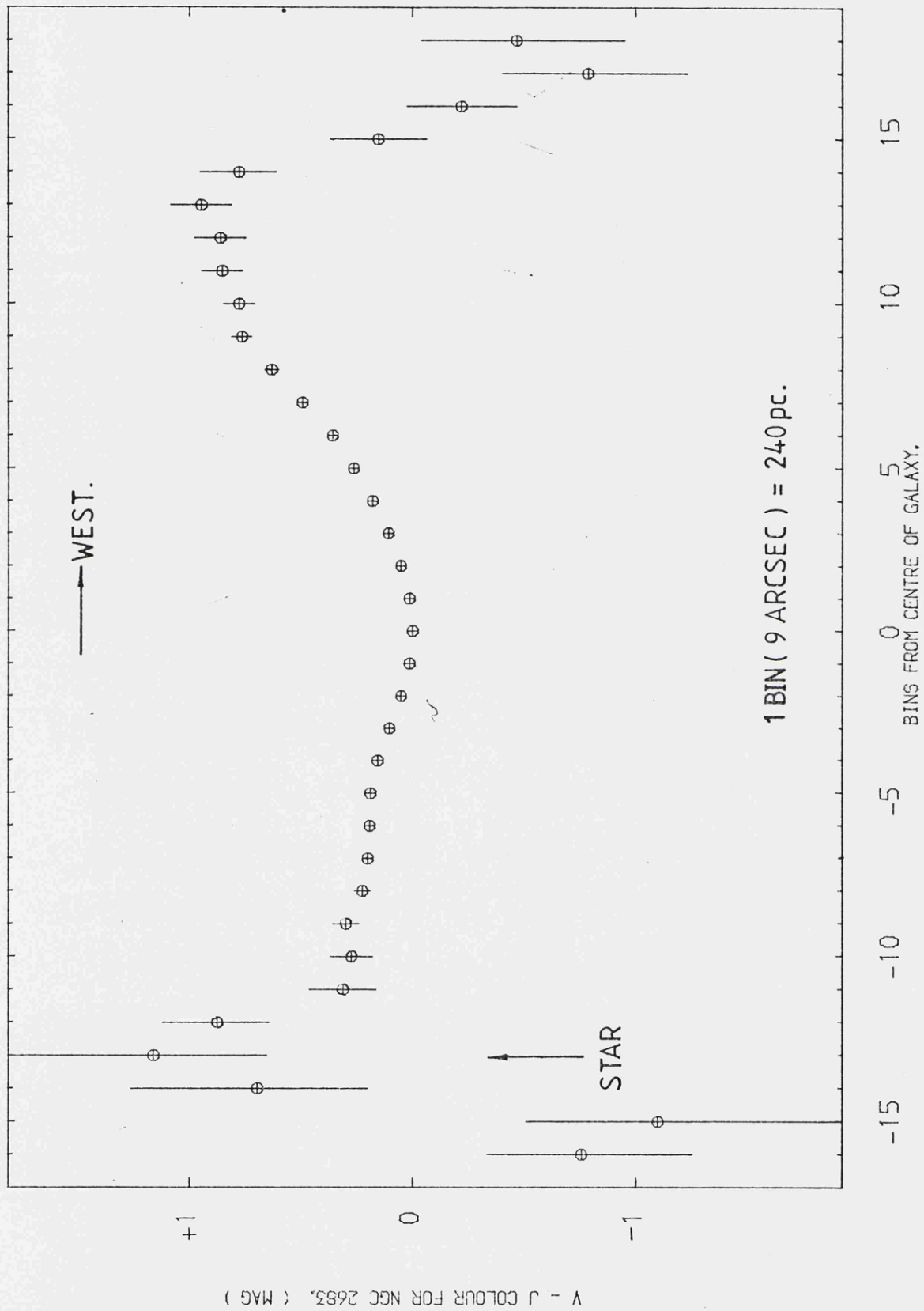
The infrared excess on the West side of the galaxy could either be due to a faint diffuse halo or, alternatively, a nuclear bulge which would have to extend out to approximately 2.5kpc from the nucleus. This would then indicate that the redder edge was the most distant edge, agreeing with Simkin (1967). The nuclear bulge of the galaxy would, most probably, consist of heavy-element-rich stars, such as late-type M giants and population I K giants ( Nassau and Blanco (1958) and Eaton (1982) ). Therefore, if one believes that the spheroidal component extends 2.5kpc out from the nucleus, then there is no evidence to support, or refute, Simkins proposal that a halo exists around NGC 2683.

The red detection at bin position -13 on the colour plot is the faint star to the East of the nucleus on Plate 4.2.

It should be noted that there were possible errors in the background determination which would affect the colours. In the scanning system used both the infrared and the optical channels were chopped by the same mirror. As a result both the infrared and optical channels consisted of two common beams, the object beam and the reference beam. The

---

<sup>3</sup> Using a distance of 5.5Mpc from Simkin (1975). It should be noted that Simkin derived this distance from its recessional velocity and Hubbles expansion law. Therefore, her estimate of the galaxy's distance is in some doubt.



PLOT OF V-J COLOUR vs RADIAL DISTANCE FROM NUCLEUS.

Figure 4.9

reference beam was used to remove any sky drifts from the infrared data and the resulting counts at the two wavelengths were :-

$$J_{tot} = J_{obj} - J_{ref}$$

$$V_{tot} = V_{obj} + V_{ref}$$

where  $J_{obj}, V_{obj}$  are the object beam counts and  $J_{ref}, V_{ref}$  are the reference beam counts for the infrared and optical wavelengths respectively. A source passing through the reference beam would reduce the  $J_{tot}$  counts, whereas the  $V_{tot}$  counts would increase. If this source fell into one of the background determination windows the level calculated would be too high for the V data and too low for the J data. This would give a reddening effect similar to that seen on the colour plot.

The only way to rule this effect out was to check the reference beam position, which was 8 arcminutes west of the object beam, for the whole of the scan. No objects were apparent on the Palomar plates and so the background determination was taken to be correct.

A further point to notice is that the colour plot becomes bluer after 11 arcseconds from the nucleus. Two explanations of this can be found. The first is that the galaxy is not quite edge on and so, beyond 2.5kpc, the blue disc becomes less obscured by the spheroidal component and its own absorption within the disc diminishes with distance from the nucleus. This would require that the disc extends out to approximately 7kpc, corrected for the angle to the line of sight, from the nucleus. This is not unreasonable

since the radius of the galaxy, measured from the optical plate along the major axis, was estimated to be 6.5kpc. The second explanation is that the background determination was in error but, as discussed above, this was regarded as unlikely from examination of the Palomar plates and Figures 4.6 and 4.7.

## REFERENCES

ADAMSON, A., "INFRARED SURFACE BRIGHTNESS DISTRIBUTIONS OF GALAXIES", Ph.D. thesis, Leicester University, 1983.

DE VAUCOULEURS, G., DE VAUCOULEURS, A., and CORWIN, H.G., "SECOND REFERENCE CATALOGUE OF BRIGHT GALAXIES", 1976.

EATON, N., "INFRARED AND OPTICAL STAR COUNTS IN THE PLANE OF THE GALAXY", Ph.D. thesis, Leicester University, 1982.

CHARLES, A.P., CULHANE, J.L., and FABIAN, A.C., Mon. Not. R. astr. Soc., Vol. 178, pp 307-323, 1977.

HASCHICK, A.D., and BURKE, B.F., Ap. J. ( Letters ), Vol. 200, L 137, 1975.

HEGYI, D.J., and GERBER, G.L., Ap. J. ( Letters ), Vol. 218, L 7-11, 1977.

HOHLFELD, R.G., and KRUMM, N., Ap. J., Vol. 244, pp 476-482, 1981.

KRUMM, N., and SALPETER, E.E., Astr. Ap., Vol. 56, pp 465, 1977.

MAIHARA, T., ODA, N., SUGIYAMA, T., and OKUDA, H., Publ. Astron. Soc. Japan, Vol. 30, pp 1, 1978.

MAYALL, N.U., and LINDBLAD, P.O., Astr. Ap., Vol. 8,  
pp 364-374, 1970.

NASSAU, J.J., and BLANCO, V.M., Ap. J., Vol. 128, pp 46, 1958.

SIMKIN, S.M., Astron. J., Vol. 72, pp 1032-1039, 1967.

SIMKIN, S.M., Astron. J., Vol. 80, pp 415-426, 1975.

## **CHAPTER 5**

## CHAPTER 5

### 5.1 INTRODUCTION

The data used in this chapter were obtained in November 1980 on the Anglo Australian Telescope ( AAT ) by Dr.M.J.Ward, Dr.D.J.Axon and Dr.R.F.Jameson.

This was the first observing run with the Infrared Photometer's new software system at the AAT and certain difficulties arose in the later analysis of the data which will be discussed at the appropriate time during this chapter.

NGC 613, 1097, 1365, and 1808, four Sersic-Pastoriza galaxies, were chosen because they possess morphologically peculiar nuclei. Designated as 'hot-spots', by Morgan (1958), these regions were thought, by Tovmassian (1966), to be due to active processes causing division of the nucleus into daughter nuclei. Burbidge and Burbidge (1960), Burbidge and Burbidge (1968), and Osmer et al (1974), proposed that these regions were, in fact, HII regions with dust lanes extending into the nucleus.

Osmer et al showed that the corrected H $\beta$  luminosities, for NGC 613, 1097, and 1365, are similar to those of

Seyfert galaxies. They proposed that hot stars are the most plausible source of ionizing radiation which are strongly reddened, in the visible, by interstellar absorption. However, the  $H\beta$  luminosities, after correction for interstellar absorption, were a factor of 10 to 100 times more luminous than that from a typical giant HII region. This led Osmer et al to conclude that the rapid star formation, proceeding in the HII complexes, is only transitory.

Maps were generated from the AAT data and, in the cases of NGC 1097 and NGC 1365, greyscale plots are shown from a later trip to the AAT. Unfortunately, the data for the greyscale plots were obtained rather late and so no detailed analysis has been conducted on them.

J-H versus H-K plots for each of the galaxies were attempted in an effort to determine the emission processes in the nuclear and perinuclear regions. However, there were some doubts about the results produced which will be discussed in section 5.3 (iii). Colours are calculated, from the map and spot photometry data, for various aperture sizes for the nuclei of these galaxies. The maps of the galaxies were also tested to see if the isophotes of their nuclei conform to de Vaucouleurs and/or the exponential Disc law.

This chapter is subdivided into into the following sections :-

5.1] INTRODUCTION

5.2] THE OBSERVATIONS

5.3] DATA PROCESSING TECHNIQUES

5.4] ANALYSIS OF THE DATA

## 5.5] DISCUSSION AND CONCLUSIONS

### 5.2 THE OBSERVATIONS

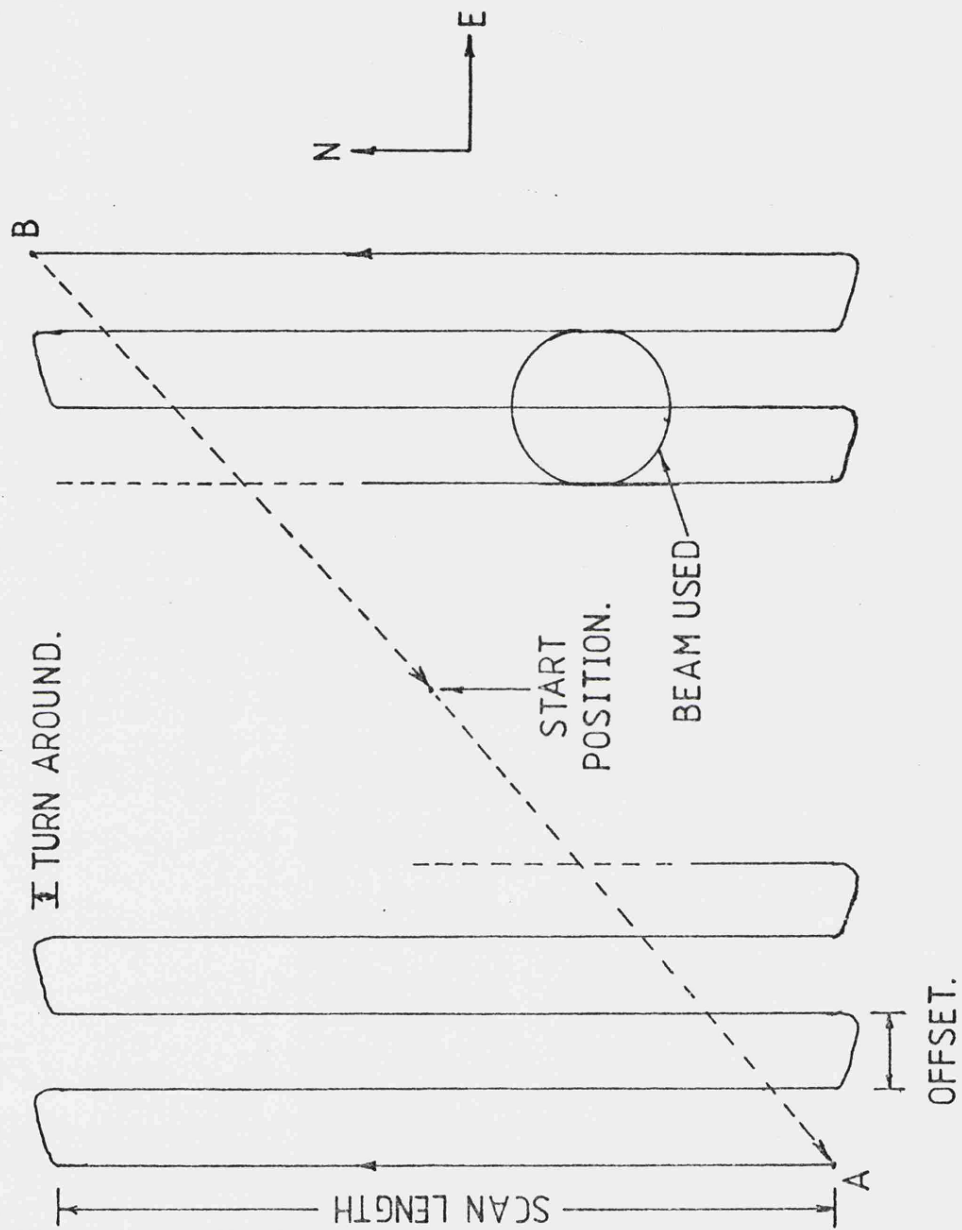
Most infrared observations are conducted in, what is known as, "AC mode". This is where a chopping mirror is used to switch the section of sky the detector "sees" from object to background very rapidly. The chopping frequency is made fast enough so that any sky variations are insignificant over the chopping/sampling period. The main drawback to this system is that if a source moves into the infrared reference beam the object counts will be significantly reduced, since the resultant count is the difference between the two beam position counts ( see Chapter 4, section 4.5 ).

When looking at diffuse objects, such as galaxies, these reference beam contaminations would make the analysis of the data very awkward. A solution to this problem is to switch the chopping mirror off and use the telescope in "DC mode".

The telescope was centred on the nucleus of the chosen galaxy. On starting the scan the telescope went through three phases ( shown in Figure 5.1 ):-

- 1] Offset to the corner of the scanning box (position A).

- 2] Raster scans across the object finishing at the corner diagonally opposite position A (position B).



TELESCOPE SCANNING METHOD.

Figure 5.1

3] Returns to the start position ( ie the nucleus of the galaxy ).

The data collated for each scan were stored on a magnetic tape in IBM 8 bit ( byte ), 16 bit ( half-word ), 32 bit ( full-word ) integer, and 32 bit floating point formats. This tape was eventually read, via a lengthy Fortran programme, onto a Control Data Corporation ( CDC ) CYBER 73 mainframe computer. Each scan began with a header followed by five columns of information, the first being the cycle number and then four lots of data ( an example is shown in Figure 5.2 ).

An attempt to reduce the sky drifts on the data was to scan the objects rapidly. However, this was not rapid enough and all the scans exhibit drifts of which the poorest was the Johnson H band for NGC 1365 ( see Figure 5.4 ).

The new AAT system has gone one step further and scans the object so rapidly that the background counts remain constant for the whole picture. Repeated scans are added into the first, increasing the signal to noise ratio with each scan, and what emerges is a drift free picture ( see Plates 5.2 and 5.3 ).

### 5.3 DATA PROCESSING TECHNIQUES

#### i) Background removal

As can be seen from Figure 5.3 to 5.5 ( NGC 1365 only ), the background drifts were very significant for some of the

Run	Object	UT	RA	DEC	Airmass	Filter	Magn	Mag Const	Points	Ext Coeff	Ext Time	Reset Time	Efficiency	Integ'n Time	B/Switch Cycles	B/Switch Wait
1	NGC 1097	13 50 13	02 45.9	-30 22	10.3	K	2.200	0.000	4	0.000	0.000	94%	5580.2	0.80	5569.4	0.05
2	MODE 1	APERTURE 06											5585.6		5577.6	
3	1000	EXTENDED											5602.1		5582.7	
4	196	196											5666.3		5633.5	
5													5656.3		5653.1	
6													5706.1		5749.2	
226													5916.8		6033.3	
													5791.6		5881.3	
													5491.5		5515.8	
													5505.5		5502.6	

FORMAT OF RECOVERED AAT DATA.

Figure 5.2

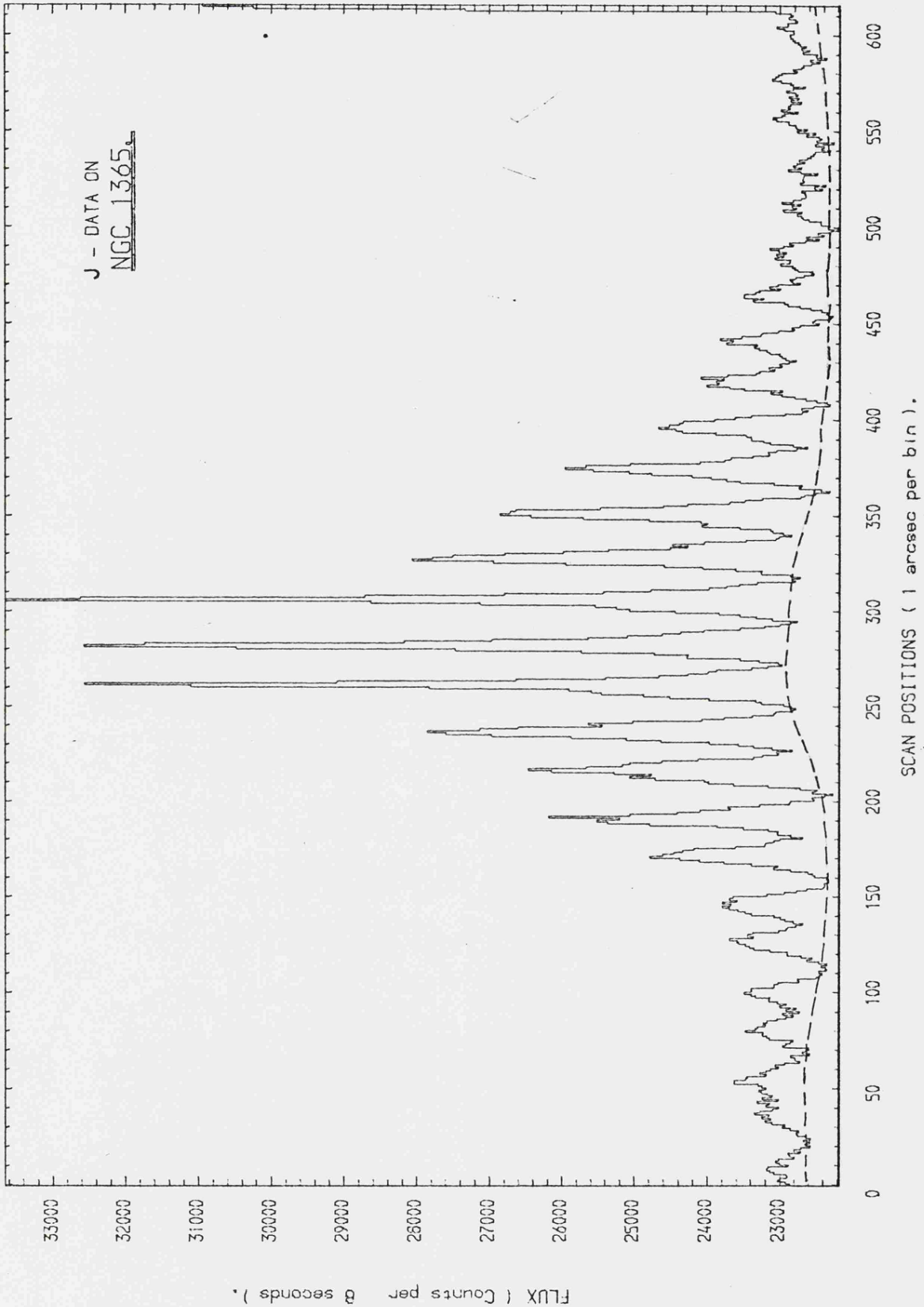
scans. For the worst case the drift was approximately 10% of the peak signal. The method employed for removing these drifts was to intercompare the raw data for the three wavelengths since a source which is obvious at the Johnson K band must also be evident at the Johnson H and J bands ( with the possible exception of hot dust ). This helped in distinguishing between a real detection and a background drift. Curves were then drawn, by eye, along what were thought to be the background levels for each of the J, H, and K data sets ( dotted curve ). A digitiser was then used to transfer these curves onto files on the CYBER. These background-data files were used to remove the sky drifts from the relevant raw data leaving almost drift free scans.

ii) Picture construction routine

The next step was to construct a "picture" from the drift free data. However, the scan lengths in Declination ( DEC ) were known only approximately. Also, the turn around time of the telescope and the delay between the start of integration and the start of the raster scan, which varied for each scan, were all unknown.

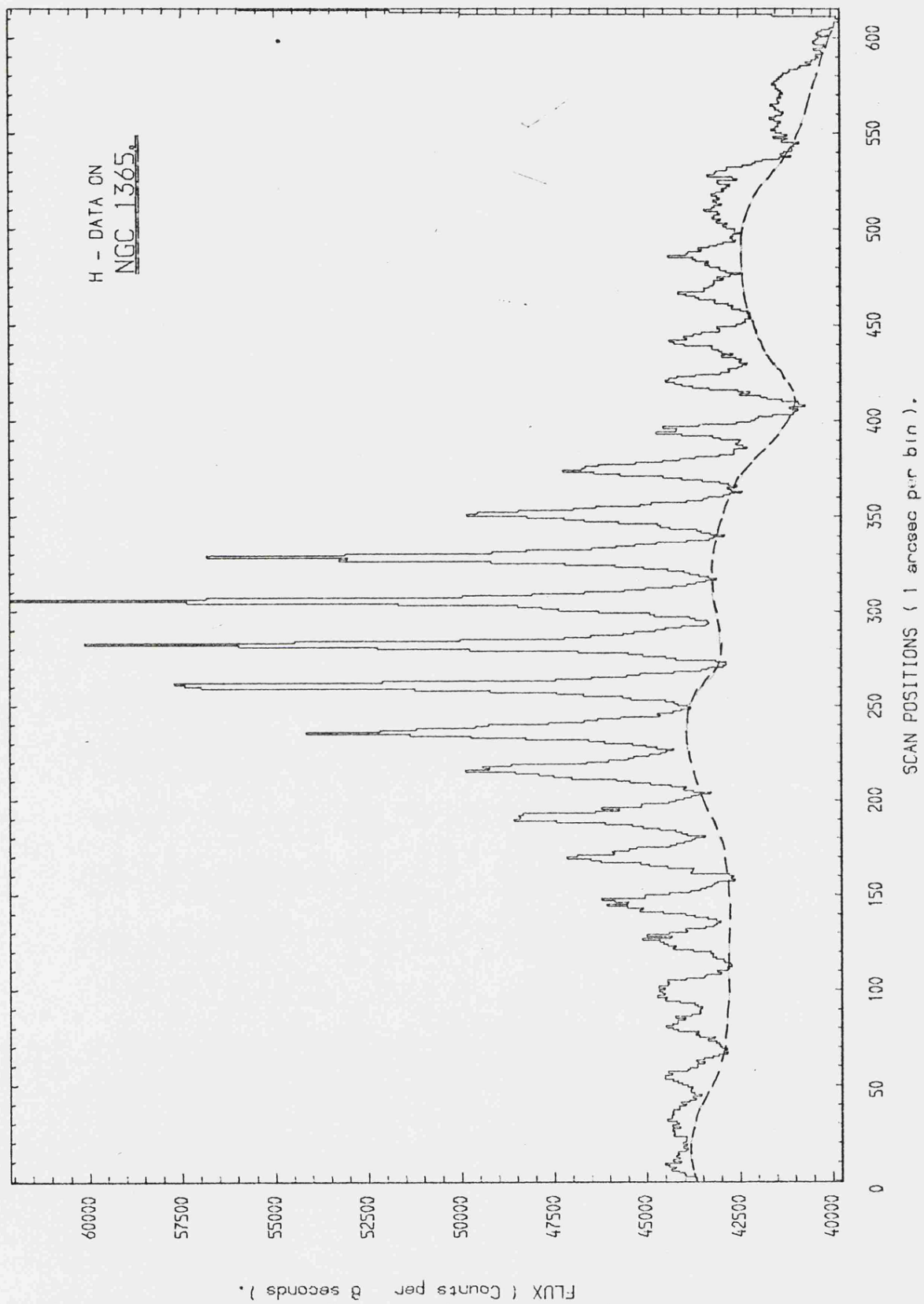
This proved to be very troublesome at first but eventually a routine was written which could sort these previously unintelligible data sets into sensible pictures. To construct a picture from a raw data set a Fortran programme was written which would execute the following :-

1] Find the maximum reading in the data set ( in all cases this was the nucleus ).



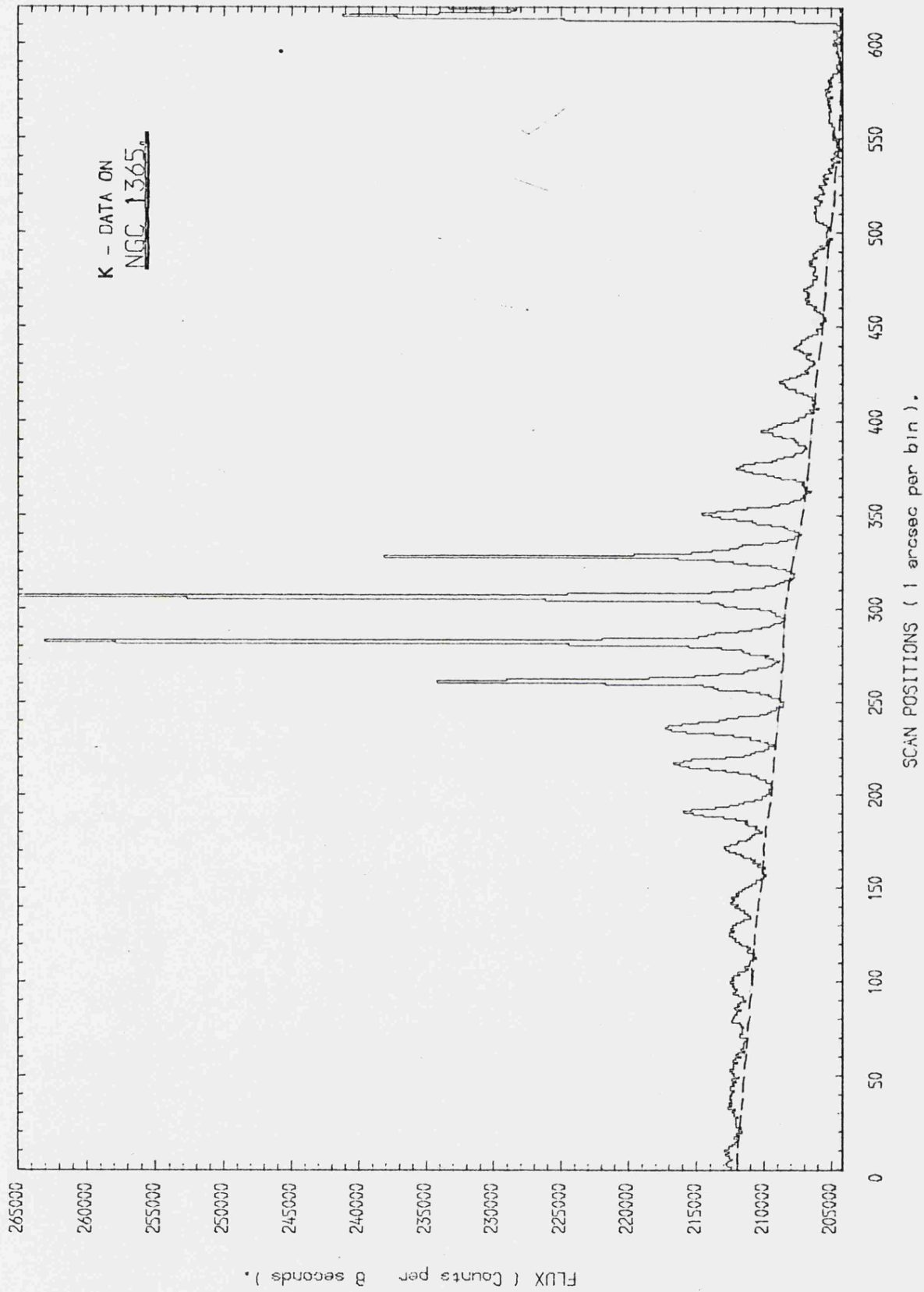
RAW J DATA FROM SCAN OF NGC 1365.

Figure 5.3



RAW H DATA FROM SCAN OF NGC 1365.

Figure 5.4



RAW K DATA FROM SCAN OF NGC 1365.

Figure 5.5

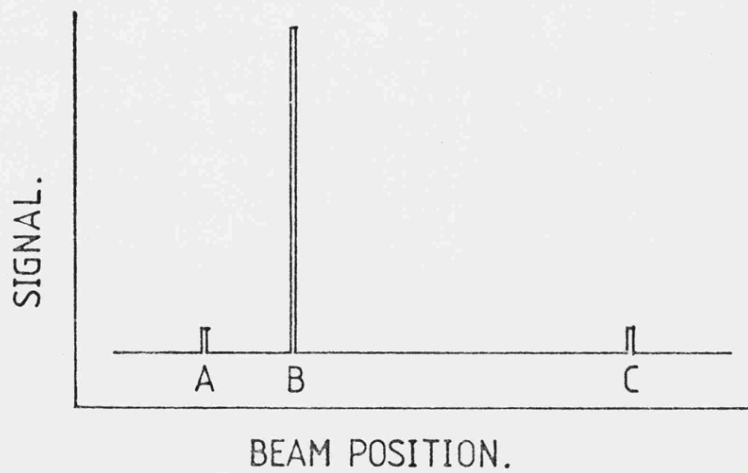
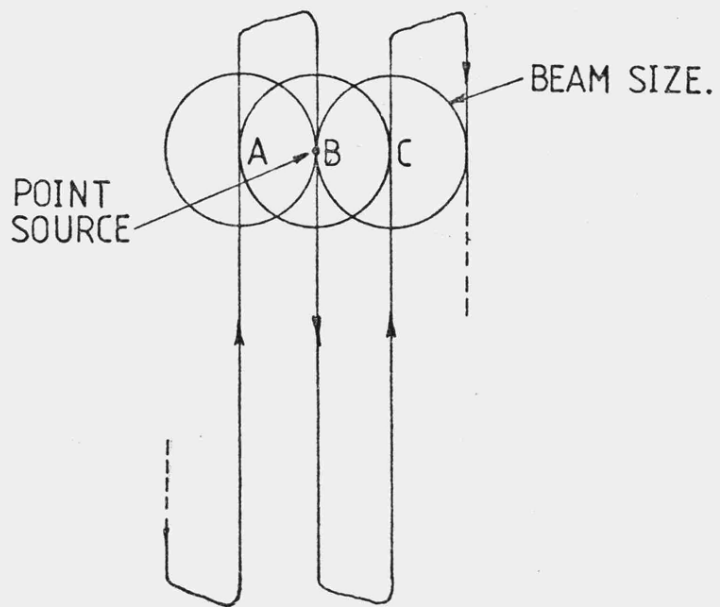
2] Collect the coordinates of the nearest subsidiary maximum coordinates and the approximate scan, as chosen by the observer. Half the distance between the two maxima gave a scan start position, since the turn around time of the telescope should be less than one bin in length.

3] Using the present scan length, the computer stepped back through the data, a scan length at a time, until the start of the whole data set was found ( ie as close to the first bin in the data set as possible ).

4] From the scan start position scan lengths of data were transferred to a two dimensional array with every other scan reversed. This was because the Raster scanning mode was used ( see Figure 5.1 ).

5] Because the data was over sampled by a factor of 2 a point source would appear in a maximum of three and a minimum of two scans ( illustrated in Figure 5.6 ). This helped in arriving at the best picture ( ie the picture with the minimum amount of structure ).

The method chosen for finding the best picture was to sum up all the absolute values of the gradients ACROSS the scan lines. For the point source example there would be a minimum in the gradient summation when the three detections coincided. A contour plot of NGC 1097 with a wrong scan length is shown in Figure 5.7 to illustrate the results obtained prior to the use of this minimizing routine. If



AN EXAMPLE OF A SCAN OF A POINT SOURCE.

Figure 5.6

the sum of the absolute gradients was less for the present picture than the previously saved picture, the latter would be replaced with the former.

6] The scan length was incremented from -2 to +2 arcseconds about the approximate value in steps of 0.1 arcseconds. Routines 3] to 5] were then executed again for each new scan length.

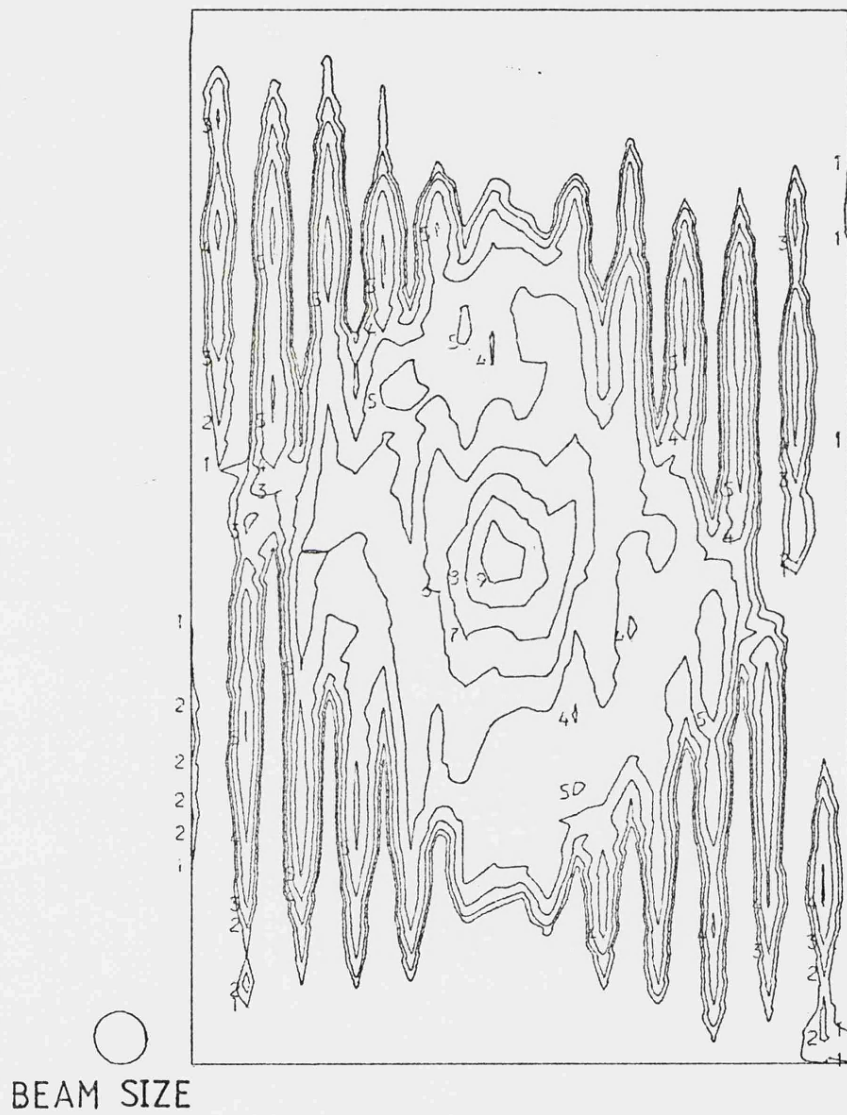
7] On completing all the interval steps about the approximate scan length, the programme would then plot the picture with the minimum gradient summation.

The above technique gave a much improved contour plot which was free from oscillations, unlike Figure 5.7. Figures 5.8, 5.9, 5.10, 5.16, 5.17, 5.18, 5.23, 5.24, 5.25, 5.29, 5.30 and 5.31 are the final versions for the four galaxies. Table 5.1 shows the approximate scan lengths as compared with the scan lengths obtained by the above routine.

### iii) Radial power law routine

To test power laws, such as de Vaucouleurs  $R^{1/4}$  law, a routine was derived to sum up the data points around concentric ellipses, of which the eccentricity and position angle ( PA ) had to be provided by the user.

The routine took the maximum in the two dimensional data set as the centre of the concentric ellipses. Then, taking a datum at the map coordinate [ x,y ], it calculated the



CONTOUR PLOT OF NGC 1097 WITH WRONG SCAN LENGTH.

Figure 5.7

---

GALAXY	JOHNSON	SCAN LENGTH	SCAN LENGTH
NGC NO.	BAND.	APPROXIMATE.	FINAL.
		( arcsec )	( arcsec )

---

613	J	30	30.71
	H	30	30.72
	K	30	30.68
1097	J	40	40.93
	H	40	40.99
	K	40	40.80
1365	J	40	39.55
	H	40	39.73
	K	40	39.55
1808	J	30	30.71
	H	30	30.75
	K	30	30.80

---

TABLE 5.1

semi-major axis,  $a$ , of the ellipse<sup>1</sup> to which the datum was associated. The semi-major axis for each datum was rounded to the nearest whole arcsecond and was then used in binning up the data. The logarithm of the flux counts could then be plotted as any function of the semi-major axis.

iv) Colour map construction routine

The colour maps produced were either J-H or H-K. The wavelength common to both these colour maps was the Johnson H band. A comparison between the H picture and the colour

---

<sup>1</sup> Derivation of this is in Appendix C

plots was vital so that the colour plot could easily be assessed. So, the H picture was kept fixed while either the J or K pictures were shifted in the X and Y axis to find the "best" colour picture. This was to allow easy conversion to the colour-colour plots in the later analysis of these galaxies.

Several methods were used to find the "best" contour picture and all the routines returned different answers which were generally reasonable for one colour but not for the other. This continual inconsistency in the methods meant none of the colour plots could be believed. As a result, no information was drawn from the data, via this method, on the emission processes which are occurring in the nuclear and perinuclear regions.

The methods used in attempting to match up the two wavelength pictures were as follows :-

METHOD 1 : All the data points, in the picture being compared with the H band picture, were scaled such that the maxima, at the two wavelengths, were the same.

The next step was to move this picture until the Volume difference<sup>2</sup> between the two pictures reached a minimum. At this point, it was assumed that the best fit had been found and the colour map was then generated.

METHOD 2 : This method took the ratio of the counts, for a given pixel, subtracted one and then added the positive value of this ratio to the total count. This was repeated

---

<sup>2</sup> Volume difference is, for example,  $\sum |C_J - C_H|$  where  $C_J$  and  $C_H$  are the pixel counts at J and H.

for all the array, providing the counts were one standard deviation above the background, and the results were added in to the total count. An average of the total count was then obtained. The colour picture with the smallest average was then assumed to be the best fit.

Variations on the above methods were also applied ( eg confining the above routines to the 25 elements centred on the maximum ) and still results were returned which could not be believed. These problems were a result of the pictures being misaligned and, on shifting a picture fractions of a bin, an inherent smearing of the shifted data resulted. These problems presumably confused the minimizing routine which returned poor results.

It was, therefore, decided that these methods were not going to yield sensible results within a reasonable length of time and so colours could only be obtained from averaging several pixels.

#### 5.4 ANALYSIS OF THE DATA

The method used for determining the inclination and PA of the galaxies from the contour plots was to assume that the nuclear bulge of a galaxy is circularly symmetric, if viewed at an inclination to the line of sight of zero degrees. Then the PA and the inclination,  $i$ , can be ascertained from the eccentricity of the bulge's isophotes. However, if the inclination exceeds a maximum<sup>3</sup> of

---

<sup>3</sup> derived in APPENDIX D.

$i_{\max} = \text{Tan}^{-1} ( a/b - b/a )$ , where  $a$  and  $b$  are the semi-major and semi-minor axes of the bulge respectively, the estimate for the inclination would be in error. Moreover, if the nuclear bulge was elliptical, or irregular viewed at  $i = 0^\circ$ , the value obtained for the PA would also be in error.

Table 5.2 shows how the estimates derived from the above method compare with other people's appraisals.

GALAXY	POSITION	INCLINATION	REFERENCE
NGC No.	ANGLE	( degrees )	
	( degrees )		
613	111	36	BLACKMAN (1981)
	-	~54	WRIGHT (1968)
	-	37	DE VAUCOULEURS et al (1976)
	110	36	THIS THESIS
1097	115	48	BLACKMAN*
	136	49.5	BURBIDGE AND BURBIDGE (1960)
	-	44.5	DE VAUCOULEURS*
	103	~47	THIS THESIS
1365	57	40	BLACKMAN*
	-	46	WRIGHT*
	-	55	DE VAUCOULEURS*
	44.5	66	BURBIDGE*
	47	45	THIS THESIS
1808	~142	66.5	BURBIDGE AND BURBIDGE (1968)
	-	55	DE VAUCOULEURS*
	110	41	THIS THESIS

\* - REFER TO PREVIOUS REFERENCE FOR YEAR OF PUBLICATION.

TABLE 5.2

i) NGC 613

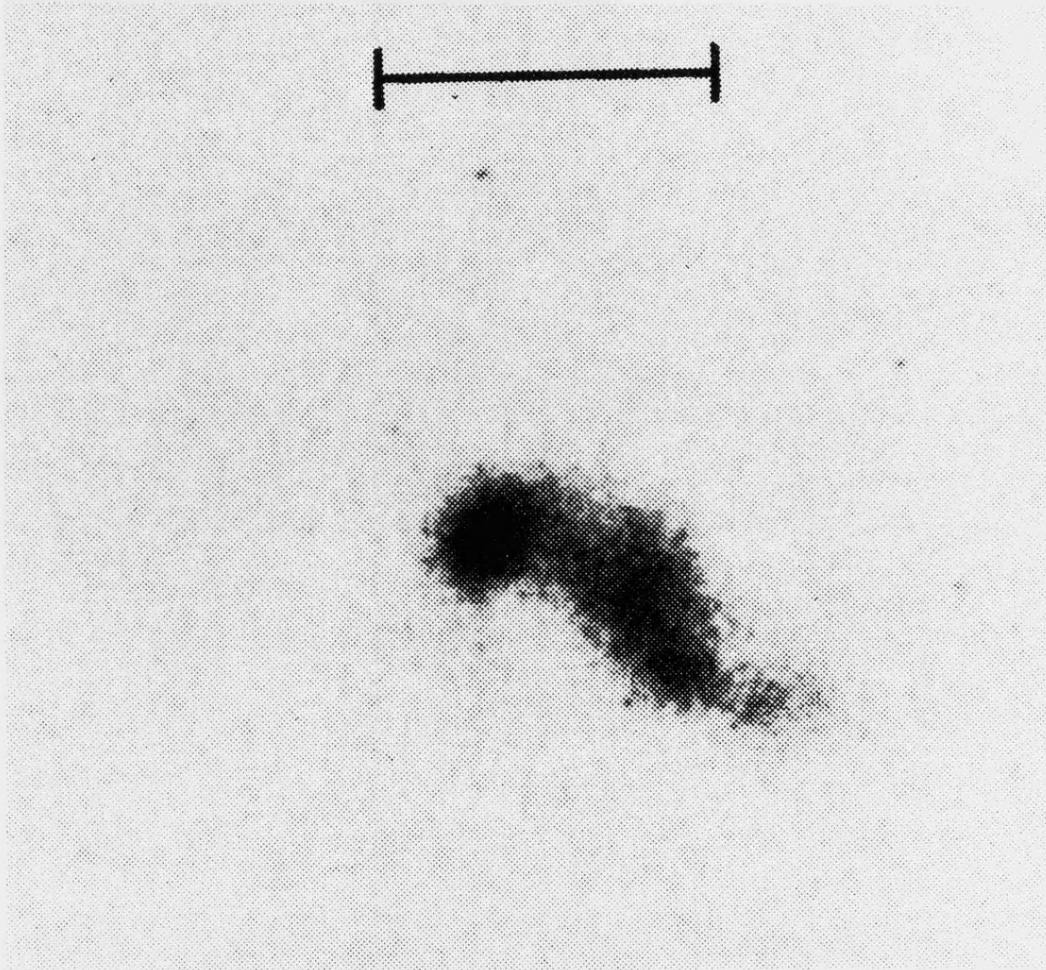
This galaxy, which is at a distance<sup>4</sup> of 20Mpc and has a morphological classification<sup>5</sup> of SB(rs)bc, has been studied by only a few people ( see Osmer et al (1974), Prabhu (1980) and Blackman (1981) ). The nucleus appears to be asymmetric in the optical ( see Plate 5.1 ) with two prominent hot-spots, one 4.3 arcseconds to the north-west and the other 2.1 arcseconds to the south-east of the faint nucleus. However, at J, H and K the asymmetry becomes less apparent ( see Figures 5.8, 5.9 and 5.10 ).

Cuts, which went through these hot-spots and the nucleus, were performed on all the data sets for the three wavelengths. The cuts through the K data ( Figures 5.11 and 5.12 ) illustrate how these hot-spots have become "attached" to the nucleus. This structure, evident in Figure 5.11, appears to be a bar extending out to approximately 0.6kpc from the nucleus, agreeing with the findings of Sersic and Pastroiza (1965, 1967) that "...there is a relationship between abnormal nuclear structures and the existence of a bar". A curve was fitted by eye to, what was thought, the underlying galaxy's profile. At 4.3 arcseconds north-west of the nucleus, the colours were determined for the observed counts and the underlying galaxy profile. These colours are shown in Table

---

<sup>4</sup> The distances of the galaxies were obtained by assuming a Hubble constant of 75 km/s/Mpc and using radial velocities from de Vaucouleurs et al (1976) unless otherwise stated.

<sup>5</sup> All morphological classifications were obtained from Sersic and Pastoriza (1965).

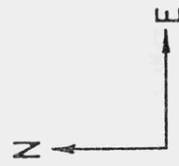
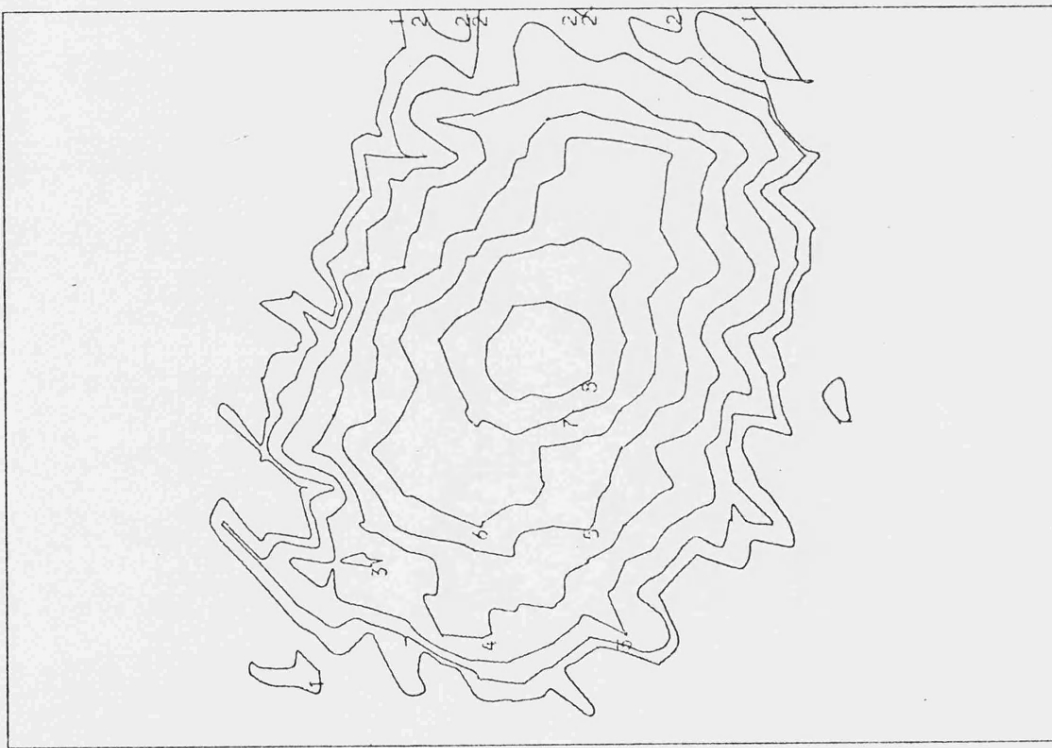


SCALE : 0.21 ARCSECONDS PER MILLIMETRE

Plate 5.1

5.21

LOWEST CONTOUR = 22.13 mag / arcsec<sup>2</sup>  
PEAK READING = 18.21 mag / arcsec<sup>2</sup>



BEAM SIZE.

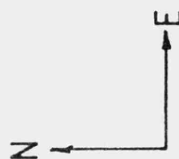
SCALE : 0.21 ARCSECONDS PER MILLIMETRE

J CONTOUR PLOT OF NGC 613.

Figure 5.8

LOWEST CONTOUR = 21.73 mag/arcsec<sup>2</sup>

PEAK READING = 17.33 mag/arcsec<sup>2</sup>



BEAM SIZE.

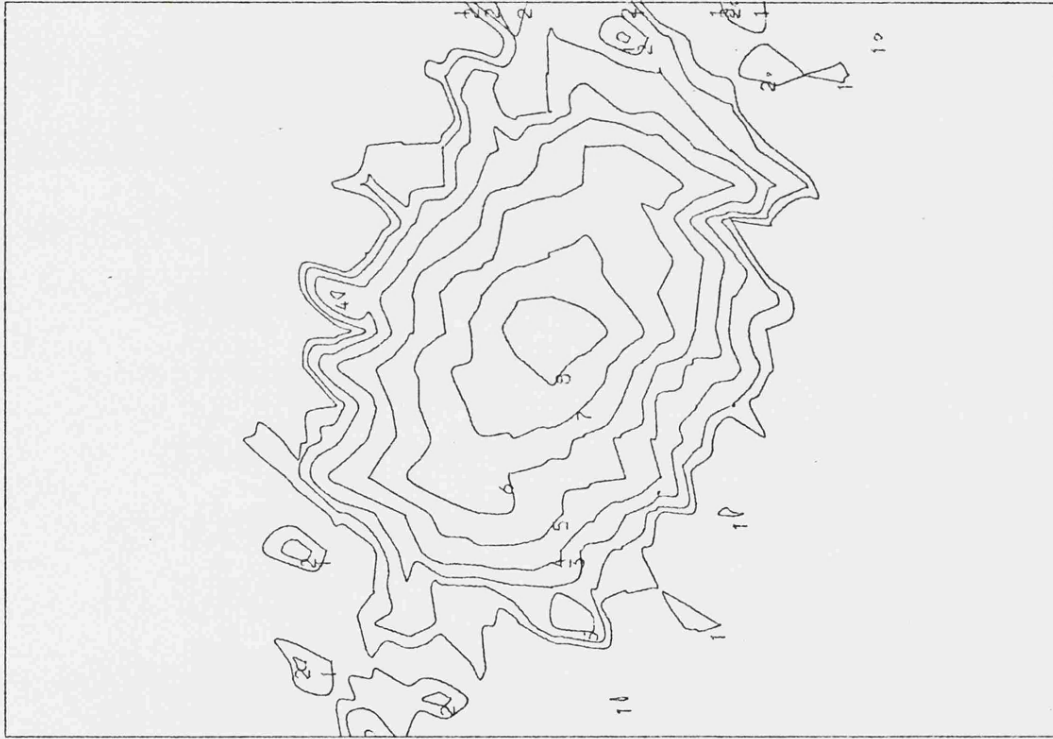
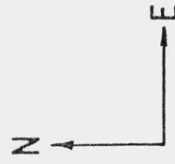
SCALE : 0.21 ARCSECONDS PER MILLIMETRE

H CONTOUR PLOT OF NGC 613.

Figure 5.9

LOWEST CONTOUR = 20.9 mag / arcsec<sup>2</sup>

PEAK READING = 16.94 mag / arcsec<sup>2</sup>

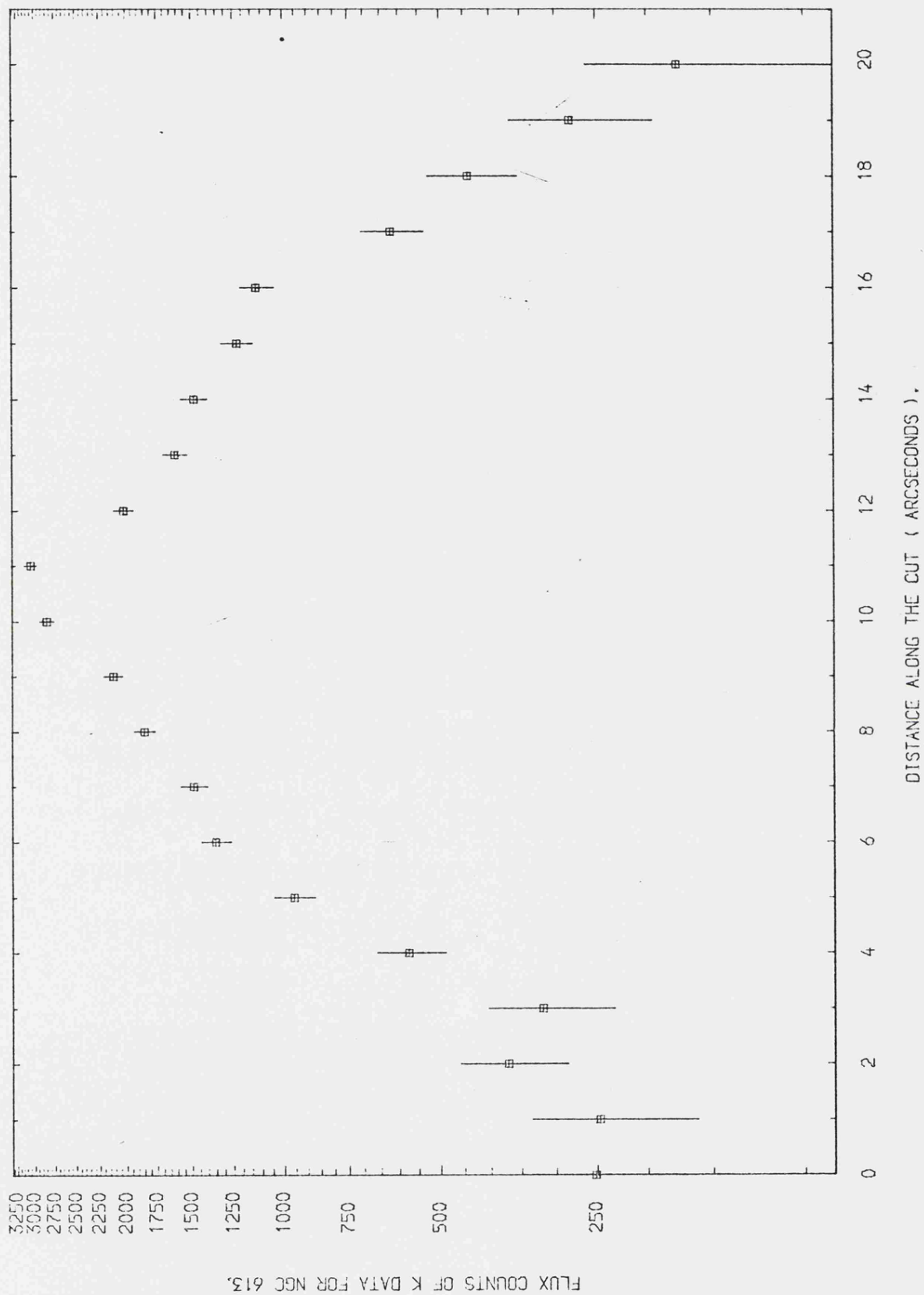


BEAM SIZE.

SCALE : 0.21 ARCSECONDS PER MILLIMETRE

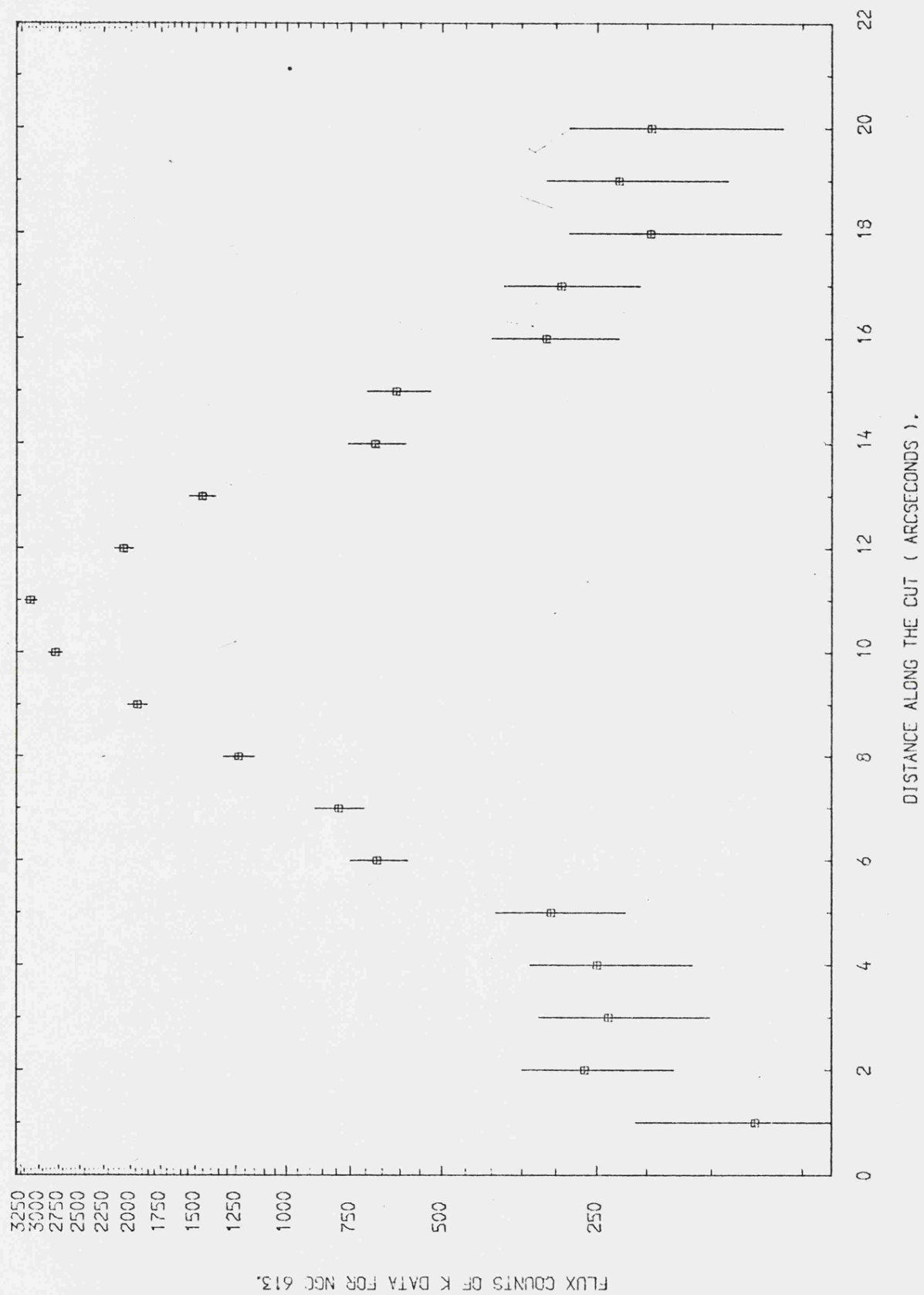
K CONTOUR PLOT OF NGC 613.

Figure 5.10



A CUT THROUGH THE NUCLEUS AND HOT-SPOTS FOR THE K DATA.

Figure 5.11



A CUT PERPENDICULAR TO THE NUCLEUS-HOT-SPOT AXIS.

Figure 5.12

5.3 and are plotted on Figure 5.22<sup>6</sup>. The vector, joining these two points tentatively suggests that the excess counts are probably due to HII regions and hot dust.

The inclination and PA, determined from the maps, agree very well with those obtained by other people and was, therefore, used in obtaining the annular radial summation profiles.

The annular radial summation plots of the J, H and K data are shown in Figure 5.13, 5.14 and 5.15. The H and K plots seem to indicate a discontinuity at a radial distance of 10 arcseconds (  $\approx 1\text{kpc}$  ) although it is less evident at J. This distance compares very favourably with the discontinuity in the radial velocity curve obtained by Blackman (1981). Within this radius the nuclear mass was determined by Blackman to be  $6 \times 10^9 M_{\odot}$  and is also rotating like a solid body. There appear to be no arms extending beyond this point within the boundaries of the contour plots.

The next feature to notice, on Figures 5.13 to 5.15, is that the central counts do not exhibit a beam effect<sup>7</sup>. For a rough determination of the possible cause of the excess counts in the nucleus an attempt was made at extrapolating

---

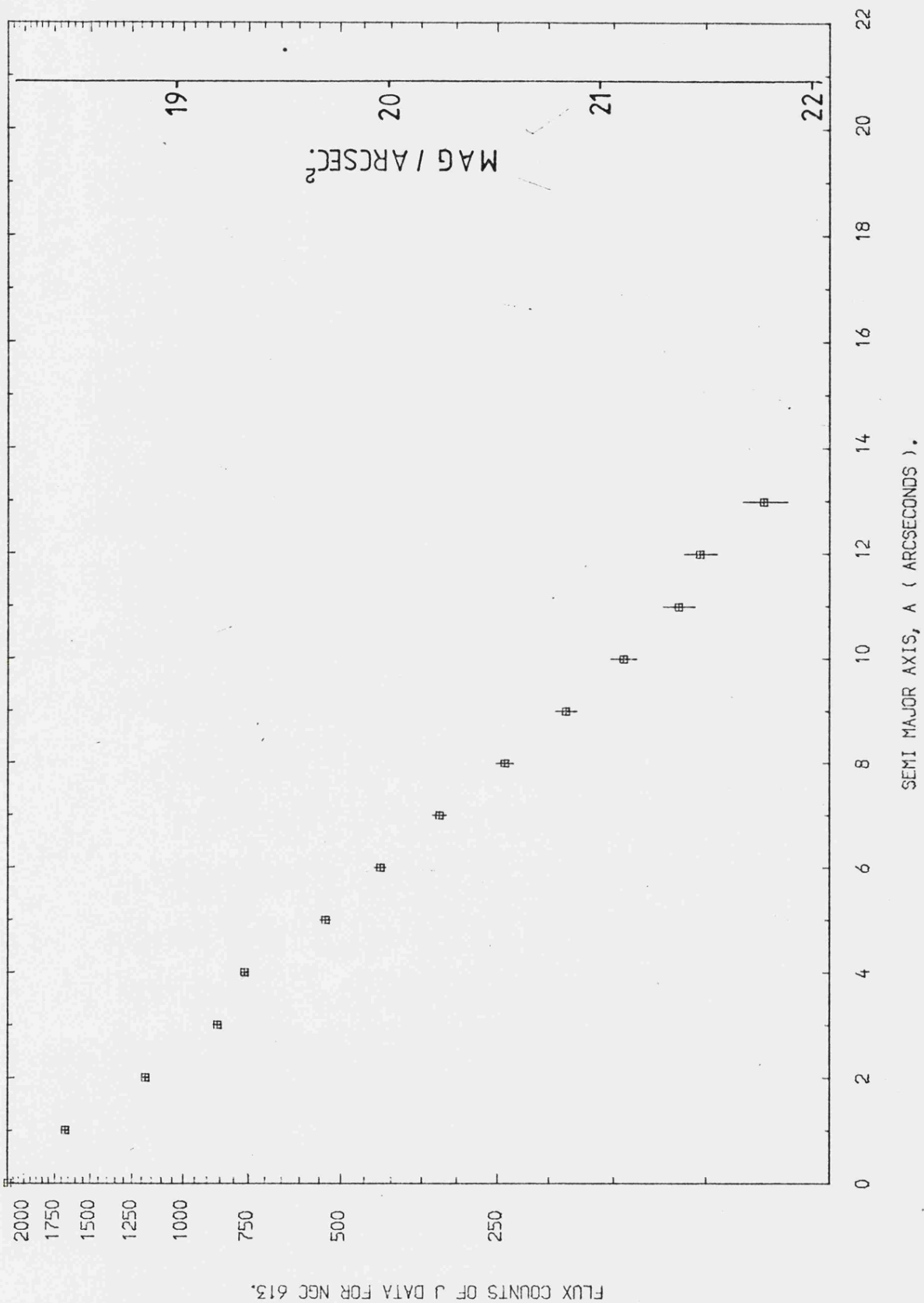
<sup>6</sup> Figure 5.22 is a J-H vs H-K graph. The dashed ellipse is the region where normal galactic nuclei are found when the light arises predominantly in red giants. It also shows the loci of late type giants and dwarfs, and the vector displacements generated with the addition of reddening, of emission from 1000K dust, of free-free bremsstrahlung radiation and a blue stellar contribution from AOY stars ( reproduced from Telesco and Gatley (1984) ). The error bars are for the extrapolated colours only. The errors on the observed colours are at least a factor of 2 better than these.

<sup>7</sup> A finite measuring beam can only give an average rather than an ideal peak count near the nucleus. This is the beam effect.

the annular radial summation profiles into the nucleus. However, the colours calculated were not significantly different from the observed colours of the nucleus. This may be because the profiles are perturbed more than was thought by emission from, for example, hot dust within 10 arcseconds of the nucleus.

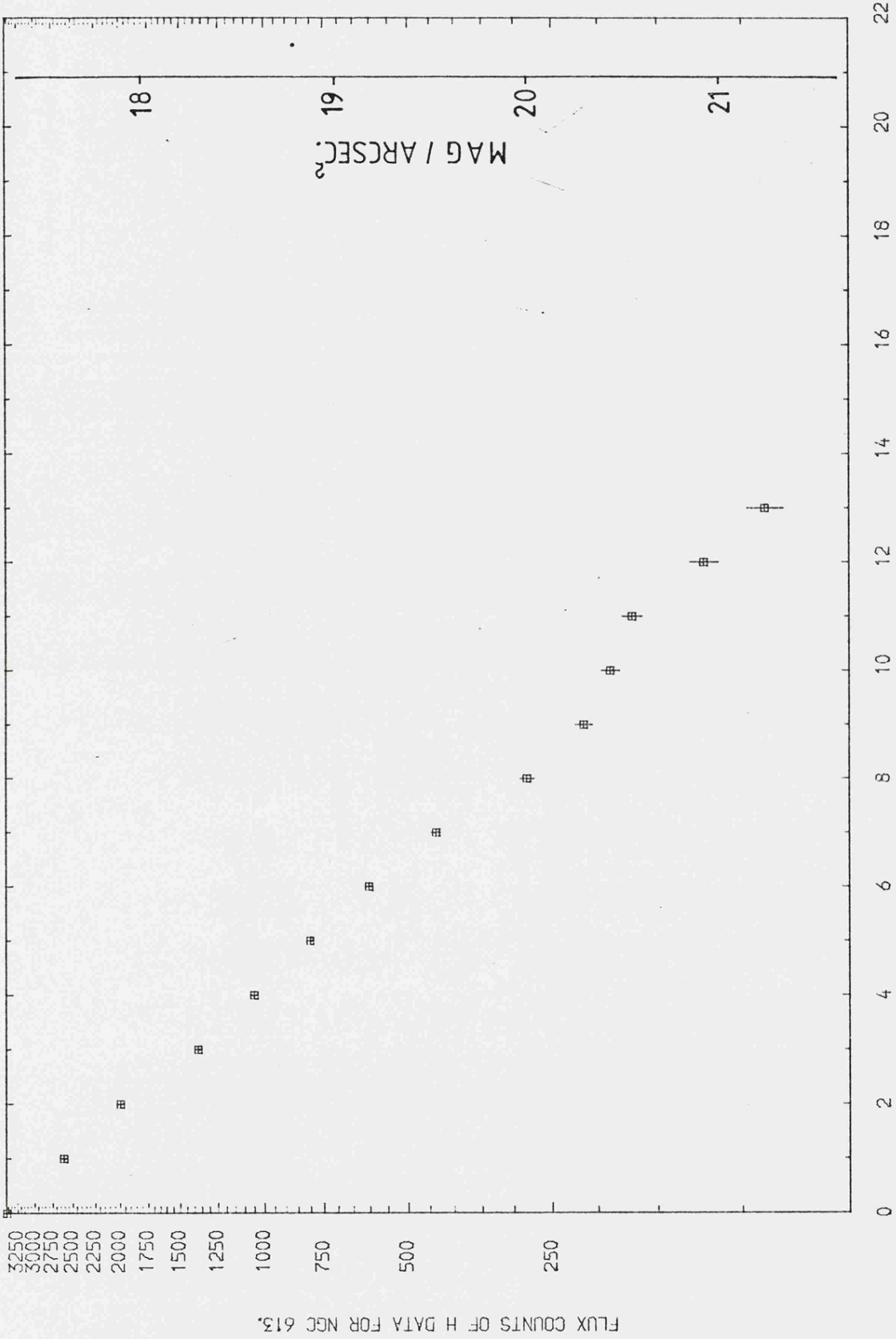
In the visible ( 4000 - 4600 Å ), Prabhu (1980) conducted a similar technique to the annular radial summations above, with the exception that he plotted the logarithm of the intensity versus the effective radius,  $(A/\pi)^{1/2}$ , where A is the area for a given intensity level. Because his data only extended out to 10 arcseconds he did not observe a discontinuity in the profile but he did detect a feature at approximately 2 arcseconds from the nucleus. The absence of this feature on our profile plots can be explained by young blue stars. The elliptical component, or bulge, of the nucleus, which is the source of de Vaucouleurs law, consists mainly of late-type stars ( see Adamson (1984) ) which were probably formed at one epoch in the early life of the galaxy. The transient star formation, thought to be in operation, has perturbed Prabhu's profile from the expected profile since a low number of young blue stars will contribute a large fraction to the optical light and yet very little to the infrared.

The annular radial summation profiles, in Figure 5.13 to 5.15, seem to show that the exponential disc component is beginning to dominate at the edge of the picture. However, the data points beyond 10 arcseconds are not sufficient to be absolutely sure of the gradient of the outer exponential disc law. Ideally, the scan of the central region should



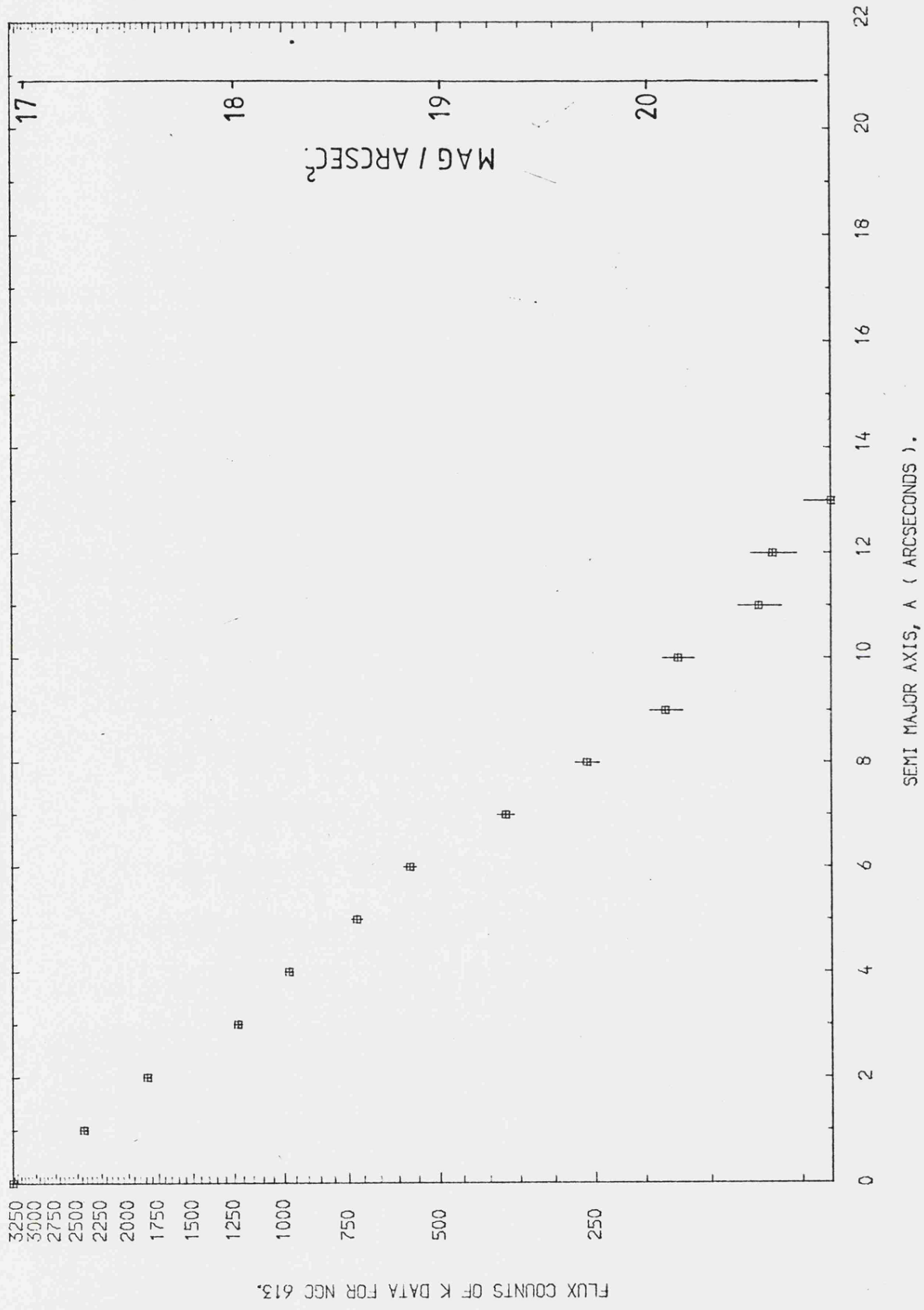
ANNULAR RADIAL SUMMATION PLOT FOR THE J DATA.

Figure 5.13



ANNULAR RADIAL SUMMATION PLOT FOR THE H DATA.

Figure 5.14



ANNULAR RADIAL SUMMATION PLOT FOR THE K DATA.

Figure 5.15

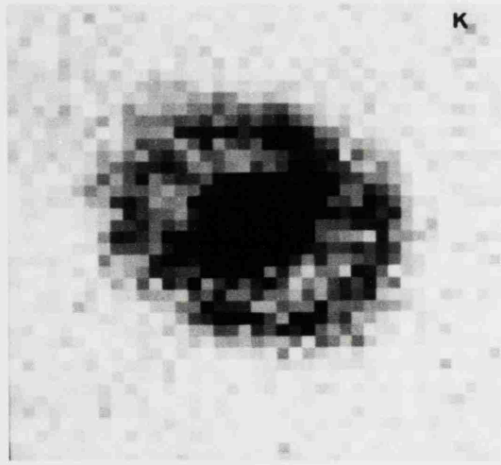
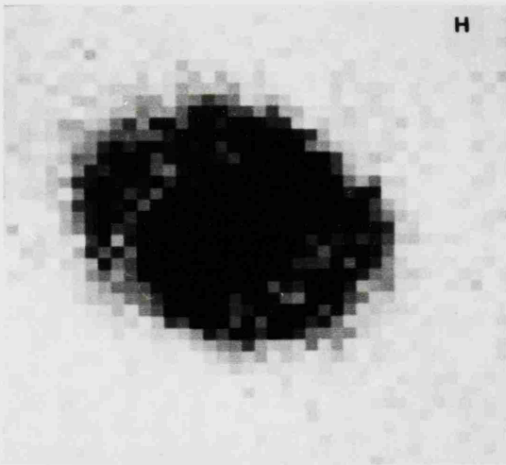
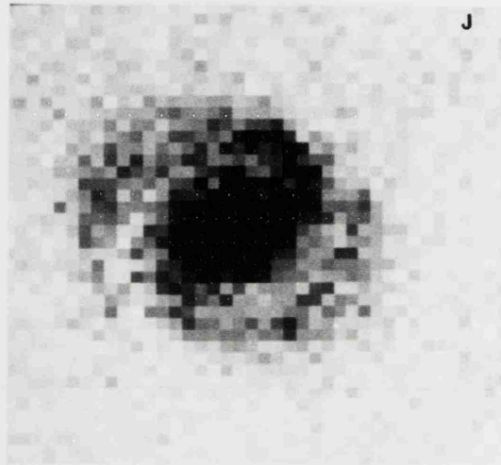
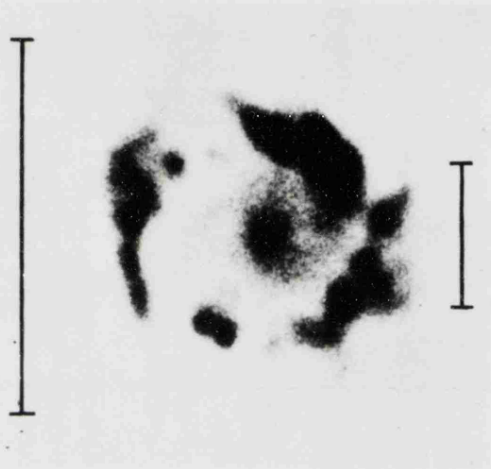
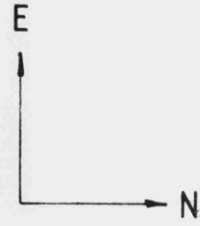
have been enlarged and the signal to noise improved so that the maximum semi-major axis in the annular radial plots could have been extended ( this is true for all the galaxies in this chapter ). This would have helped in estimating the exponential disc law at a distance where the transient star formation, the  $R^{1/4}$  law would have little effect and the discontinuity, at 10 arcseconds, may have become more distinct.

The J-H and H-K colours of the nucleus are 0.88,0.39,0.78 and 0.39 for the map data and 5 arcsecond spot photometry respectively. This places the nucleus very close to the reddening vector on Figure 5.22. It also lies some distance from the normal galactic nuclei colour region which indicates that the nucleus probably suffers from reddening (  $A_v \approx 1.4$  magnitudes ) or is, perhaps, a marginally active nucleus.

ii) NGC 1097

The morphological classification of this galaxy is SB(s)b and its redshift places it a distance of 17Mpc. The optical photograph of this galaxy ( Plate 5.2 (a) ) seems to indicate an almost complete ring around the nucleus. The J, H and K contour plots ( Figure 5.16, 5.17 and 5.18 ) indicate that a bar is extending out to this ring. Improved J, H and K greyscale pictures, from a later trip, are shown on Plate 5.2 where the bar is more prominent. This bar extends out to meet the ring at 8.5 arcseconds (  $0.7\text{kpc} \approx 1\text{kpc}$  for an inclination of  $0^\circ$  ) from the nucleus.

Osmer et al (1974) and Phillips et al (1984) both agree

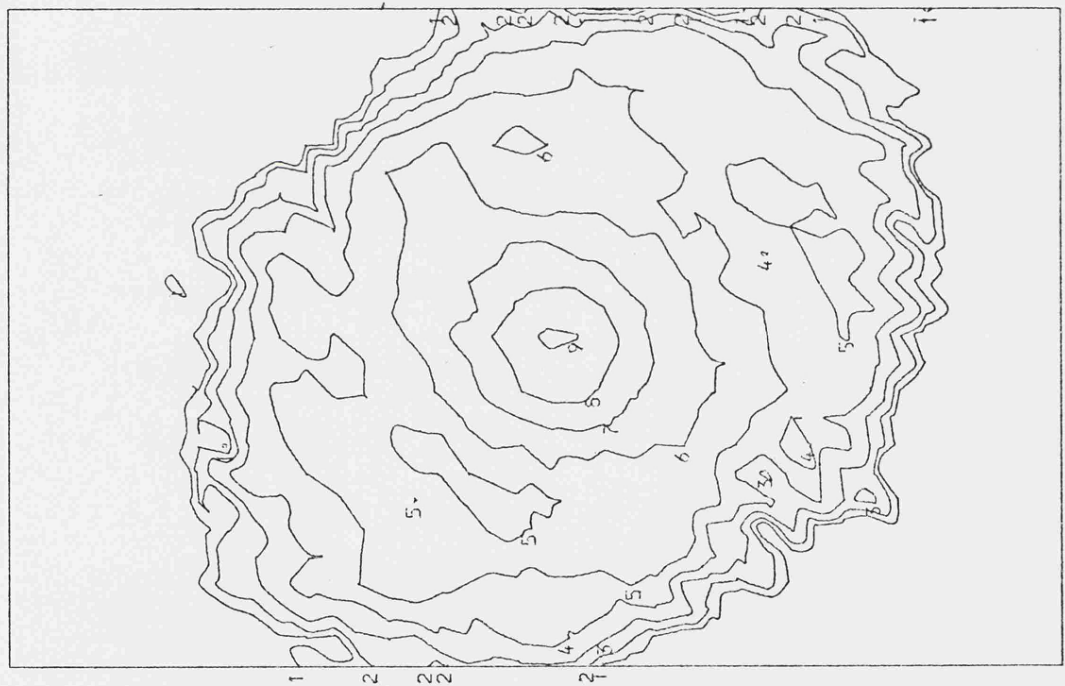
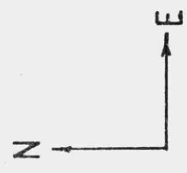


SCALE : 0.59 ARCSECONDS PER MILLIMETRE

Plate 5.2

5.33

LOWEST CONTOUR = 20.41 mag/arcsec<sup>2</sup> .  
PEAK READING = 16.29 mag/arcsec?



BEAM SIZE.

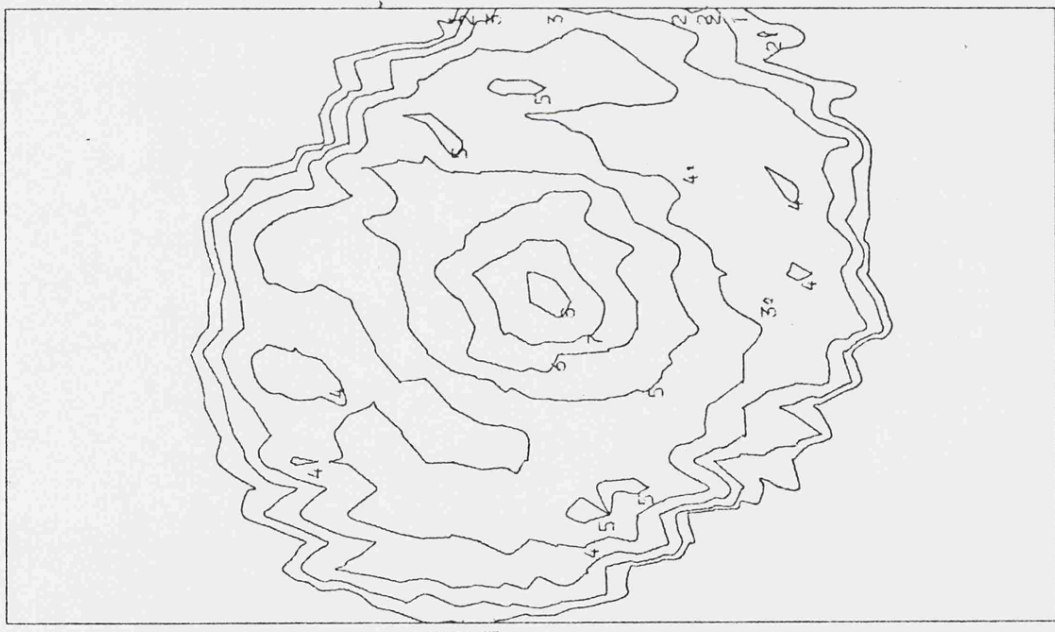
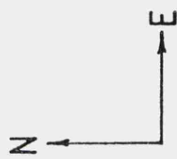
SCALE : 0.29 ARCSECONDS PER MILLIMETRE

J CONTOUR PLOT OF NGC 1097.

Figure 5.16

LOWEST CONTOUR = 19.17 mag / arcsec<sup>2</sup>

PEAK READING = 15.46 mag / arcsec<sup>2</sup>



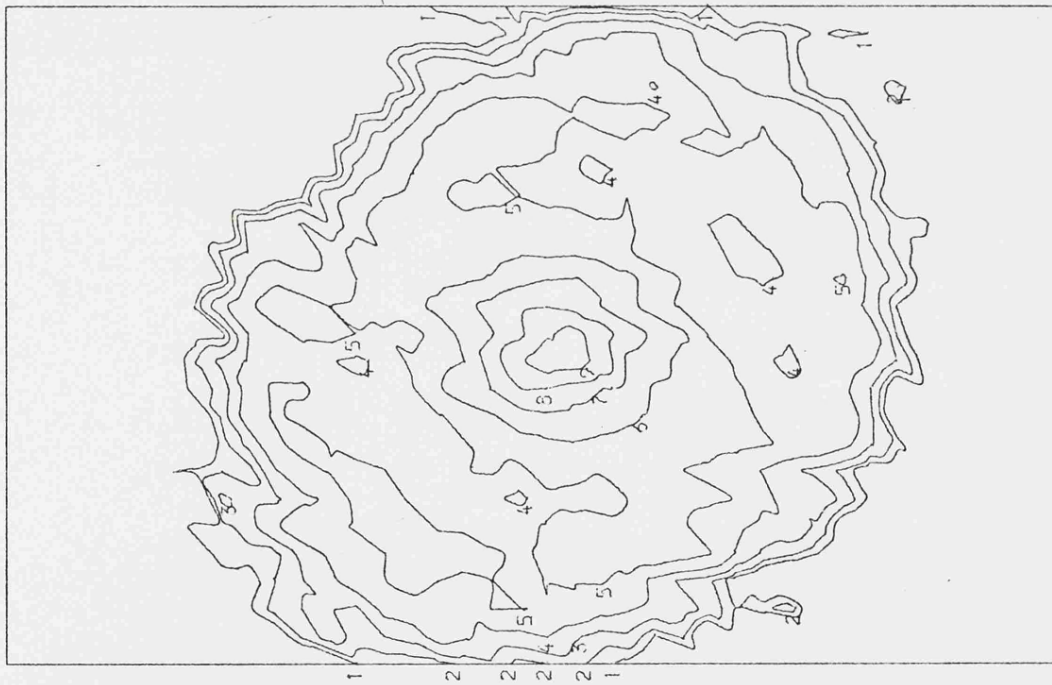
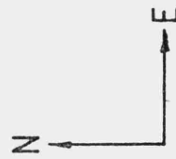
BEAM SIZE.

SCALE : 0.29 ARCSECONDS PER MILLIMETRE

H CONTOUR PLOT OF NGC 1097.

Figure 5.17

LOWEST CONTOUR = 19.04 mag / arcsec<sup>2</sup>  
PEAK READING = 14.74 mag / arcsec<sup>2</sup>



BEAM SIZE.

SCALE : 0.29 ARCSECONDS PER MILLIMETRE

K CONTOUR PLOT OF NGC 1097.

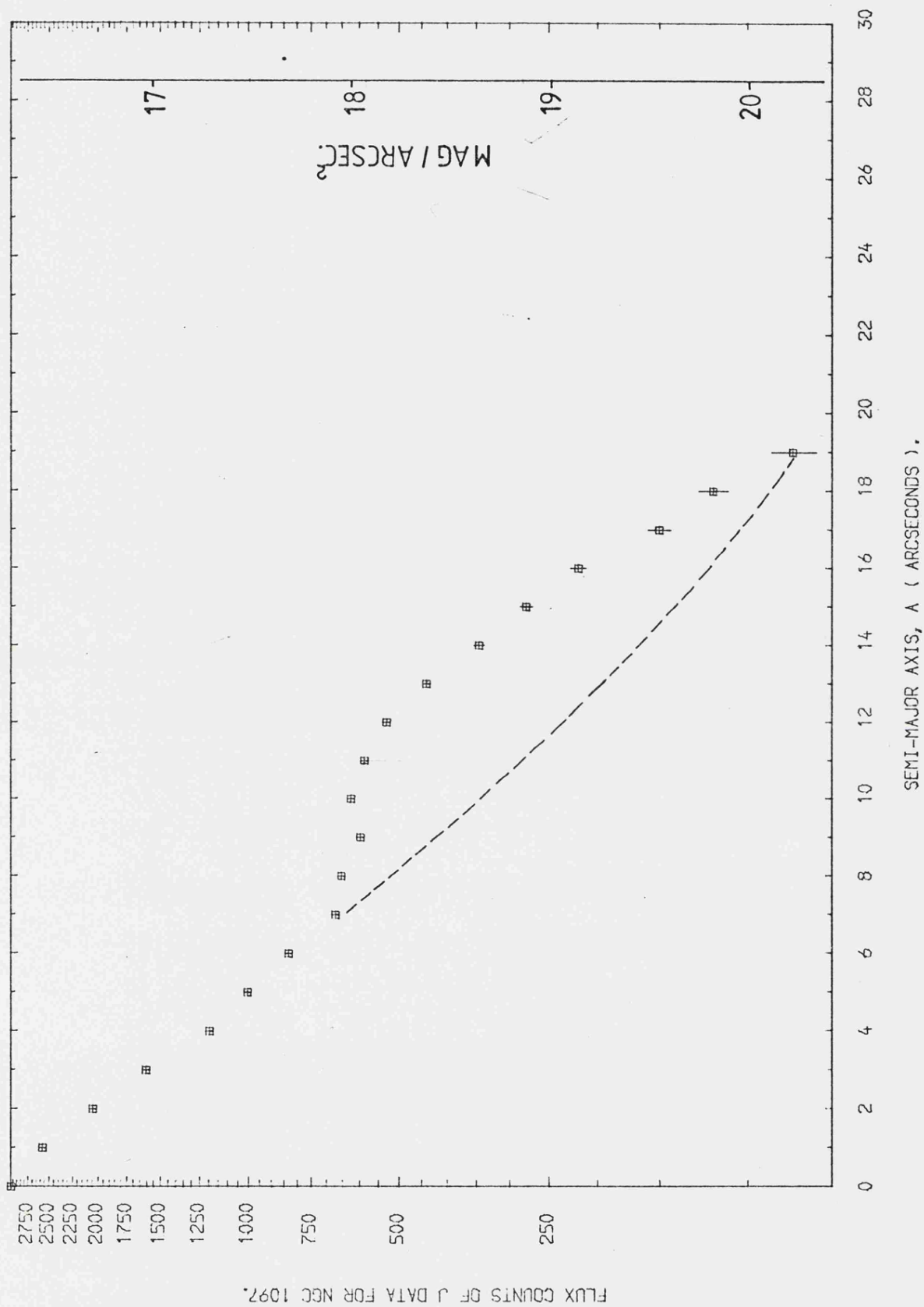
Figure 5.18

that the ring has a substantial population of young hot stars surrounded by HII regions. The nuclear continuum is shown, by Talent (1982) and Phillips et al, to be dominated by late-type stars and turns out to be very similar to that of an elliptical galaxy.

Blackman (1981) obtained a rotation curve which showed a near constant velocity on either side of the nucleus from 5 to 20 arcseconds. Within the inner radius the rotation curve is almost identical to that of a solid body and Blackman estimated the mass within this radius to be  $7.2 \times 10^9 M_{\odot}$ .

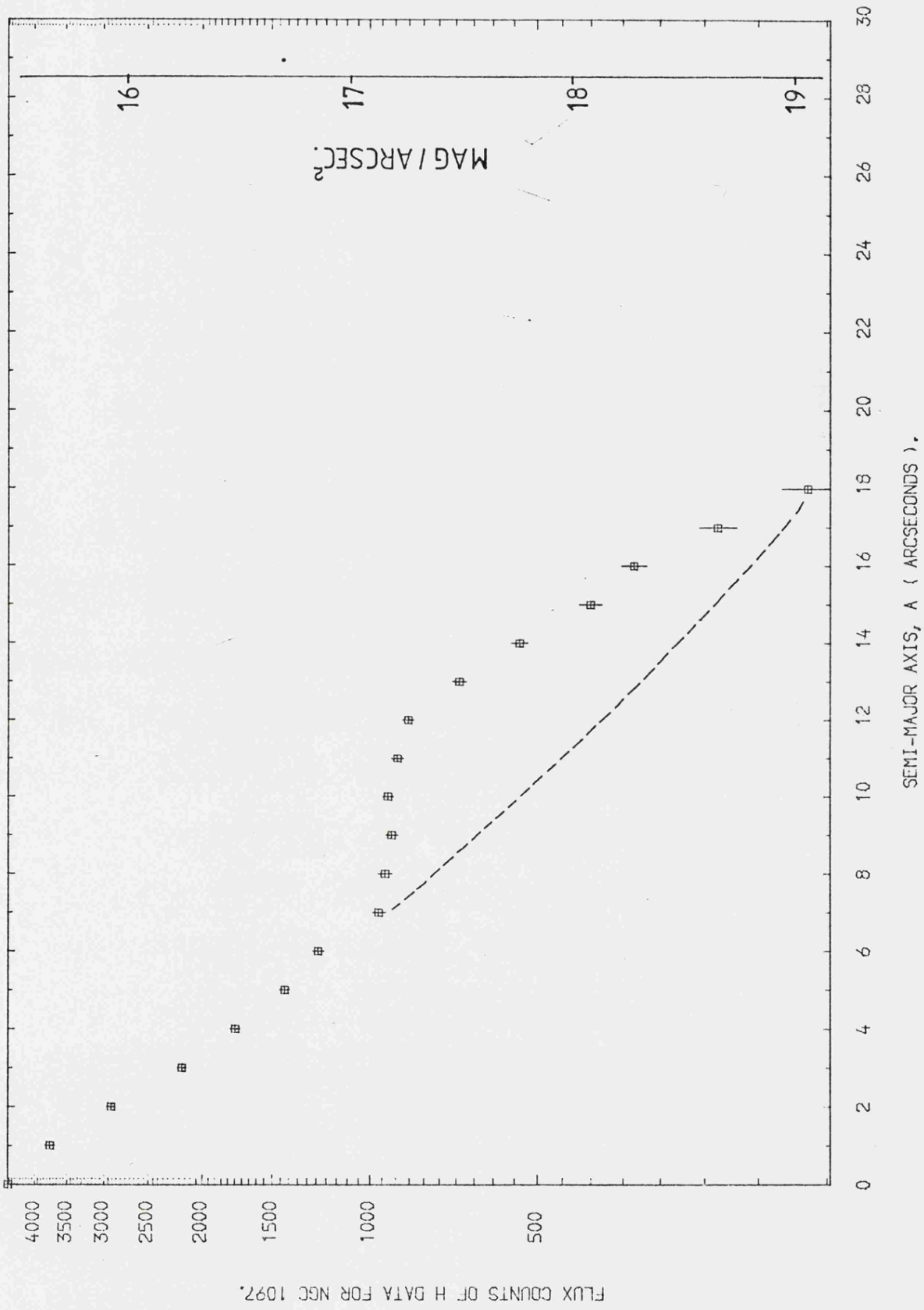
The determination of the inclination and PA, from the maps, proved to be rather awkward since the isophotes were almost circular. However, on averaging all the estimates, results were obtained which are in very good agreement with other peoples values. Therefore, these estimates were used in the annular radial summation analysis.

The annular radial summation plots of the J, H and K data ( shown in Figures 5.19, 5.20 and 5.21 ) all exhibit, what appear to be, excess counts from 8 to 18 arcseconds. Within this ring the young blue star population must be low since Talent and Phillips et al both showed that the nuclear continuum was dominated by late type stars. The dotted curve is an attempt at extrapolating the galaxy profile seen in normal galaxies. The colours of a region 11 arcseconds from the nucleus were determined for the extrapolated curve and the observed counts. The vector joining the two should give an indication as to what the sources, perturbing the annular radial profile, are. The colours derived for the extrapolated curve at 11 arcseconds



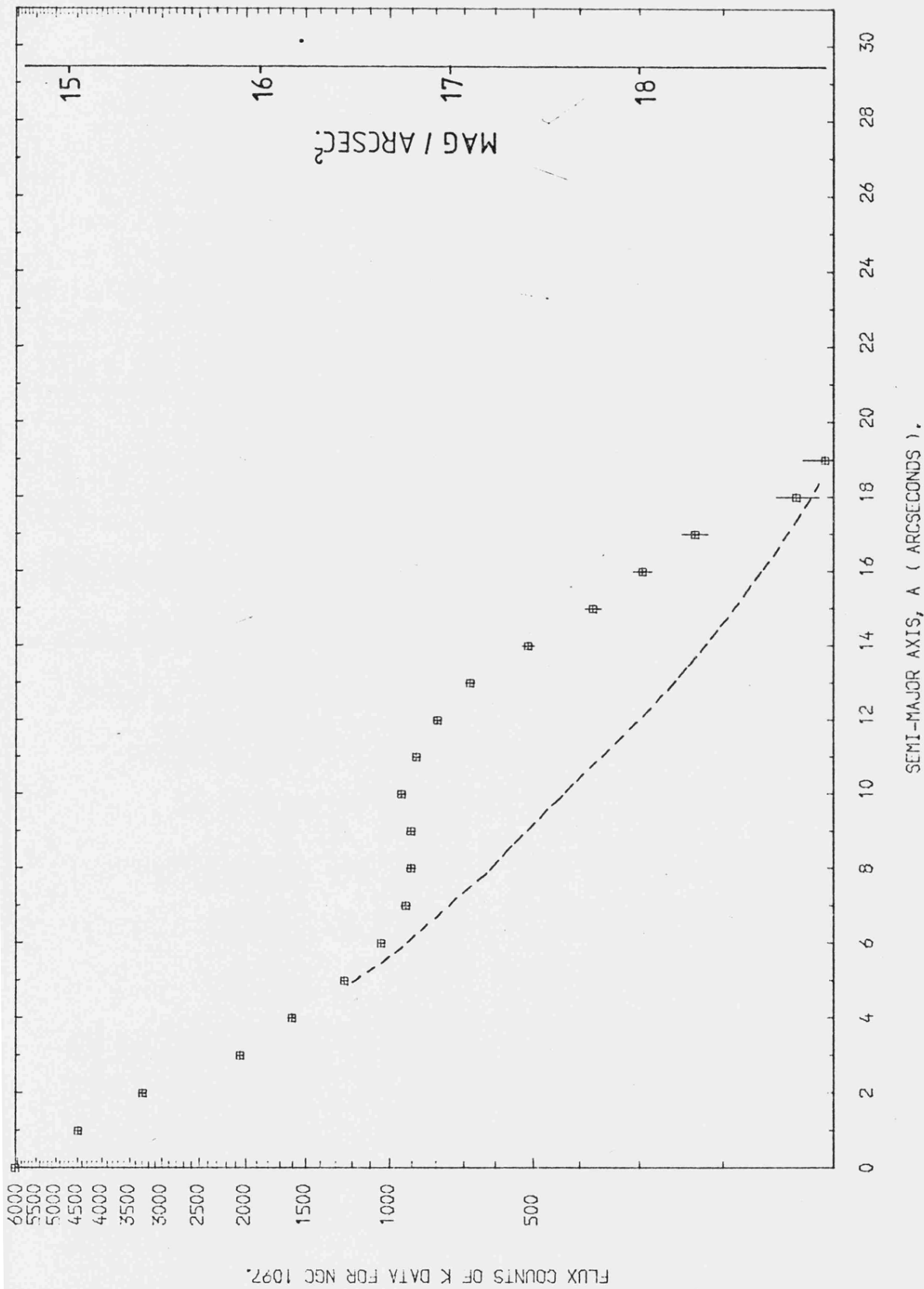
ANNULAR RADIAL SUMMATION PLOTS FOR THE J DATA.

Figure 5.19



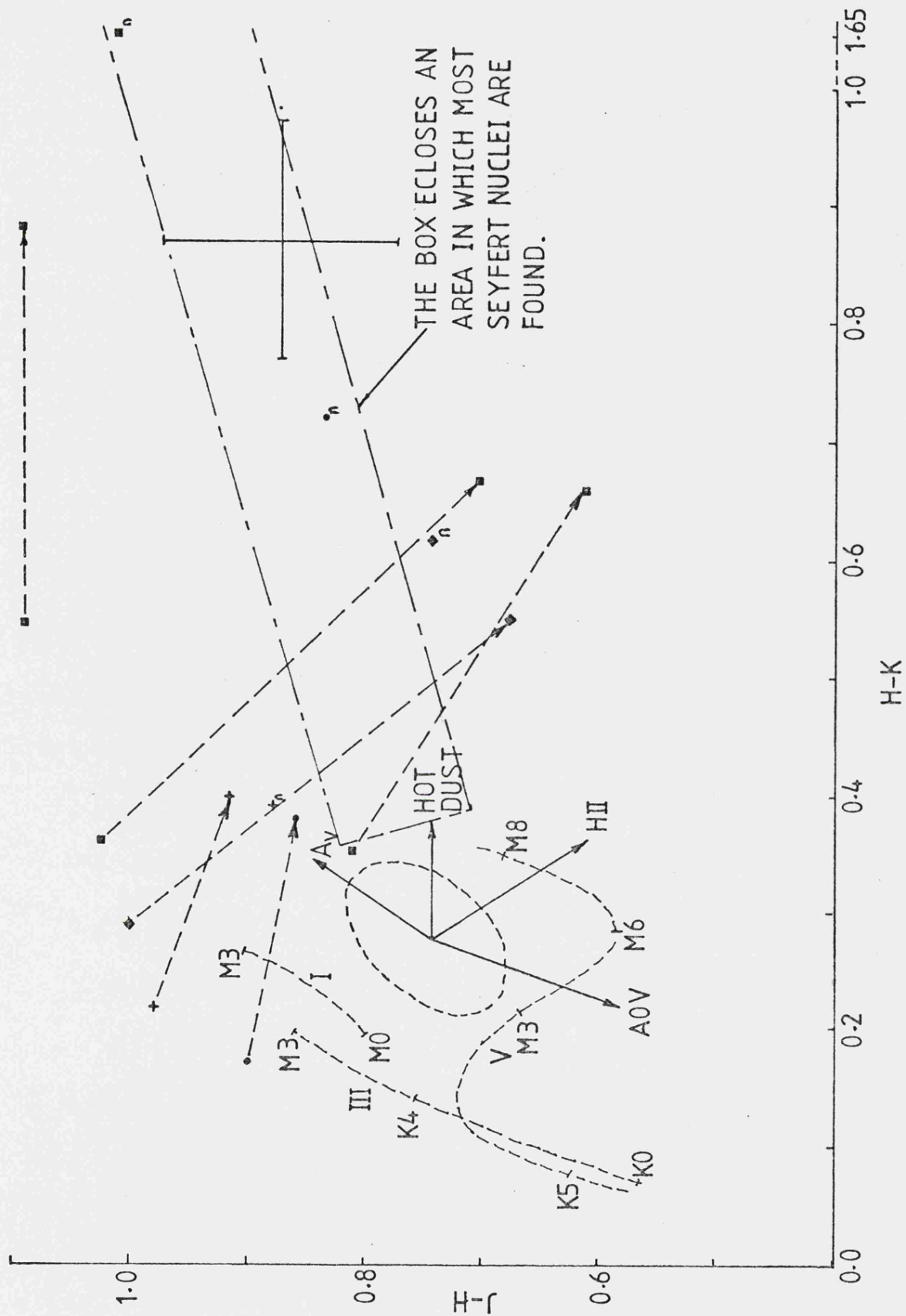
ANNULAR RADIAL SUMMATION PLOTS FOR THE H DATA.

Figure 5.20



ANNULAR RADIAL SUMMATION PLOTS FOR THE K DATA.

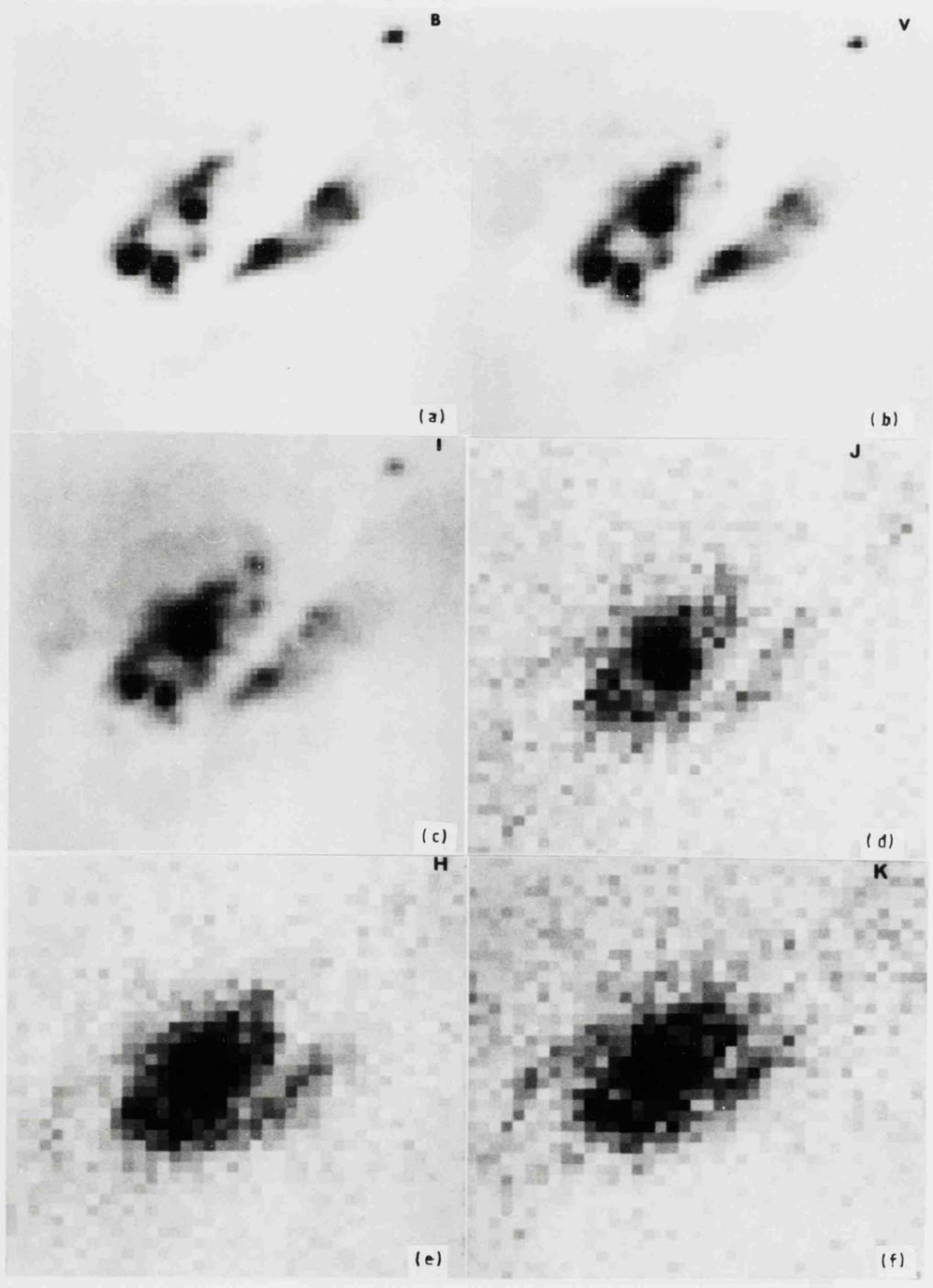
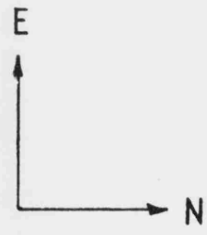
Figure 5.21



+ NGC 613; • NGC 1097; ■ NGC 1365; ♦ NGC 1808  
 WHERE SUBSCRIPT  $n$  IS THE NUCLEAR COLOUR OF THE PARTICULAR  
 GALAXY ( FOR THE POSITION OF THE POINTS SEE TEXT ) AND THE  
 REDDENING VECTOR HAS A LENGTH  $A_V = 1.0$  MAGNITUDE.

J-H VS H-K PLOT

Figure 5.22



SCALE : 0.64 ARCSECONDS PER MILLIMETRE

Plate 5.3

from the nucleus ( shown in Table 5.3 ) are 0.90 and 0.17 for J-H and H-K respectively. However, the observed counts give colours of 0.86 and 0.38 for J-H and H-K respectively. The vector joining these two points, shown in Figure 5.22, can be reproduced by a combination of HII regions and hot dust. One must conclude that the ring region has a large number of HII regions and hot dust within it. This is in good agreement with the results of Osmer et al and Phillips et al. Prabhu (1980) obtained an equivalent radial profile very similar to those in Figures 5.19 to 5.21.

The nuclear colours from the 5 and 10 arcsecond spot photometries, listed in Table 5.4, indicate that the nucleus has colours similar to that of an active galaxy ( see Aaronson (1977) ). Alternatively, one could take the view that the nucleus is surrounded by hot dust and, therefore, also slightly reddened.

### iii) NGC 1365

This galaxy, which has a morphological classification of SB(s)b and is at a distance of 20Mpc, has been studied extensively by many people and is thought to be an intermediate Seyfert ( see Veron et al (1980) and Edmunds and Pagel (1982) ).

The blue CCD image of this galaxy, taken at the AAT, ( Plate 5.3 (a) ) shows three very distinct hot-spots, the first two are 5.7 arcseconds to the south-west and the third is 7.1 arcseconds to the north-west of the nucleus.

The hot-spots have narrow Balmer lines and Edmunds and Pagel concluded that these regions were normal HII

NGC No.		J	H	K	J-H	H-K	POSITION
		(mag)	(mag)	(mag)	(mag)	(mag)	
613	(O)	19.22	18.31	17.91	0.91	0.40	4 arcseconds NW of nucleus.
	(E)	19.95	18.97	18.76	0.98	0.21	
613		18.21	17.33	16.94	0.88	0.39	Nucleus.
1097		16.29	15.46	14.74	0.83	0.72	Nucleus.
1097	(O)	18.07	17.21	16.83	0.86	0.32	11 arcseconds from nucleus from annular radial profile plots.
	(E)	18.85	17.95	17.78	0.90	0.17	
1365		16.16	15.15	13.50	1.01	1.65	Nucleus.
1365	(O)	17.72	17.02	16.35	0.70	0.67	5 arcseconds SW of nucleus.
	(E)	18.28	17.26	16.90	1.02	0.36	
1365	(O)	17.77	17.16	16.50	0.61	0.66	7 arcseconds NW of nucleus.
	(E)	18.33	17.52	17.17	0.81	0.35	
1365	(O)	16.83	15.74	14.86	1.09	0.88	3 arcseconds from nucleus from annular radial profile plots.
	(E)	16.83	15.74	15.19	1.09	0.55	
1808		15.46	14.72	14.10	0.74	0.62	Nucleus.
1808	(O)	17.00	16.32	15.77	0.68	0.55	6 arcseconds SE of nucleus.
	(E)	17.66	16.66	16.37	1.00	0.29	

ALL COLOURS HAVE BEEN OBTAINED FROM THE MAPS FOR A BEAM DIAMETER OF 2 ( OR 3.5 FOR NGC1365 ) ARCSECONDS UNLESS OTHERWISE STATED.

(O) ... OBSERVED MAGNITUDES AND COLOURS.  
(E) ... EXTRAPOLATED MAGNITUDES AND COLOURS.

TABLE 5.3

complexes. Edmunds and Pagel also showed that the nucleus has broad emission lines ( eg H $\alpha$  with a FWHM  $\approx$  1600km/s ) although these lines all exhibited an asymmetry towards the blue. Similar emission line asymmetries are observed in

some Seyfert 2 galaxies such as NGC 1808 and 2997. They concluded that this could be "...attributed either to the presence of some rapidly moving clouds coming preferentially towards us or to multiple scattering in a moving cloudy medium...".

Looking at the B to K images on Plate 5.3, from a later trip to the AAT, and the J to K contour plots from the earlier trip ( Figure 5.23, 5.24 and 5.25 ) the most striking feature is that the nucleus begins to dominate towards longer wavelengths. This compares favourably with the 8 to 13 $\mu$ m and 0.4 to 0.7 $\mu$ m spectra, from Roche et al (1984) and Edmunds and Pagel respectively, where the nuclear continuum is steepening towards longer wavelengths. Glass (1973), Aaronson (1977) and Frogel et al (1982) all proposed that the nucleus has substantial amounts of hot dust within it. In fact, Frogel et al concluded that this hot dust extends to approximately 10 arcseconds from the nucleus. This would account for the steepening of the continuum towards longer wavelengths. The spiral arms also become more prominent in Plate 5.3, although a bar is not as evident in the nuclear region as was the case in the two earlier galaxies.

The 10 arcsecond beam diameter spot photometry colours and the 2 arcsecond beam diameter colours from the map of the nucleus, listed in Table 5.4, show that the nucleus is displaced a large distance from the region where normal galactic nuclei are found. This can be explained by the hot dust and strong reddening pointed out in the earlier paragraph.

The hot-spot region to the south-west has colours, from



LOWEST CONTOUR = 21.05 mag / arcsec<sup>2</sup>

PEAK READING = 16.16 mag / arcsec<sup>2</sup>



BEAM SIZE.

SCALE : 0.32 ARCSECONDS PER MILLIMETRE

J CONTOUR PLOT OF NGC 1365.

Figure 5.23



LOWEST CONTOUR = 19.69 mag / arcsec<sup>2</sup>

PEAK READING = 15.15 mag / arcsec<sup>2</sup>

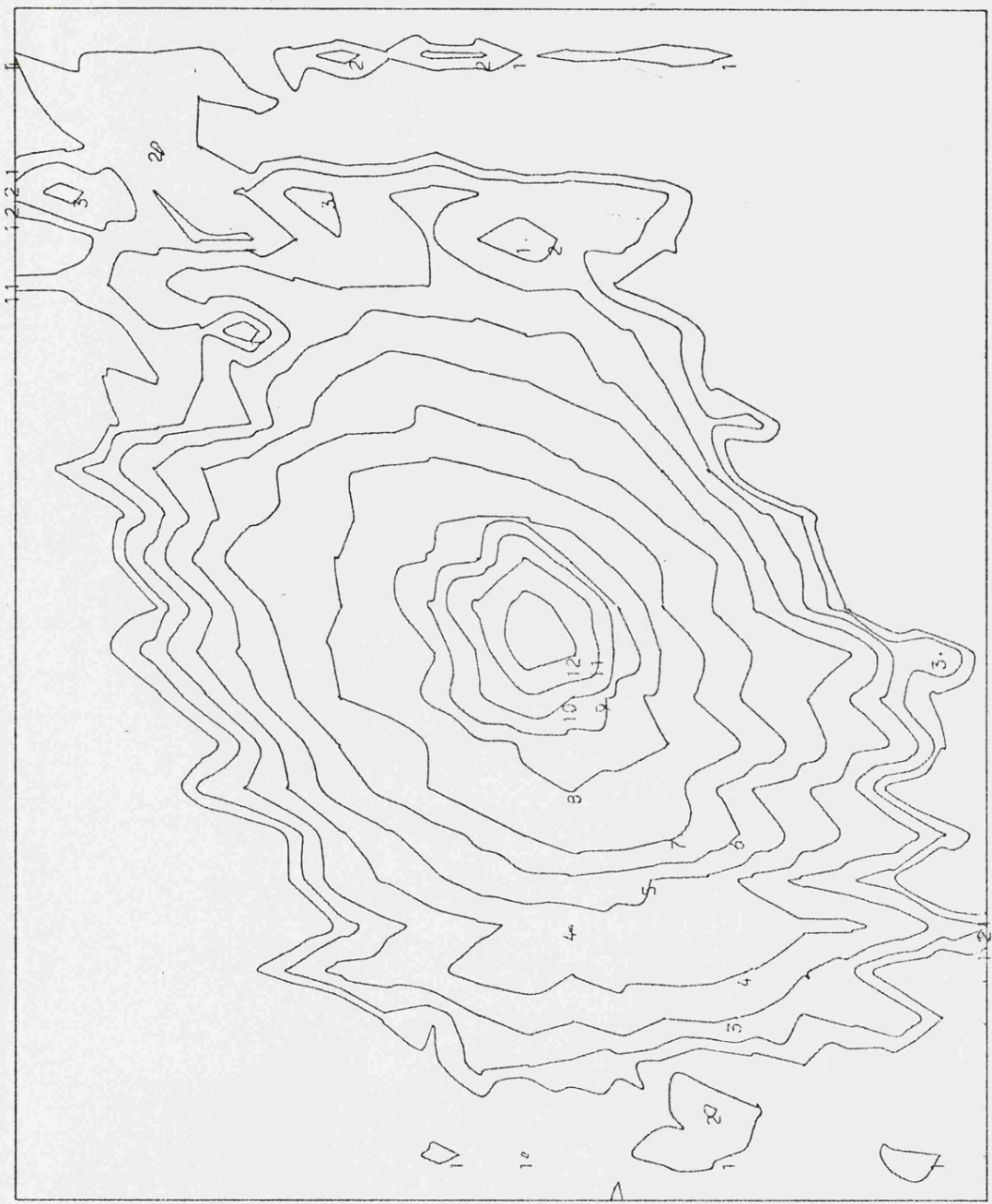
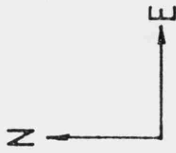


BEAM SIZE.

SCALE : 0.32 ARCSECONDS PER MILLIMETRE

H CONTOUR PLOT OF NGC 1365.

Figure 5.24



BEAM SIZE.  
LOWEST CONTOUR = 19.26 mag / arcsec.  
PEAK READING = 13.5 mag / arcsec.

SCALE : 0.32 ARCSECONDS PER MILLIMETRE

K CONTOUR PLOT OF NGC 1365.

Figure 5.25

-----  
 NGC NUMBER.  
 -----

	613		1097		1365		1808	
BEAM SIZE	J-H	H-K	J-H	H-K	J-H	H-K	J-H	H-K
IN ARCSEC	ALL COLOURS ARE IN MAGNITUDES							
	ERRORS = $\pm 0.1$ MAGNITUDES							
-----								
2.0 (3.5) CM	0.88	0.39	0.83	0.72	1.01	1.65	0.74	0.62
4.5 (7.9) SM	0.87	0.33	0.81	0.55	1.08	1.40	0.93	0.44
6.8 (11.8) SM	0.89	0.33	0.73	0.48	1.04	1.04	0.96	0.44
11.3 (19.7) SM	0.83	0.34	0.74	0.41	1.01	0.89	0.92	0.45
15.8 (27.6) SM	0.82	0.39	0.76	0.37	0.98	0.83	0.90	0.45
5 CP	0.78	0.39	0.89	0.34	-	-	0.94	0.50
10 CP	0.82	0.39	0.86	0.30	0.99	0.90	-	-
-----								

NOTE:-

C - CIRCULAR APERTURE USED.

S - SQUARE APERTURE USED BUT THEIR DIAMETERS ARE QUOTED IN EQUIVALENT CIRCULAR APERTURE DIAMETERS.

M - COLOURS OBTAINED FROM MAP DATA.

P - SPOT PHOTOMETRY.

THE BEAM SIZES IN ROUND BRACKETS ARE THE EQUIVALENT BEAM SIZES FOR NGC 1365 ONLY.

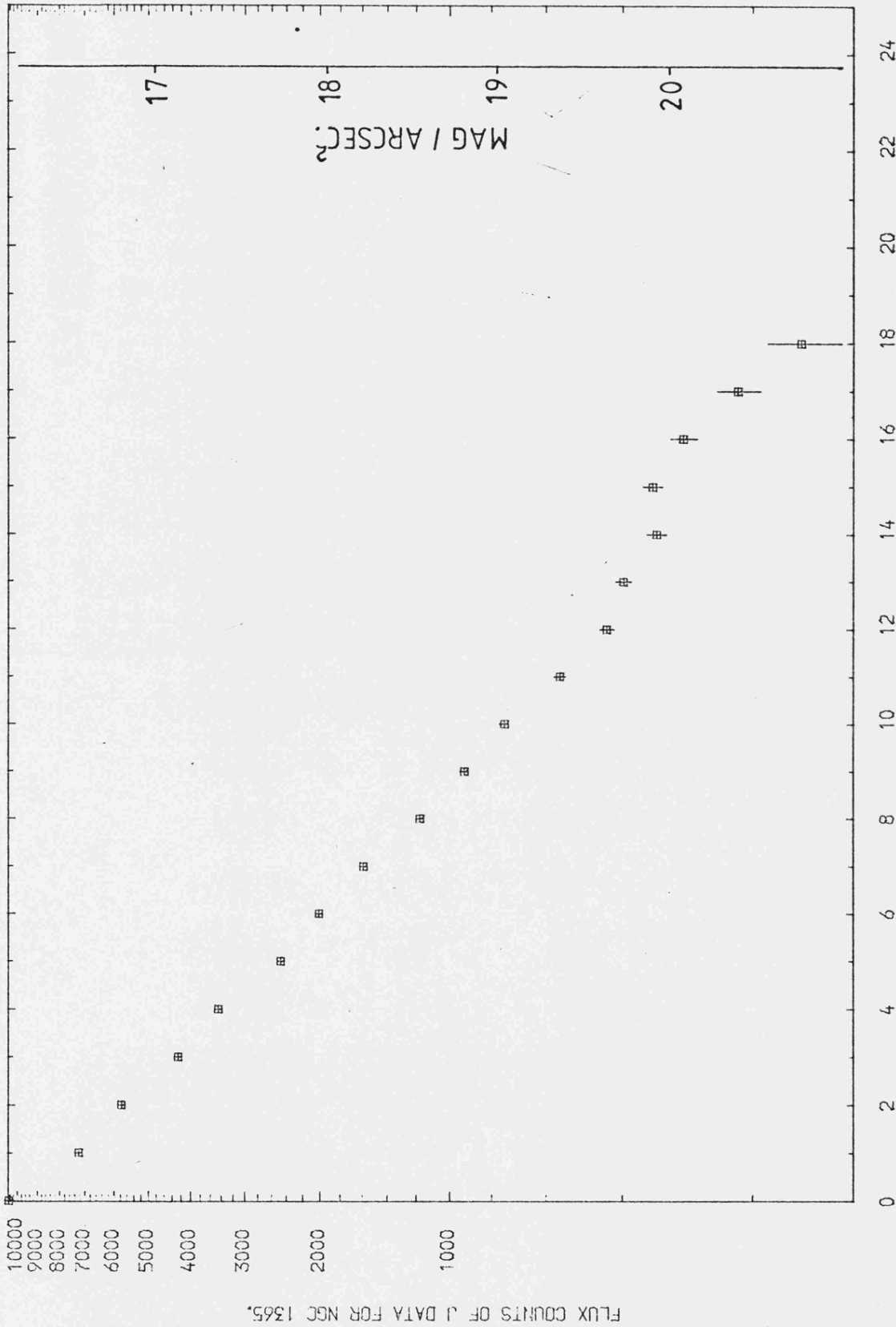
TABLE 5.4

the map data, of 0.70 and 0.67 for J-H and H-K respectively. The hot-spot to the north-west has colours of 0.61 and 0.66 for J-H and H-K respectively. Yet again, to determine the processes causing the excess counts, it was necessary to extrapolate what was thought to be the

galaxy's underlying profile. The extrapolated colours are shown in Table 5.3 and are plotted on Figure 5.22. The two vectors joining the colours of these regions before and after extrapolation of the galaxy's profile are indicative of the presence of HII regions and hot dust. These vectors agree with the findings of Osmer et al (1974) and Edmunds and Pagel (1982).

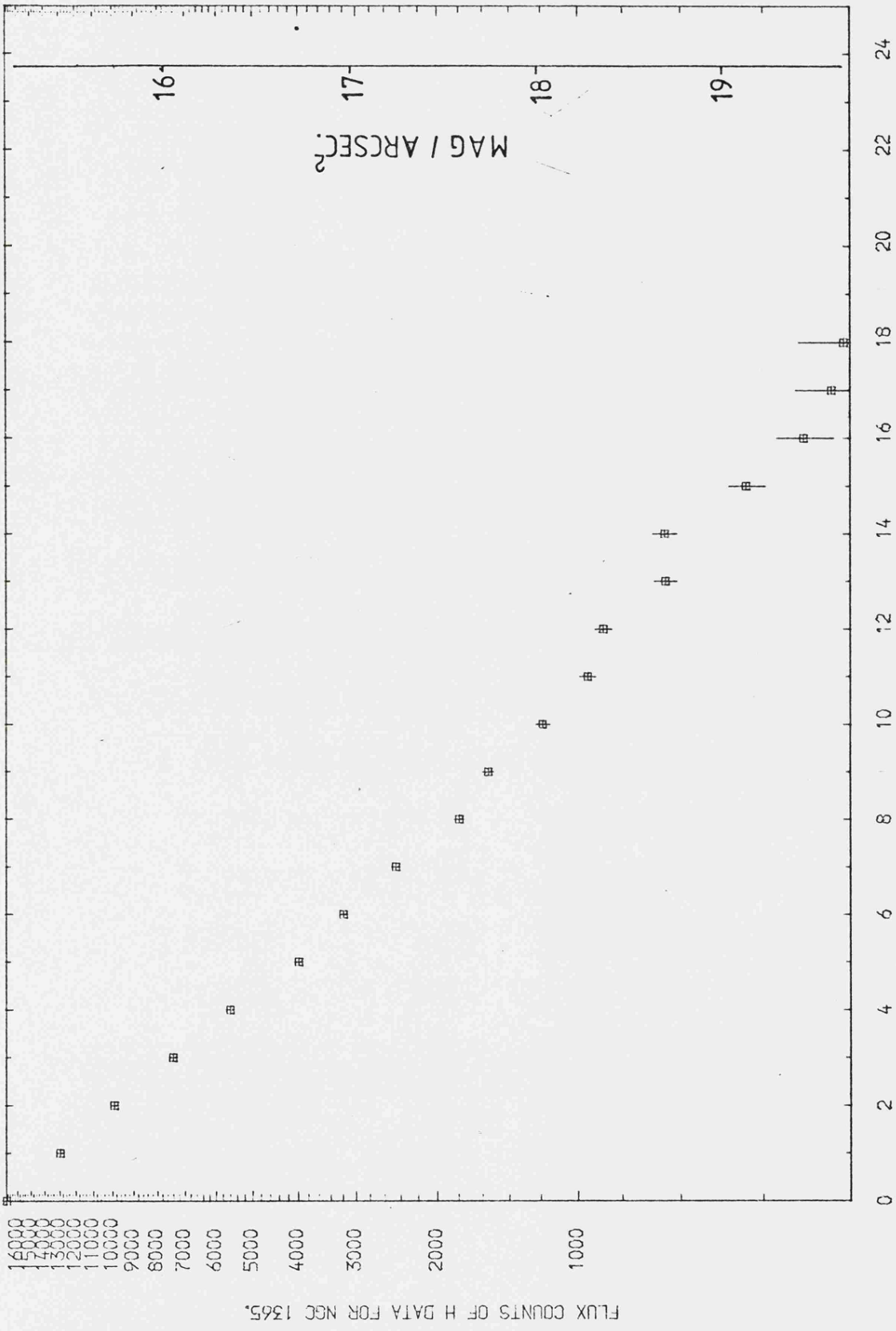
The inclination and PA, in Table 5.2, are in good agreement with other people's estimates, although the values of de Vaucouleurs and Burbidge are significantly different from those of Wright and Blackman. Despite this, the inclination and PA, derived from the method described in this thesis, were used in conducting the annular radial summations.

The annular radial summation profiles ( see Figures 5.26, 5.27 and 5.28 ) show no distinct features, unlike NGC 1097, although the J and K data do show a faint feature at approximately 21 arcseconds from the nucleus and yet the H data does not. This is probably due to a slight error in the background level being used for the H data since this was the worst scan for background drifts. The K data shows a change in gradient at 4.5 arcseconds from the nucleus and yet the other two wavelengths show absolutely no change in their slopes at this point. An extrapolation of the K profile, shown on Figure 5.28, and the resulting colours of the region 3.5 arcseconds from the nucleus are shown in Table 5.3. As can be seen on Figure 5.22, emission from hot dust would explain the excess emission seen and would also account for the spot photometry colours. The excess emission extends into the nucleus as can be seen in Figure



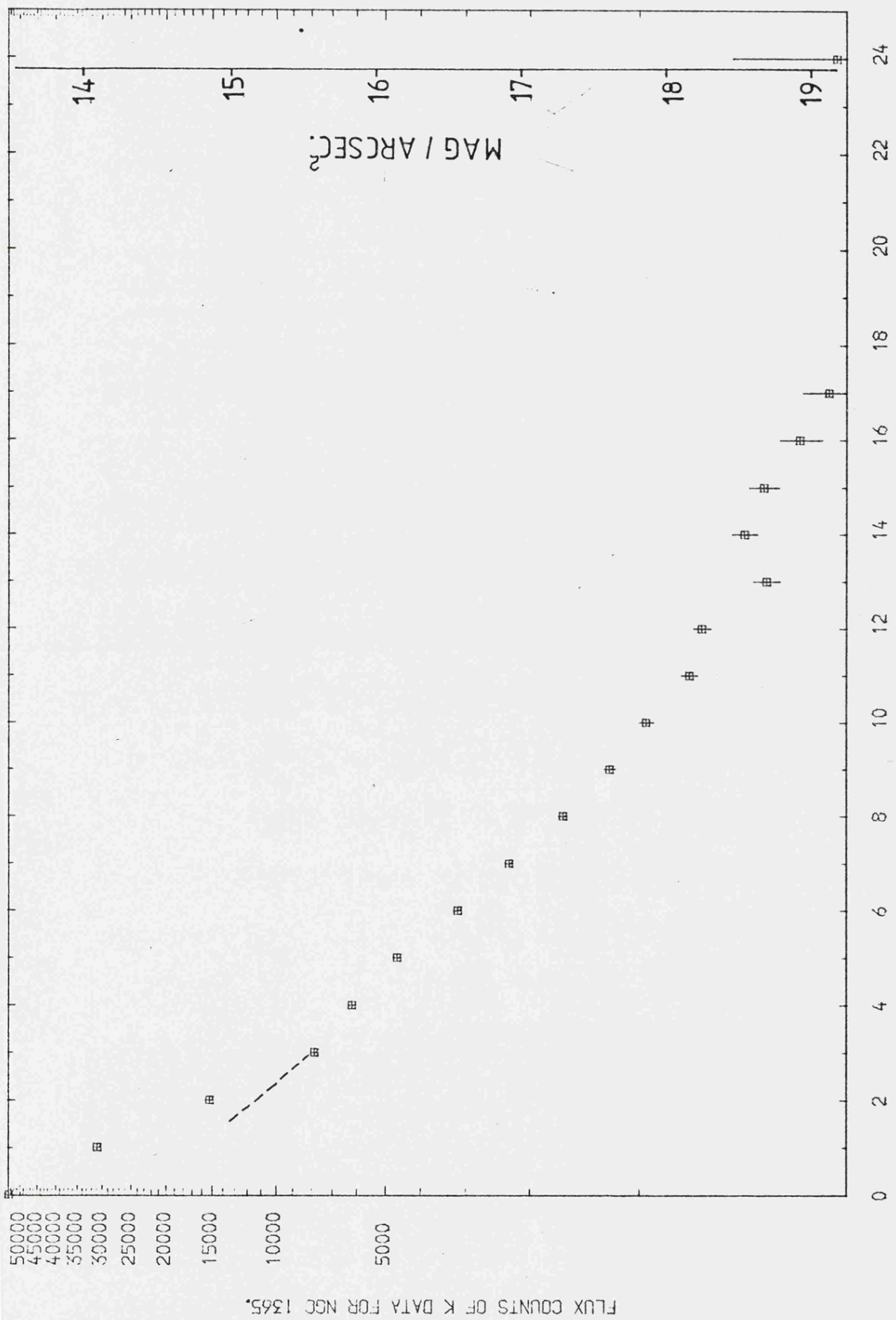
ANNULAR RADIAL SUMMATION PLOT FOR THE J DATA.

Figure 5.26



ANNULAR RADIAL SUMMATION PLOT FOR THE H DATA.

Figure 5.27



ANNULAR RADIAL SUMMATION PLOT FOR THE K DATA.

Figure 5.28

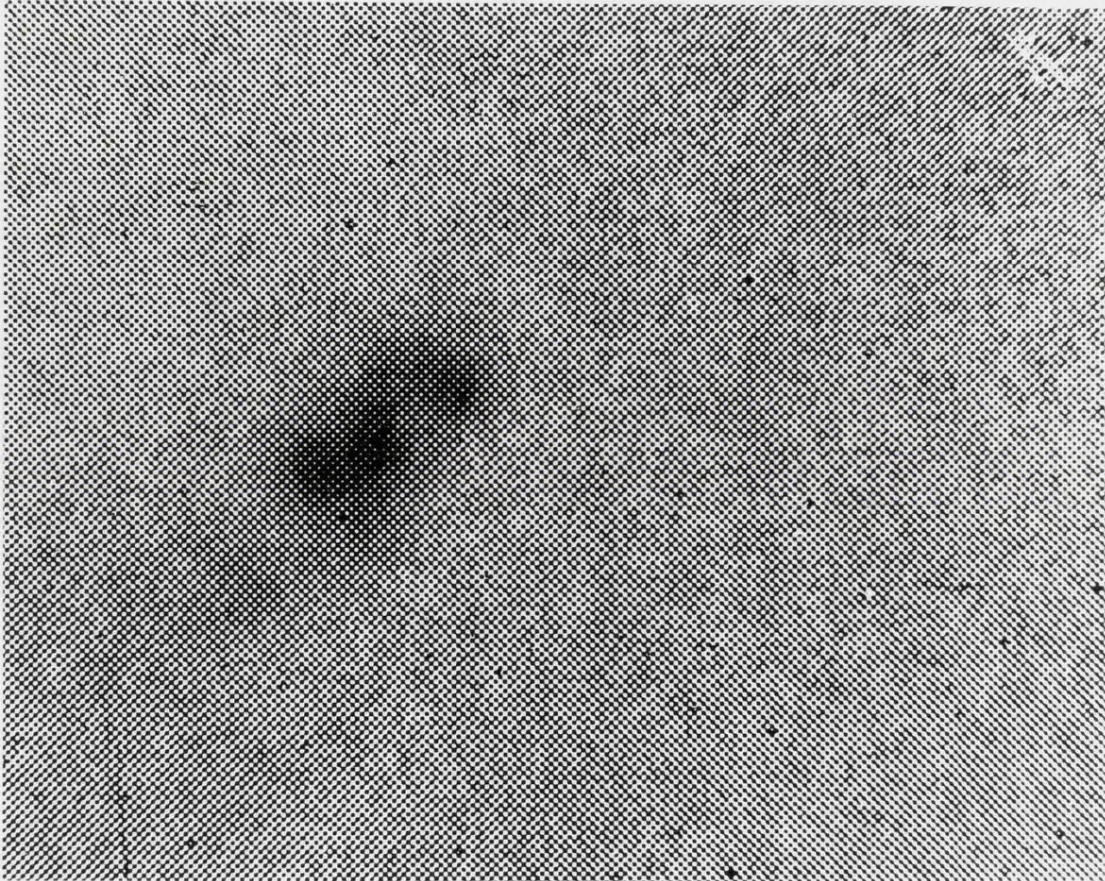
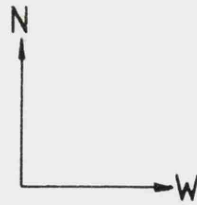
5.28 and so one can assume that the nucleus must also suffer from excess emission from hot dust. The extrapolated colours have simply to be dereddened ( $A_V \approx 3.5$  magnitudes) to return the colours to the normal galactic nuclei region. This supports the findings of Glass, Aaronson and Frogel et al, which were discussed earlier.

iv) NGC 1808

The distance of this Seyfert 2 galaxy is estimated to be 10Mpc, by Burbidge and Burbidge (1968), and has a morphological classification of RSAB(s)a, where R indicates that there is an outer ring to the galaxy. Burbidge and Burbidge pointed out that this galaxy appeared to be very dusty and seems to have radial dust lanes emanating from the nucleus.

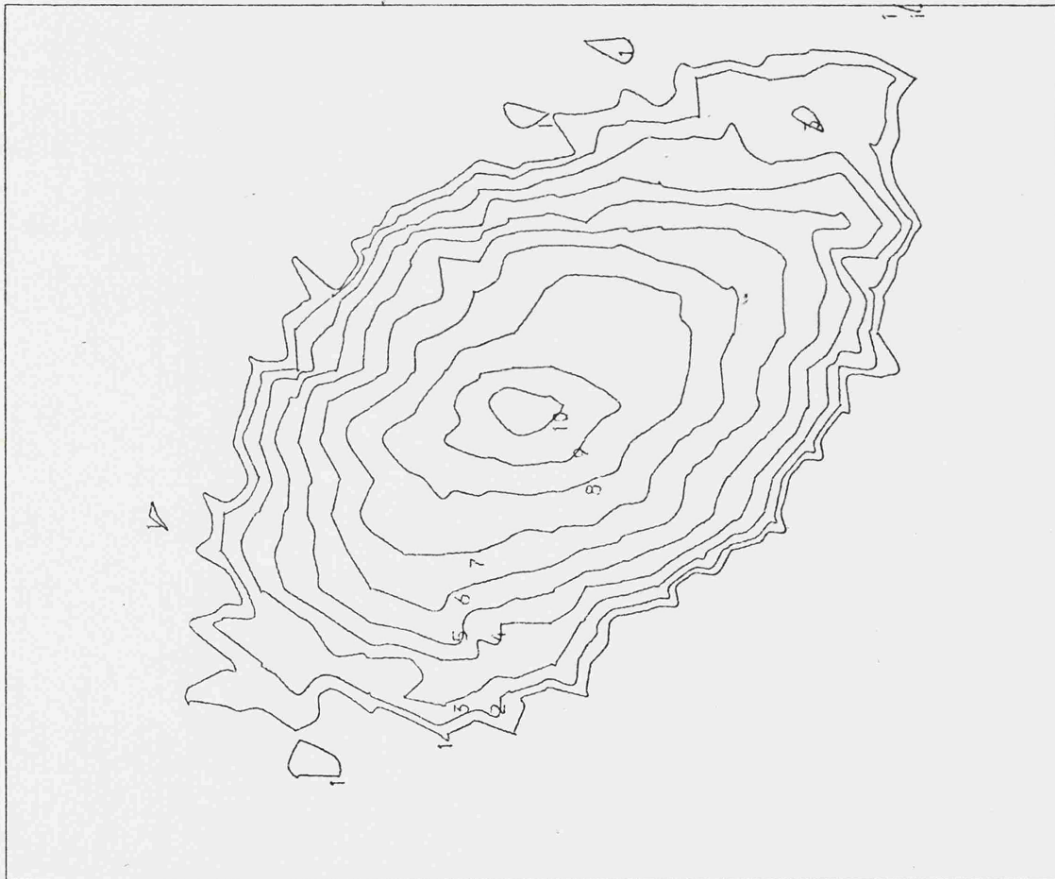
The short exposure optical photograph of the nucleus, shown in Plate 5.4, seems to possess an 'S' shape of which the central bright spot was initially thought, by Burbidge and Burbidge, to be the nucleus. However, the asymmetry of the rotational velocity curve obtained by them, showed that the bright spot was not the centre of mass. They concluded, by folding the radial profile at different points, that the centre of mass was 4 arcseconds ( $\approx 200\text{pc}$ ) to the south-east of the bright spot. However, by superimposing our J, H and K contour plots on the optical photograph, the indications are that the nucleus is only 1.5 arcseconds to the south-east of this bright spot.

The J, H and K contour plots, shown in Figures 5.29, 5.30 and 5.31, show no prominent features, although there may be



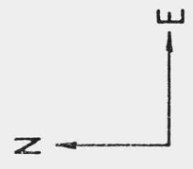
SCALE : 0.21 ARCSECONDS PER MILLIMETRE

Plate 5.4



LOWEST CONTOUR = 20.29 mag/arcsec<sup>2</sup>

PEAK READING = 15.46 mag/arcsec<sup>2</sup>



BEAM SIZE.

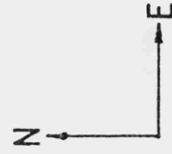
SCALE : 0.21 ARCSECONDS PER MILLIMETRE

J CONTOUR PLOT OF NGC 1808.

Figure 5.29

LOWEST CONTOUR =  $19.84 \text{ mag/arcsec}^2$

PEAK READING =  $14.72 \text{ mag/arcsec}^2$



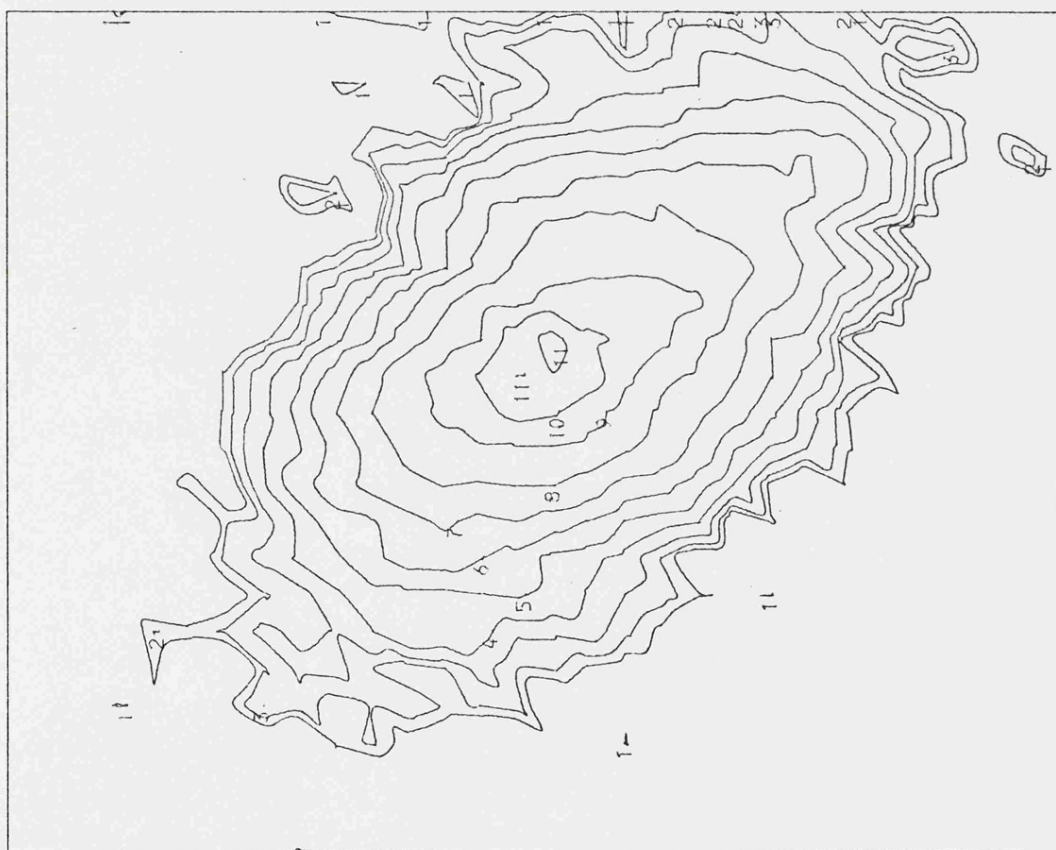
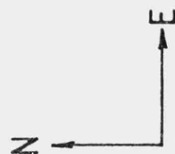
BEAM SIZE.

SCALE : 0.21 ARCSECONDS PER MILLIMETRE

H CONTOUR PLOT OF NGC 1808.

Figure 5.30

LOWEST CONTOUR = 19.26 mag/arcsec<sup>2</sup>.  
PEAK READING = 14.1 mag/arcsec<sup>2</sup>.



BEAM SIZE.

SCALE : 0.21 ARCSECONDS PER MILLIMETRE

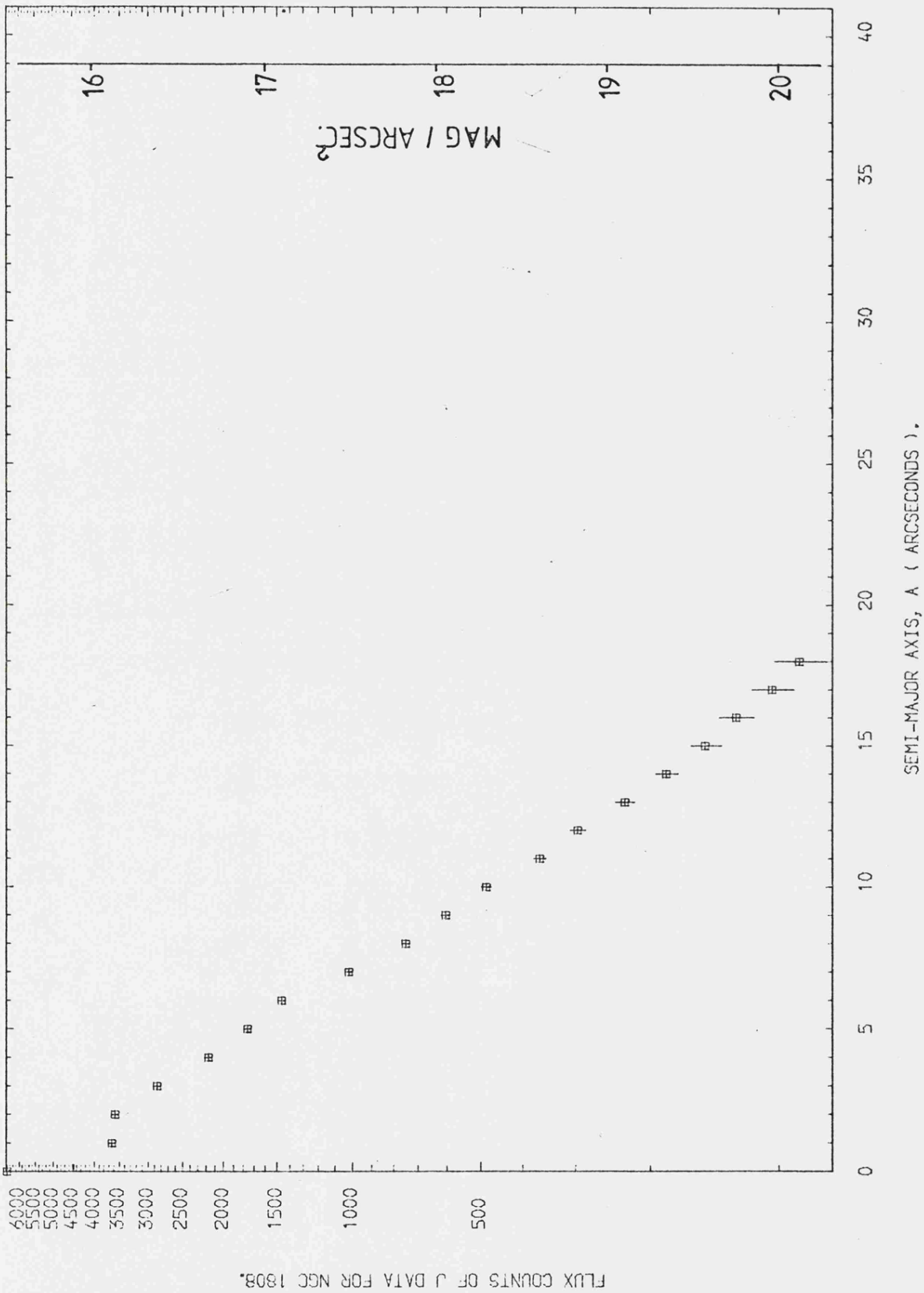
K CONTOUR PLOT OF NGC 1808.

Figure 5.31

an 'S' appearance to the nucleus, and no bar is evident like the previous galaxies. This may be due to its large inclination to the line of sight. The colours obtained from the maps, Table 5.4, are close to the 5 arcsecond spot photometry colour. The colours, shown in Table 5.4, remain constant except for the smallest beam. It, therefore, appears that this galaxy has a compact active nucleus. Frogel et al (1982) suggested, from their 8 to 13 $\mu$ m spectra of the nucleus, that the excess counts seen at these wavelengths were due to hot dust. This observation agrees with our spot photometry and map colours.

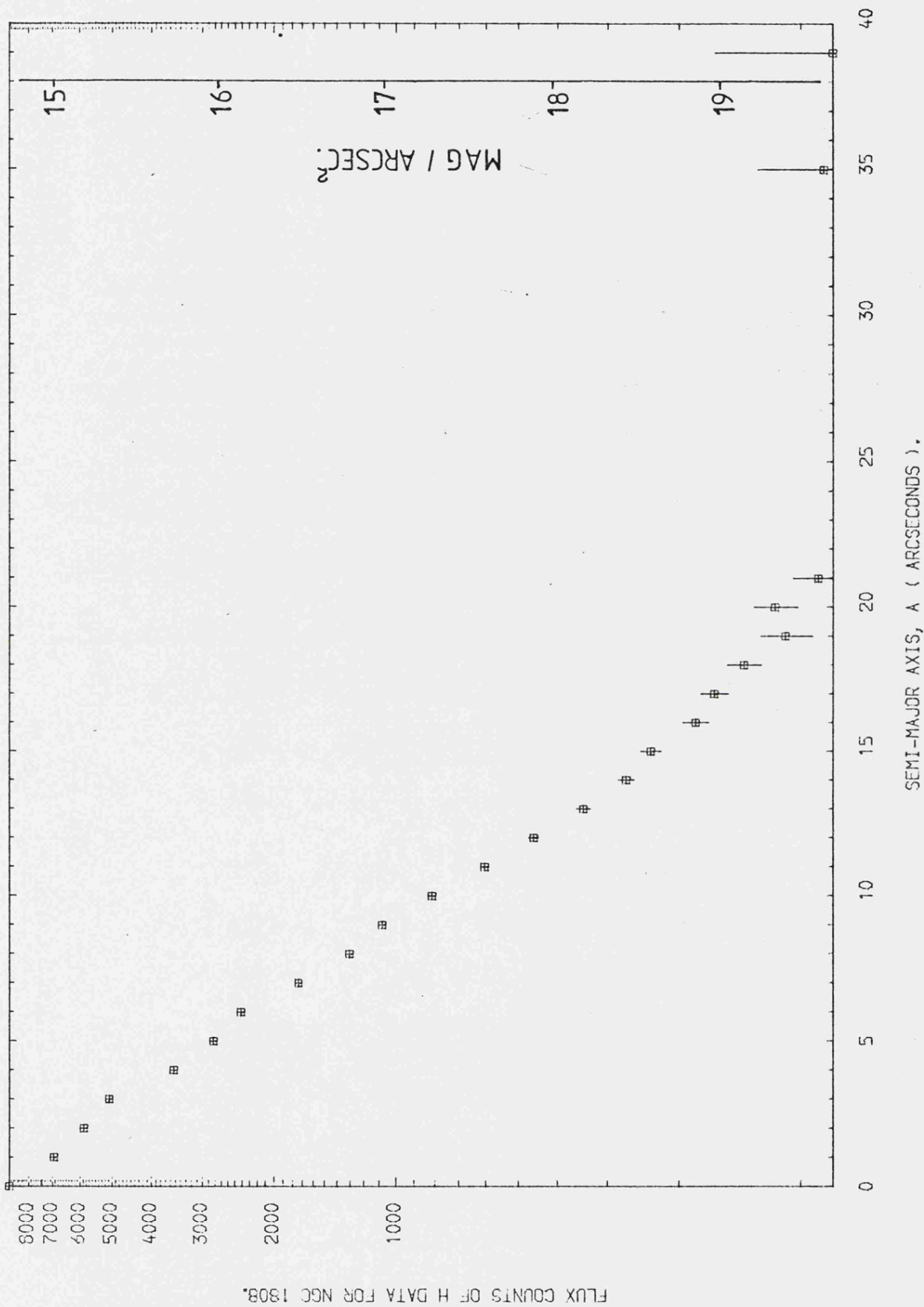
The inclination and PA, in Table 5.2, are noticeably different from the estimates of other people, although this would also be true for NGC 1365 if the values of Wright (1968) and Blackman (1981) were not available. However, if the estimates of de Vaucouleurs and Burbidge are assumed to be correct for NGC 1808, then either the nucleus is elliptical ( or irregular ), if viewed at an inclination of 0°, and/or the isophotes have become distorted due to the bulge eclipsing effect discussed in Appendix D. Therefore, the averages of the values obtained by de Vaucouleurs and Burbidge were used in the annular radial summation routine instead of our estimates.

Figures 5.32, 5.33 and 5.34 are the radial summation profiles for this galaxy. The first point to notice is that no beam effect is evident for the nuclear count and, in fact, the counts go well above a reasonable extrapolation of the curve. A simple explanation for this is that NGC 1808 is a Seyfert 2 galaxy with a nuclear continuum steepening towards longer wavelengths. No other unusual



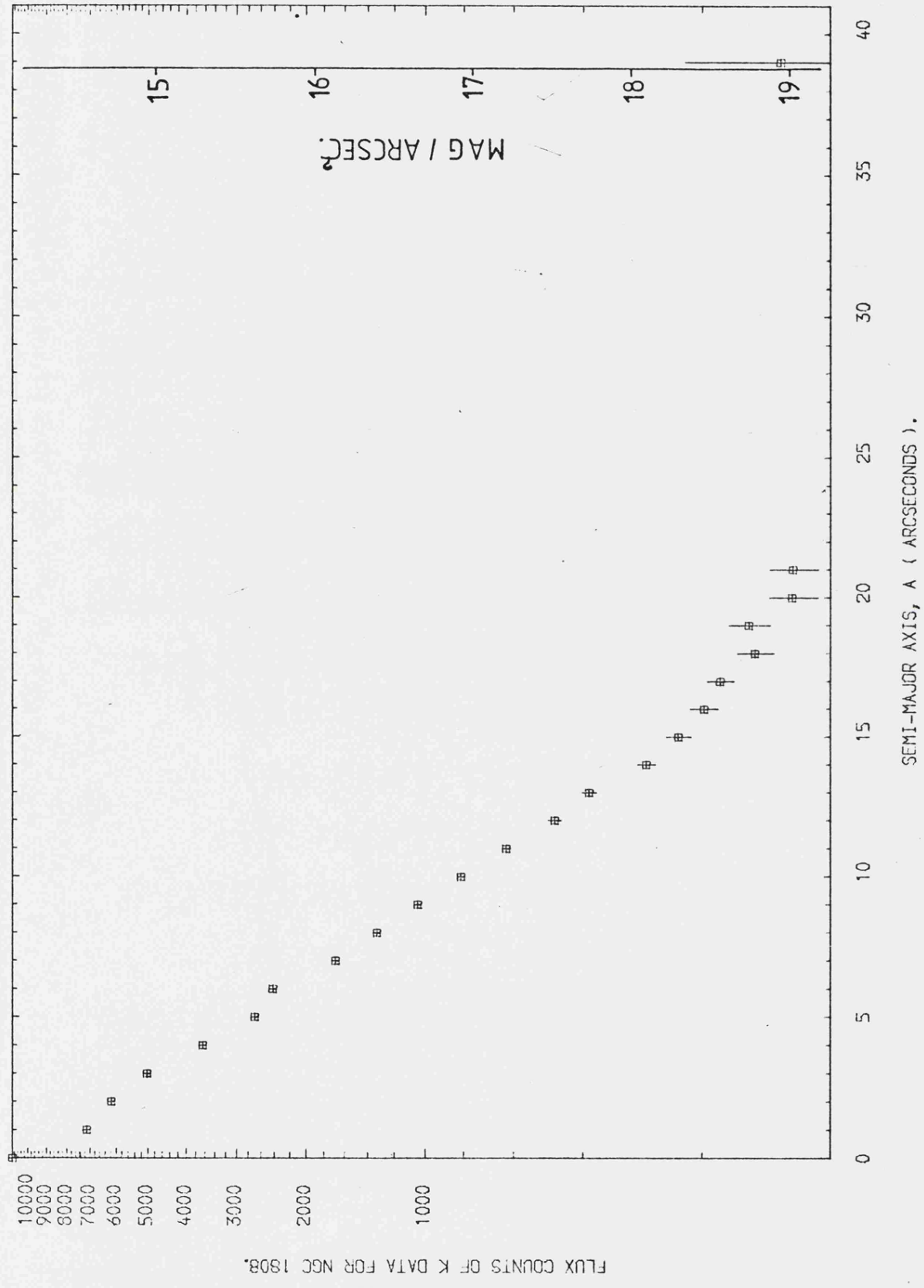
ANNULAR RADIAL SUMMATION PLOTS FOR THE J DATA.

Figure 5.32



ANNULAR RADIAL SUMMATION PLOTS FOR THE H DATA.

Figure 5.33



ANNULAR RADIAL SUMMATION PLOTS FOR THE K DATA.

Figure 5.34

features are observed and the strong feature, which is so apparent on the profile obtained by Prabhu (1980), is not evident on any of our radial profiles. This feature is probably due to a small population of young blue stars which contribute very little to the infrared but, in the optical, contribute a considerable fraction of the total light.

A region 6 arcseconds to the south-east of the nucleus, which on Plate 5.4 is a faint hot-spot, was analysed by doing a cut through this region plus the nucleus and then extrapolating the expected galaxy profile. The resulting colours are shown in Table 5.3. The vector joining the two tends to indicate that this is a HII region with hot dust.

## 5.5 DISCUSSION AND CONCLUSIONS

In an effort to arrive at the possible sources of the excess emission, seen in all the galaxies, extrapolations of the galaxies underlying profiles were fitted by eye. This was the major contributor of the errors on the extrapolated colours in Table 5.3. These errors would have been substantially reduced if the exponential disc component could have been evaluated. De Vaucouleurs law could then have been fitted to the remaining points with the resulting excess counts being attributable to some additional process ( eg HII regions ). However, the exponential disc law could not be estimated since most of the annular radial summation profiles did not extend far enough from the nucleus for the exponential disc component to become the major contributor of the light.

The misalignment of the images meant that a direct comparison of the pictures could not be made and it also proved to be very awkward for the images to be compared when shifting one or both the images. A dual scanning system, available on the AAT now, will do K and J or H scans simultaneously and would have been of great advantage. The K scans, which would be the common wavelength to all the scans, could be used to line the J and H data up and then one would know that the results were true. Also, the AAT's new system has no problems from sky drifts because of its fast scanning mode.

The method employed to remove the drifts from the data in this thesis were not completely successful since the streaky features in the contour plot of NGC 1365 are probably due to some residual sky drifts. However, the method was more successful than simply using a linear fit for the background.

With the exception of NGC 1808 all these galaxies seem to have bars within approximately 1kpc of the nucleus. Except for the nucleus (ie the largest infrared signal) the hot-spots, seen on the optical plates, were shown to be HII regions with hot dust.

One could speculate that the annular radial profiles do conform to the expected profile of a "normal" galaxy with perturbations from unusual amounts of HII regions, hot dust, reddening or young blue stars. However, because the exponential disc law could not be determined with any amount of certainty this could not be confirmed.

There seems to be strong evidence, from the colours, that the nuclei of NGC 1365, 1097, and 1808 are active nuclei

( in descending order of activity ). However, NGC 613's nuclear colours can be explained by reddening or it could be a marginally active nucleus.

## REFERENCES

AARONSON, M., Ph.D. thesis, Harvard University, 1977.

ADAMSON, A., Ph.D. thesis, Leicester University, 1983.

BLACKMAN, C.P., Mon. Not. R. astr. Soc., Vol. 195,  
pp 451-466, 1981.

BURBIDGE, E.M., and BURBIDGE, G.R., Ap. J., Vol. 132,  
pp 30-36, 1960.

BURBIDGE, E.M., and BURBIDGE, G.R., Ap. J., Vol. 151,  
pp 99-103, 1968.

DE VAUCOULEURS, G., DE VAUCOULEURS, A., and CORWIN, H.C.,  
"SECOND REFERENCE CATALOGUE OF BRIGHT GALAXIES", University  
of Texas Press, 1976.

EDMUNDS, M.G., and PAGEL, B.E.J., Mon. Not. R. astr. Soc.,  
Vol. 198, pp 1089-1108, 1982.

FROGEL, J.F., ELIAS, J.H., and PHILLIPS, M.M., Ap. J.,  
Vol. 260, pp 70-74, 1982.

GLASS, I.S., Mon. Not. R. astr. Soc., Vol. 164, pp 155-168,  
1973.

MORGAN, W.W., Pub. A.S.P., Vol. 70, p364, 1958.

OSMER, P.S., SMITH, M.G., and WEEDMAN, D.W., Vol. 192,  
pp 279-291, 1974.

PHILLIPS, M.M., PAGEL, B.E.J., EDMUNDS, M.G., and DIAZ, A., in  
press, 1984.

PRABHU, T.P., J. Astrophys. Astr., Vol. 1, pp 129-154, 1980.

ROCHE, P.F., AITKEN, D.K., PHILLIPS, M.M., and WHITMORE, B.,  
Mon. Not. R. astr. Soc., Vol. 207, pp 35-46, 1984.

SEVIC, J.L., and PASTORIZA, M.G., Pub. A.S.P., Vol. 77,  
pp 287-289, 1965.

SEVIC, J.L., and PASTORIZA, M.G., Pub. A.S.P., Vol. 79,  
pp 152-155, 1967.

TALENT, D.L., Pub. A.S.P., Vol. 94, pp 36-39, 1982.

TELESCO, C.M., and GATLEY, I., Private Communication, 1984.

TOVMASSIAN, G.M., Atrofizica, Vol. 2, p 317, 1966.

VERON, P., LINDBLAD, P.O., ZUIERWIJK, E.J., VERON, M.P., and  
ADAM, G., Astr. Ap., Vol. 87, p 245, 1980.

WRIGHT, R.R., Pub. A.S.P., Vol. 81, pp 51-59, 1969.

**CONCLUDING REMARKS**

### CONCLUDING REMARKS

The CID was shown to have a low sensitivity (  $10^{\text{th}}$  magnitude for a one standard deviation detection in one second with all the light from a point source focused on one element ). Therefore, our plan to scan the nuclear regions of galaxies was impractical. Consequently, although the image quality could be improved and the outgassing of the oil from the Getter could be eliminated, the sensitivity of the CID could not be improved.

The only interesting results obtained with the system showed that the rings of Saturn were considerably brighter than the main body of the planet and that the poles of Jupiter were as bright as the central region of the planet.

Looking to the future, one must await the advent of more sensitive infrared arrays and possibly the introduction of a two dimensional infrared array which would make the scanning mirror system redundant. Until then, Cincinnatti discrete element arrays combined with a wide throw Cassegrainian chopper would be an improvement.

In chapter 4, the final conclusion was that NGC 2683 exhibited a reddening possibly due to internal absorption

within the spiral arms and a spheroidal component. It was proposed that the side westward of the nucleus was the most distant edge due to the greater reddening from the spheroidal component. Beyond 90 arcseconds from the nucleus the colours become bluer which can be explained by a blue disc extending out to at least 7kpc ( for an inclination of  $0^\circ$  ) from the nucleus. Therefore, the reddening due to a halo will be counter acted by the blue disc if the galaxy, being observed, is not exactly edge on. This would make it awkward to detect the halo.

If the signal to noise could be improved it would be interesting to see how the colours would respond beyond 140 arcseconds from the nucleus. Would the colours begin to be dominated by the halo or would no halo be detected?

Three of the four galaxies in chapter 5, namely NGC 1365, 1097, and 1808, exhibit the colour characteristics of Seyfert nuclei. NGC 613's colours can be explained by reddening or it could be a weak active galaxy.

The hot-spots, other than the nucleus, were shown to be HII regions. This agrees with the results obtained by other people.

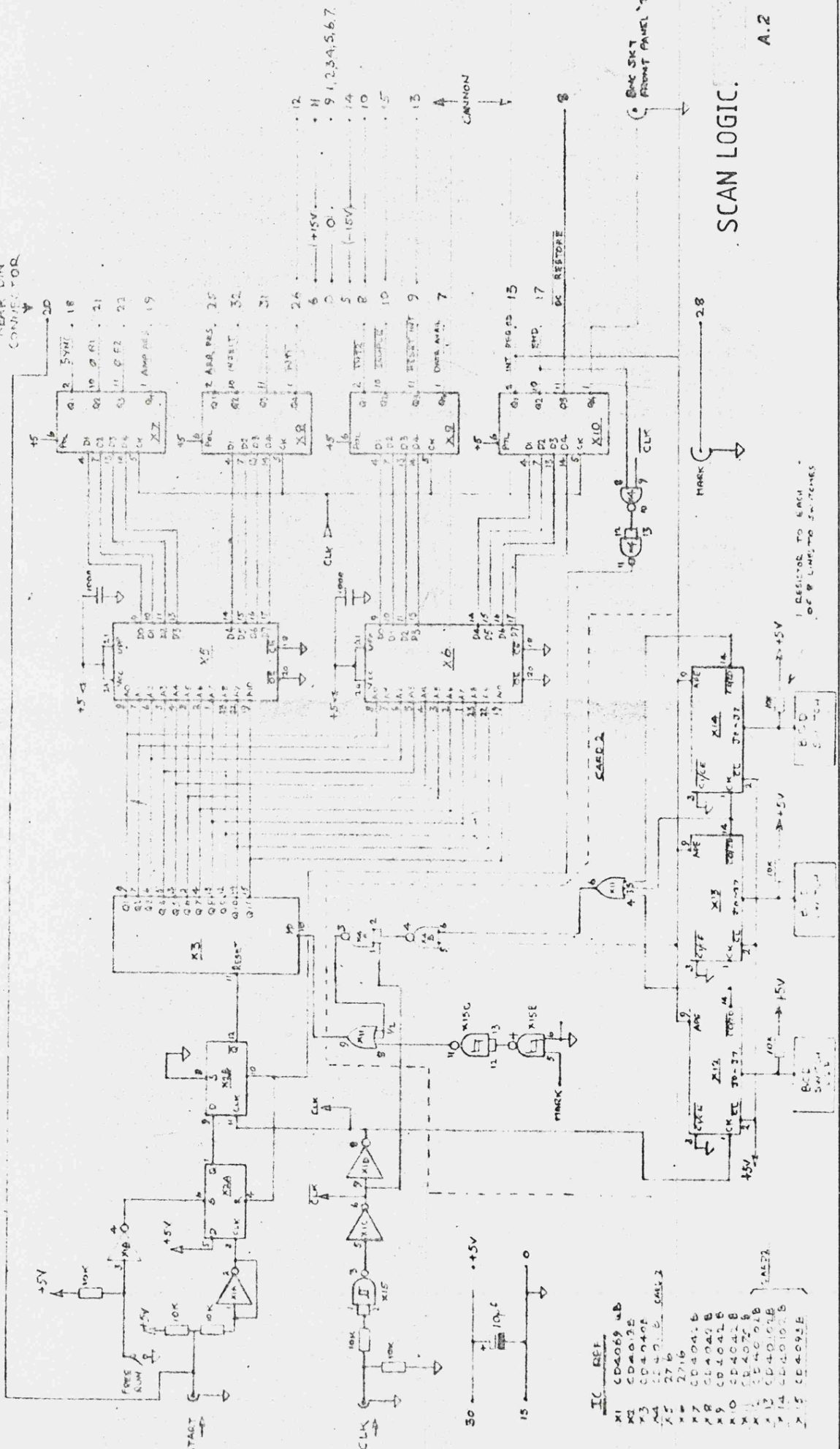
Further observations of these galaxies should be conducted with the new AAT rapid scanning system, thus eliminating the sky drifts. The dual photometer system should also be used so that the colour maps can be obtained more easily and with more certainty.

The mapping area should be enlarged so that the exponential disc and  $R^{1/4}$  laws can be applied to the profiles and a more rigorous analysis of the excess

emission from the hot-spot regions could then be conducted.

*APPENDIX A*

REAR DIN CONNECTOR



SCAN LOGIC.

A.2

IC	REF
X1	CD4069 UB
X2	CD4012
X3	CD4040
X4	CD4013
X5	7416
X6	7416
X7	CD4041 B
X8	CD4041 B
X9	CD4041 B
X10	CD4041 B
X11	CD4041 B
X12	CD4012
X13	CD4012
X14	CD4012
X15	CD4012

RESISTORS TO EACH OF 8 LINES TO 28 PINS





**APPENDIX B**

Listing of the PASCAL programme used in re-formatting the data from the first trip's data files on the CYBER.

```
PROGRAM CONVERT ( INPUT , OUTPUT ) ;
  VAR II , I : INTEGER ;
      CHR : CHAR ;
  BEGIN
    LINELIMIT ( OUTPUT , -1 ) ;
    I := 0 ;
    II := 0 ;
    WHILE NOT EOF ( INPUT ) DO
      BEGIN
        READ ( CHR ) ;
        IF CHR <> ' ' THEN BEGIN
          IF CHR <> '?' THEN BEGIN
            WRITE ( CHR ) ;
            I := I + 1 ;
            II := 0 ;
          END ;
          IF CHR = '?' THEN BEGIN
            I := 0 ;
            IF II = 0 THEN BEGIN
              II := 1 ;
              WRITELN ;
            END ;
          END ;
        END ;
      END ;
    IF NOT EOLN ( INPUT ) THEN BEGIN
      IF I = 80 THEN BEGIN
```

```
I := 0 ;  
WRITELN ;  
END ;  
END ;  
END ;  
END ;  
END.
```

*APPENDIX C*

This appendix gives the derivation of an expression for the semi-major axis given the eccentricity and inclination, with respect to the x-axis measured anti-clockwise from the origin, of an ellipse to which a point, in cartesian coordinates, is associated.

Figure C.1 shows a point [ x,y ] on an ellipse where :-  
 x,y = cartesian coordinates of the point considered,

D = distance of the point from the origin,

$\alpha$  = inclination of the ellipse to the x-axis,

e = eccentricity of the ellipse,

a = semi-major axis of the ellipse,

$R_1$  = distance of the point from focus F1

and

$R_2$  = distance of the point from focus F2.

An ellipse is defined such that :-

$$R_1 + R_2 = 2a \quad \dots[C.1]$$

where, from Figure C.1,  $R_1$  and  $R_2$  are given by :-

$$R_1 = \sqrt{ (x+ae\cos\alpha)^2 + (y-ae\sin\alpha)^2 }$$

and

$$R_2 = \sqrt{ (x+ae\cos\alpha)^2 + (y+ae\sin\alpha)^2 }.$$

Squaring both sides of equation [C.1] one obtains :-

$$R_1^2 + 2R_1R_2 + R_2^2 = 4a^2 \quad \dots[C.2.]$$

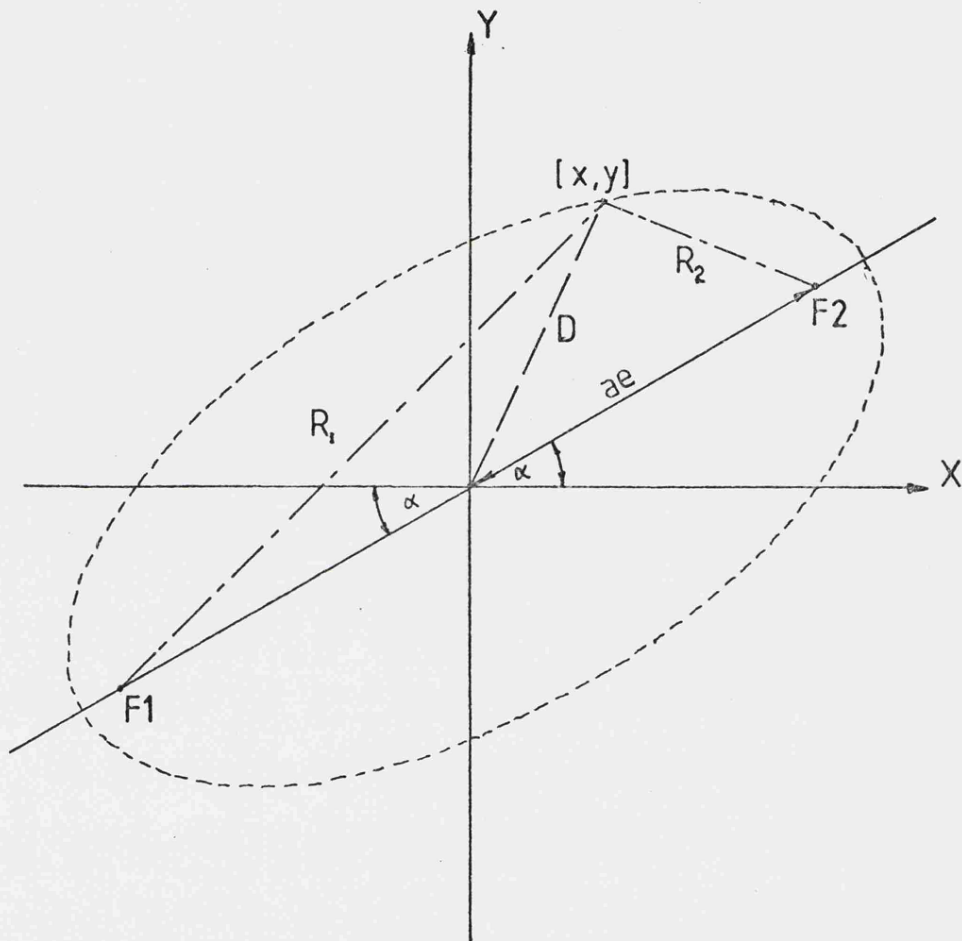


Figure C.1

However, squaring and expanding the two expressions for  $R_1$  and  $R_2$  one arrives at the following :-

$$R_1^2 = D^2 - 2ae( x\cos\alpha + y\sin\alpha ) + a^2e^2 \quad \dots[C.3]$$

and :-

$$R_2^2 = D^2 + 2ae( x\cos\alpha + y\sin\alpha ) + a^2e^2, \quad \dots[C.4]$$

where :-

$$D = \sqrt{ ( x^2 + y^2 ) }.$$

Therefore, from adding the two above expressions together, one gets :-

$$R_1^2 + R_2^2 = 2D^2 + 2(ae)^2 \quad \dots[C.5].$$

Combining equation [C.2 and [C.5 and squaring both sides :-

$$(R_1R_2)^2 = ( 2a^2 - D^2 - (ae)^2 )^2 \quad \dots[C.6]$$

but, multiplying equations [C.3 and [C.4 together, one gets :-

$$(R_1R_2)^2 = D^4 - [2ae( x\cos\alpha + y\sin\alpha )]^2 + 2(aeD)^2 + (ae)^4.$$

Then, combining this with equation [C.6 and re-arranging, an expression for the semi-major axis of the ellipse, on which a point [ x,y ] lies, is obtained :-

$$a = \sqrt{ \left( D^2 - e^2 ( x \cos \alpha + y \sin \alpha )^2 \right) / \left( 1 - e^2 \right) }$$

---

**APPENDIX D**

The bulge of a galaxy shall be assumed to be made up of two solid segments of a sphere, of radius R, such that the plane of the chords are in the plane of the galaxy. As the bulge is inclined to a distant observer, the maximum inclination,  $i_{max}$ , is when the most distant edge disappears behind that part of the bulge vertically ( ie perpendicular to the line of sight of the distant observer ) above the nucleus.

One must define, therefore, the maximum inclination in terms of the two axes of the bulge ( ie the scale height, b, and the intercept of the bulge with the galaxy's plane, a ).

Figure D.1 shows a schematic cross-sectional view of the bulge.

At the point where the edge of the bulge becomes obscured, the distance c is given by :-

$$c = a \cos[i_{max}] \quad \dots[D.1]$$

where  $i_{max}$  = the maximum inclination of the galaxy. However, c is also obtained from :-

$$c = f - e \quad \dots[D.2]$$

where :-

$$f = \sqrt{ ( R^2 - (d \cos[i_{max}])^2 ) },$$

$$e = d \sin[i_{max}]$$

and

$$d = \sqrt{ ( R^2 - a^2 ) }.$$

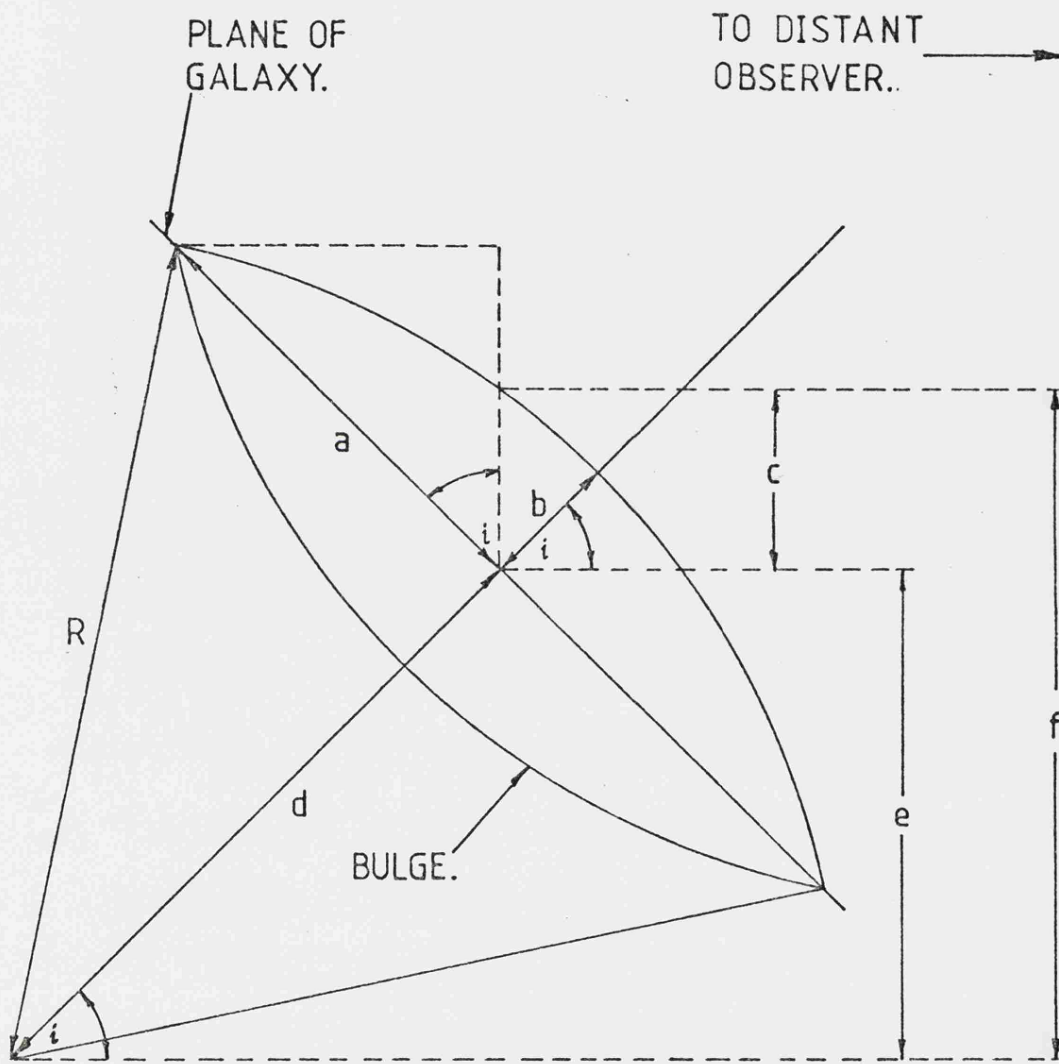


Figure D.1

Equating [D.1 to [D.2 and using the expression for f, e and d one obtains :-

$$a \cos[i_{\max}] = \sqrt{ ( R^2 \sin^2[i_{\max}] + a^2 \cos^2[i_{\max}] ) - \sin[i_{\max}] \cdot \sqrt{ ( R^2 - a^2 ) } .}$$

Dividing through by  $\cos[i_{\max}]$  :-

$$a = \sqrt{ ( R^2 \tan^2[i_{\max}] + a^2 ) } - \tan[i_{\max}] \cdot \sqrt{ ( R^2 - a^2 ) } .$$

Taking the negative expression on the right to the left hand side and squaring one obtains :-

$$a^2 + 2a \tan[i_{\max}] \cdot \sqrt{ ( R^2 - a^2 ) } + ( R^2 - a^2 ) \cdot \tan^2[i_{\max}] = R^2 \tan^2[i_{\max}] + a^2 .$$

Cancelling identical terms in the above gives an expression for  $i_{\max}$  in terms of R and a :-

$$i_{\max} = \tan^{-1} [ 2 \sqrt{ ( -1 + ( R/a )^2 ) } ] \quad \dots [D.3]$$

However, an expression in terms of b rather than R is desirable. Therefore, using the equation for b :-

$$b = R - d = R - \sqrt{ ( R^2 - a^2 ) } ,$$

one can obtain an expression for R in terms of a and b :-

$$R = ( b^2 + a^2 ) / 2b .$$

Substituting this into equation [D.3, the final expression

for  $i_{\max}$  is arrived at in terms of the scale height and width of the bulge :-

$$i_{\max} = \text{Tan}^{-1} [ a/b - b/a ].$$

---

## ACKNOWLEDGEMENTS

I would like to thank all those people who have assisted me for the past three ( and a half! ) years.

Firstly, Richard, my supervisor, for being a source of ideas and for the enormous amount of tolerance he has displayed over the last few years, which was above and beyond the call of duty.

Dave, for his helpful suggestions when I was attempting to understand microprocessors.

Martin Ward, for his help in chapter 5 and for providing the greyscale plots of NGC 1097 and 1365.

Vince and Chas, for their help with the equipment and awful jokes.

Al and Bob, for their work on the array.

Norma, who bought the coffee that kept me on edge.

Nick and Robert, for their inspiring performances on the BBC micro.

Simon and John M., for their discouraging performances on the BBC micro.

Andy, for being the source and the recipient of many a practical joke on the Cyber.

John F., for being the brunt of many a sarcastic comment, although the traffic has not been all one way. However, because I was very close to the finishing date, I think the free meal should be a quick takeaway.

Sifu Derek Frearson for his enjoyable Kung Fu and Tai Chi Chuan classes, without which there would have been a

significant reduction in the number of bruises, but with which I would have gone MAD!

Finally, but definitely not the smallest, Anne, who has persevered with my company from when I was a little first year to the present day and who has slogged her way through my thesis ( yawn! ) checking the grammar and spelling.

## ASTRONOMICAL INFRARED IMAGING

- by C.HOLLAND

( Ph.D. 1984, LEICESTER UNIVERSITY )

### ABSTRACT

The object of this thesis was to develop an imaging system using a CID Indium Antimonide ( InSb ) 33 element detector. Some interesting results were obtained on the rings of Saturn and the poles of Jupiter and the detector would have been used to scan the nuclear regions of galaxies. However, the array had a low sensitivity and a slow response which made it impractical to carry out any observations of galactic nuclei.

Data, from single detector scans of NGC 2683, were provided by Dr.A.Adamson and Dr.D.J.Adams. These scans were performed to see if a halo exists around this galaxy. Two methods were used. The first was a deconvolution method which is shown to have a fault when deconvolving diffuse objects. The second method was to analyse the colour indices. This method indicated that there could be a spheroidal component causing the V-J colour to become redder out to approximately 90 arcseconds from the nucleus. Beyond 90 arcseconds, the colour becomes bluer possibly because the galaxy is not quite edge on and the blue disc begins to dominate the colour.

The last chapter deals with the morphologically peculiar galaxies NGC 613, 1097, 1365 and 1808. The data on these galaxies were obtained on the AAT using a single detector which was scanned across the objects in a DC mapping mode. Maps were constructed, on a CYBER 73 at Leicester, from the J, H and K data. The data were then examined to see if these galaxies conform to the usual exponential disc and  $R^{1/4}$  laws.

The three latter galaxies seem to exhibit nuclear colours similar to Seyfert's and NGC 613 may be either a weak active galaxy, or could just simply suffer from reddening.